Amyloids in the Spotlight: Investigating Disease-Associated Peptides, and the Quest for Effective Treatments

Inaugural-Dissertation

zur Erlangung des Doktorgrades
der Mathematisch-Naturwissenschaftlichen Fakultät der
Heinrich-Heine-Universität Düsseldorf

vorgelegt von

Anne Pfitzer-Bilsing

aus Moers

Düsseldorf, Oktober 2023

aus dem Institut für Physikalische Biologie
der Heinrich-Heine-Universität Düsseldorf

Gedruckt mit der Genehmigung der
Mathematisch-Naturwissenschaftlichen Fakultät der
Heinrich-Heine-Universität Düsseldorf

Berichterstatter:

1. Jun.-Prof. Dr. Wolfgang Hoyer
2. Prof. Dr. Dieter Willbold

Tag der mündlichen Prüfung: 19.12.2023

„Don’t dream it. Be it.”
Frank-N-Furter
Tim Curry

Contents

Erklärung

Ich versichere an Eides Statt, dass die Dissertation von mir selbständig und ohne unzulässige fremde Hilfe unter Beachtung der „Grundsätze zur Sicherung guter wissenschaftlicher Praxis an der Heinrich-Heine-Universität Düsseldorf“ erstellt worden ist. Die Dissertation wurde in der vorgelegten oder in ähnlicher Form noch bei keiner anderen Institution eingereicht. Ich habe bisher keine erfolglosen Promotionsversuche unternommen.

Düsseldorf, 12.10.2023 Anne Pfitzer-Bilsing

Acknowledgements

Ich möchte mich bei den Menschen bedanken, die mich in den letzten Jahren unterstützt haben.

Dabei möchte ich Jun.-Prof. Dr. Wolfgang Hoyer als Erstes danken. Danke, dass ich meine Arbeit in Deiner Arbeitsgruppe anfertigen durfte und Du mir die Freiheit eingeräumt hast, ein eigenes Thema zu bearbeiten. Danke auch dafür, dass Du es mir ermöglicht hast, an weiteren spannenden Themen zu arbeiten und ich von Deinem riesigen Wissensreichtum profitieren durfte. Deine offene und durchweg positive Art schätze ich besonders. Danke, dass Du mich immer unterstützt hast.

Ebenfalls möchte ich mich bei Prof. Dr. Dieter Willbold bedanken. Danke, dass Du die Aufgabe des Mentors und Korreferenten übernommen hast, die sehr diversen Projekte im Institut durchweg unterstützt und immer mit einem offenen Ohr und einem guten Rat zur Seite stehst.

Ein sehr großer Dank gilt der Jürgen-Manchot-Stiftung, ohne die ich nicht so frei meine Doktorarbeit hätte gestalten können. Vielen Dank für die finanzielle Unterstützung und das entgegengebrachte Vertrauen.

Weiterhin möchte ich mich bei meinem Hauptprojektpartner Filip Hasecke bedanken. Danke, dass Du Dir ein so innovatives Projekt überlegt hast, um die Therapie amyloider Erkrankungen zu revolutionieren. Leider mussten wir nach Jahren feststellen, dass wir uns in einer wissenschaftlichen Sackgasse befinden und uns eingestehen, dass die Idee der Nutzung von Antikörpern mit proteolytischen Eigenschaften aktuell nicht zielführend ist. Was bleibt, ist die Etablierung einer großartigen Methode, auf die wir stolz sein können. Danke, dass Du mich in das Projekt geholt hast.

Außerdem möchte ich mich herzlich bei Prof. Dr. Charlotte Esser und Dr. Nadine Teichweyde für die Bereitstellung und Bedienung ihres Durchflusszytometers bedanken! Ein weiterer Dank gilt Dennis Hasenklever, der sich um die Instandhaltung der neu angelegten FACS-Facility kümmert und immer ansprechbar ist. Ein weiterer Dank gilt Prof. Dr. Vlada Urlacher für die großzügige Bereitstellung ihres qPCR-Geräts. Ein weiterer Dank gilt an dieser Stelle Sebastian Hölzel und Fabian Schmitz für den kurzen Draht bei der Terminabsprache.

Ein weiteres Dankeschön gilt Celina Schulz, mit der ich in zwei Projekten zusammenarbeiten durfte. Danke für die großartige Zusammenarbeit! Ich habe es sehr genossen, mit Dir in die α-Synuclein-Welt einzutauchen und auch die „einzig wahre Methode“ unserer Gruppe, ThT-Assays, kennenzulernen. Auch hat es mir große Freude bereitet, mit Dir im dimIAPP-Projekt zusammen zu arbeiten. Deine Zielstrebigkeit, Dein Engagement und Dein Humor sind Eigenschaften, die uns in den Projekten vorangebracht haben. Danke auch für die konstruktiven Korrekturen zu dieser Arbeit. Ich freue mich auf den nächsten Aperol und das nächste gute Gespräch mit Dir und bedanke mich für Deine Freundschaft!

Auch möchte ich mich bei Melissa Jansing, meiner Büronachbarin bedanken. Danke für die guten und vor allem tiefen Gespräche, Krisensitzungen und herzhaften Lacher im Büro. Danke für Deine Loyalität, Deine Empathie, Dein Verständnis, Deine Feinfühligkeit und Deine Ehrlichkeit. Danke auch für Deine konstruktiven Korrekturen zu dieser Arbeit. Du weißt, dass Du nicht nur eine Kollegin, sondern eine wundervolle Freundin für mich bist und ich bin froh, Dich in meinem Leben zu haben und immer auf Dich zählen zu können.
Danke auch an Marie Schützmann. Danke für Deine Ehrlichkeit, Offenheit und Deinen Witz. Danke für die Unterstützung, Ratschläge und Diskussionen.
Ein großer Dank gilt außerdem Robin Backer. Danke für Deine aufopferungsvolle Arbeit und den Humor, den Du nie verlierst. Du bist ein toller BTA und ein toller Mensch. Lass Dir Deine positive Art nie nehmen.
Ich bin ebenfalls dankbar für die Menschen, mit denen ich über die Jahre das Büro teilen durfte: Danke an Dr. Marcel Schmidt geb. Falke, Melissa Jansing, Filip Hasecke, Dr. Alexandra Dybala geb. Ziemski, Marie Schützmann, Fernanda Salome Peralta Reyes, Robin Backer, Justin Böcker und Ci Chu für lustige Momente, die ich nie vergessen werde und die jedes noch so frustrierende Ergebnis in den Hintergrund rücken lassen. Auch den bürointernen Dackelclub möchte ich nicht missen.
Danke an Melissa Jansing, Bianca-Georgiana Axinte und Katharina Vormann für schöne und lustige Abende. Ich danke auch allen anderen, die die IPB Nights Out unvergesslich gemacht haben!
Ein weiterer besonderer Dank gilt meiner ersten Studentin Stefanie Williams geb. Neufeld. Du hast sowohl in Deinem Forschungspraktikum als auch in Deiner Bachelorarbeit großartige Arbeit geleistet und Filips und mein Projekt vorangetrieben. Ich bin sehr dankbar, mit einer so wissbegierigen, motivierten und talentierten Person zusammengearbeitet zu haben.
Ich bedanke mich weiter bei allen weiteren Studierenden, die ich während meiner Zeit als Doktorandin betreuen und begleiten durfte: ein besonderer Dank gilt an dieser Stelle Kim Joleene Kunk und Martin Froning genannt Havixbeck.
Außerdem möchte ich mich bei allen aktuellen und ehemaligen Mitgliedern der AG Hoyer, auch Wolf-Gang genannt, für inspirierende Group Meetings und schöne Gruppenaktivitäten bedanken. Danke an Dr. Christine Röder, die ich als Mitglied der AG kennenlernen durfte und auf die ich seitdem zählen kann.
Ich möchte mich bei allen Mitgliedern des Instituts fürs Physikalische Biologie bedanken. Ich schätze besonders die Arbeitsatmosphäre im Institut, den freundlichen Umgang untereinander und die hohe Hilfsbereitschaft unter den Kollegen.
Danke auch an HeRa für das Reisekostenstipendium für die jährliche Versammlung der Protein Society in San Francisco in Kalifornien, an der ich mit Celina Schultz und Marie

Schützmann teilnehmen durfte. Auch bei allen Mitarbeitern von iGrad möchte ich mich für die tolle Auswahl weiterbildender Kurse bedanken!
Außerdem möchte ich mich auch bei der Gesellschaft für Biochemie und Molekularbiologie e.V. bedanken, die mich seit meinem Studium begleitet. Die ehrenamtlichen Tätigkeiten in der Gesellschaft haben mir immer Freude bereitet und waren ein guter Ausgleich.
Ein großer Dank gilt auch den Freunden, die ich während meines Studiums kennenlernen durfte. Ich bedanke mich herzlich bei Leonie Windeln, die mich nun seit 10 Jahren durch Dick und Dünn begleitet und ein Fels in der Brandung für mich ist. Danke für Deine Freundschaft! Together we are strong. Außerdem bedanke ich mich bei Nora Bitzenhofer, Dr. Lea Sundermeyer, Daria Lehrmann, Dr. Alexander Fejzagic, Manuel Anlauf, Vivian Willers, Niklas Peters und Maurice Tust für unzählige unvergessliche Erlebnisse in den letzten 10 Jahren.
Ein weiterer Dank gilt meiner besten Freundin seit Kindertagen Kim Wälbers. Danke, dass Du immer bedingungslos für mich da bist, mir immer zuhörst und mir immer mit Rat und Tat zur Seite stehst.
Bei meinen anderen Freunden möchte ich mich auch bedanken für all die Unterstützung, die Ihr mir entgegenbringt.
Meine Eltern Elke und Andreas Pfitzer und mein Bruder Kai Pfitzer verdienen natürlich auch einen großen Dank. Danke Mama und Papa, dass Ihr mich immer unterstützt und immer für mich da seid. Kai, auch Dir danke ich für ein offenes Ohr und Deine Unterstützung. Ich bedanke mich auch beim Rest der Familie. Ich bin froh, euch zu haben.
Zu guter Letzt möchte ich mich bei meinem Ehemann Florestan Bilsing bedanken. Ich bedanke mich bei Dir nicht nur für die konstruktiven Kommentare zu dieser Arbeit, sondern einfach für alles. Danke, dass Du immer alles auffängst, mich immer unterstützt, mir den Rücken freihältst und einfach danke dafür, dass Du mich so liebst, wie ich bin.

Figures

Tables

Abbreviations

$(G_4S)_4$	Glycine serine linker
°C	Degree Celsius
µl	microlitres
µM	Micromolar
5-FAM	5-carboxyfluorescein
aa	Amino acid
AC mode	Intermittent contact mode
AChEIs	Acetylcholinesterase inhibitors
Actb	Beta-actin
AD	Alzheimer's disease
AFM	Atomic Force Microscopy
AMP	Adenosine monophosphate
AMPK	Adenosine monophosphate activated protein-kinase
ApoE4	Apolipoprotein E4
APP	Amyloid precursor protein
Atf	Activating transcription factor
ATP	Adenosine triphosphate
Aβ	Amyloid β
$Aβ_{40}$	Amyloid β residue 1-40
$Aβ_{42}$	Amyloid β residue 1-42
BBB	Blood-brain-barrier
BMI	Body mass index
Cat	Catalase
CCD	Charge-coupled device
cDNA	Complementary desoxyribonucleic acid
CDR-SB	Clinical Dementia Rating sum of boxes score
Chop	CCAAT-enhancer-binding protein homologous protein
Cy5	Cyanine 5
DA	Dopamine
DAPI	4',6-diamidino-2-phenylindole
DBS	Deep-brain-stimulation
DimAβ	Dimeric Amyloid β
dimIAPP	Dimeric modified IAPP (C2S, C7S)
dimIAPP-O	Oligomers of dimeric modified IAPP (C2S, C7S)
DMSO	Dimethyl sulfoxide

DNA	Desoxyribonucleic acid
dNTPs	Nucleoside triphosphates
DTT	Dithiothreitol
E. coli	Escherichia Coli
ECGC	Epigallocatechin gallate
EDTA	Ethylenediaminetetraacetic acid
emPCR	Emulsion Polymerase Chain Reaction
ER	Endoplasmic reticulum
et al.	Et alia
FACS	Fluorescence-activated cell sorting
FDA	Food & Drug Administration
For	Forward
fwd	Forward
G3BP	Ras-GTPase-activating protein binding proteins
GABA	γ-aminobutyric acid
Gapdh	Glyceraldehyde-3-phosphate dehydrogenase
GdmCl	Guanidium hydrochloride
GLP1	Glucagon-like peptide 1
GLUT	Glucose transporter
h	Hour
H_2O	Water
H_2O_2	Hydrogen peroxide
HCl	Hydrogen chloride
HF	High fidelity
HFIP	1,1,1,3,3,3-hexfluoro-2-propanol
HIV	Human Immunodeficiency Virus
HP	Hairpin
HPLC	High performance liquid chromatography
IAPP	Islet amyloid polypeptide
IDP	Intrinsically disordered protein
Ig	Immunoglobulin
IMAC	Immobilized metal affinity chromatography
IRE	Inositol-requiring protein 1
IVC	In vitro compartment
IVTT	In vitro transcription and translation
kg	Kilogram
l	Liter

LDL	Low density lipoprotein
LibIgV$_2$	Library antibody derivatives with two chains
LibNano	Nanobody library
LLPS	Liquid-liquid phase separation
LPS	Lipopolysaccharide
m	Meter
M	Molar
MAO-B	Monoamine oxidase-B
MES	2-(N-Morpholino)ethansulfonic acid
min	Minute
ml	Millilitres
mm	Millimetre
mM	Millimolar
MOPS	3-(N-Morpholino)propansulfonsäure
MQ	Milli-Q
mRNA	Messenger ribonucleic acid
MWCO	Molecular weight cut-off
NAC	Non-amyloid β component
NaCl	Sodium chloride
NaN_3	Sodium azide
NaOH	Sodium hydroxide
NaPi	Sodium phosphate buffer
NDMA	N-methyl-D-aspartate
nm	Nanometre
OD	Optical density
PACMAN	Proteolytic Antigen Cleavage Mediated AmplificatioN
PAGE	Polyacrylamide gel electrophoresis
PBMC	Peripheral mononuclear cells
PBS	Phosphate-buffered saline
PCR	Polymerase Chain Reaction
PD	Parkinson’s disease
PERK	Pancreatic eukaryotic translation initiation factor 2α kinase
pg	Picogram
pIgV	Plasmid for variable immunoglobulin derivatives
PMSF	Phenylmethylsulfonyl fluoride
qPCR	Quantitative polymerase chain reaction
RBS	Ribosome binding site

rev	Reverse
RNA	Ribonucleic acid
ROS	Reactive oxygen species
RP	Reversed-phase
rpm	Rounds per minute
s	Second
scFv	Single-chain variable fragment
SDS	Sodium dodecyl sulfate
SEC	Size exclusion chromatography
SI	Supplementary Information
Sod2	Superoxide dismutase 2
T2DM	*Diabetes mellitus* Type 2
TAE	Tris based buffer with acectic acid and ethylenediaminetetraacetic acid
TEV	Tobacco Etch Virus
TFA	Trifluoroacetic acid
TH	Tyrosine hydroxylase
ThT	Thioflavin T
Tris	Tris(hydroxymethyl)aminomethane
UTR	Untranslated region
V	Volt
WT	Wildtype
Xbp	X-box binding protein
α-syn	α-synuclein

amino acid	three letter code	one letter code
alanine	Ala	A
arginine	Arg	R
asparagine	Asn	N
aspartic acid	Asp	D
cysteine	Cys	C
glutamic acid	Glu	E
glutamine	Gln	Q
glycine	Gly	G
histidine	His	H
isoleucine	Ile	I
leucine	Leu	L
lysine	Lys	K
methionine	Met	M
phenylalanine	Met	F
proline	Pro	P
serine	Ser	S
threonine	Thr	T
tryptophan	Trp	W
tyrosine	Tyr	Y
valine	Val	V

abbreviation base	meaning
A	adenine
C	cytosine
G	guanine
T	thymine
W	adenine or thymine
S	cytosine or guanine
R	adenine or guanine
Y	cytosine or thymine
K	guanine or thymine
M	adenine or cytosine
B	cytosine, guanine or thymine
D	adenine, guanine or thymine
H	adenine, cytosine or thymine
V	adenine, cytosine or guanine
N	adenine, cytosine, guanine or thymine

Summary

In this thesis, I present basic research on diseases caused by the amyloid aggregation of certain peptides as well as method development enabling us to find new therapeutic strategies. This is of great interest as none of the amyloid diseases is currently curable. To be able to find effective treatment, the understanding of mechanisms is of great importance. To contribute to this goal, I dealt with two different amyloidogenic peptides, namely α-synuclein and islet amyloid polypeptide. α-Synuclein is associated with the development of multiple diseases of which the most prominent one is Parkinson's disease while islet amyloid polypeptide plays a fatal role in the progression of *Diabetes Mellitus* Type 2.

One aim was to understand the mechanism of the inhibition of α-synuclein fibril elongation induced by a dimeric construct of α-synuclein comprising a hairpin motif in one of the two monomers fused. We subdivided α-synuclein in four defined regions and prepared several truncated versions. We found that a construct comprising only the regions forming the amyloid fibril core is sufficient for inhibition of the elongation process. This indicates that the regions critical for fibril formation can also be crucial for blocking of fibril growth.

Another objective of this thesis was the introduction of a model of islet amyloid polypeptide guaranteeing stable oligomers. This is of interest as islet amyloid polypeptide is highly aggregation prone and it is still not fully understood which species of amyloid aggregates are responsible for the progression of the disease. Our work offers the opportunity to gain more insights.

As conventional strategies have not yet led to disease-modifying therapies, novel treatment approaches are desperately needed. We aimed to no longer utilize conventional antibodies but revolutionize the field by introducing antibodies with proteolytic characteristics. To get access to naturally occurring proteolytic antibodies, we established a method which can be used for the isolation of proteolytic antibody derivatives from human blood donations. The method is feasible and easy to apply which could be proved by a model system. However, the actual motivation for us to establish the method, the isolation and selection of proteolytic antibodies, was not of success. After many detailed experiments, we doubt the existence of proteolytic antibodies possessing sufficient enzymatic activity. However, the invented method is an interesting tool for the selection of proteases.

This thesis gives insights about current questions in the field of amyloids and amyloid diseases.

Zusammenfassung

In dieser Arbeit beschäftige ich mich mit der Grundlagenforschung zu Krankheiten, die durch die Amyloid-Aggregation bestimmter Peptide verursacht werden, sowie mit der Entwicklung von Methoden, um neue therapeutische Strategien zu finden. Beide Felder sind von großem Interesse, da derzeit keine der Amyloid-Krankheiten heilbar ist. Um eine wirksame Behandlung finden zu können, ist das Verständnis der Mechanismen von großer Bedeutung. Um zu diesem Ziel beizutragen, habe ich mich mit zwei verschiedenen amyloiden Peptiden, nämlich α-Synuclein und Amylin, befasst. α-Synuclein wird mit der Entstehung zahlreicher Krankheiten in Verbindung gebracht, von denen die Parkinson-Krankheit die bekannteste ist, während Amylin eine verheerende Rolle bei der Entwicklung von *Diabetes mellitus* Typ 2 spielt.

Unser Ziel war es daher, den Mechanismus der Hemmung der Elongation von α-Synuclein zu verstehen, die durch ein dimeres Konstrukt von α-Synuclein bewirkt werden kann. Das Konstrukt beinhaltet in einem der beiden fusionierten Monomere ein Haarnadelmotiv. Wir haben α-Synuclein in vier definierte Regionen unterteilt und verschiedene verkürzte Versionen hergestellt. Wir fanden heraus, dass nicht das gesamte Konstrukt benötigt wird, sondern nur ein um die Hälfte verkürztes Konstrukt für die Hemmung des Elongationsprozesses ausreichend ist. Besonders interessant war, dass dieses Konstrukt die für die Bildung der Fibrille selbst kritischen Regionen umfasst.

Ein weiteres Ziel dieser Arbeit war die Einführung eines Amylin-Modells, das die Bildung stabiler Oligomere ermöglicht. Dies ist von Interesse, da Amylin stark zur Aggregation neigt und noch nicht vollständig geklärt ist, welche Arten von Amyloid-Aggregaten für das Voranschreiten der Krankheit verantwortlich sind. Unsere Arbeit bietet die Grundlage, die Fragestellung verlässlich zu bearbeiten.

Da die konventionellen Behandlungsstrategien, mit Ausnahme derjenigen, die derzeit in klinischen Studien erprobt werden, bisher nicht erfolgreich sind, werden dringend neue Behandlungsansätze benötigt. Unser Ziel war es, statt herkömmlichen Antikörpern Antikörper mit proteolytischen Eigenschaften in den Fokus zu rücken. Um Zugang zu natürlich vorkommenden proteolytischen Antikörpern zu erhalten, haben wir eine Methode entwickelt, die zur Isolierung proteolytischer Antikörperderivate aus menschlichen Blutspenden verwendet werden kann. Die Methode ist praktikabel und einfach anwendbar, was anhand eines Modellsystems nachgewiesen werden konnte. Die eigentliche Motivation für die Etablierung der Methode, die Isolierung und Selektion von proteolytischen Antikörpern, war nicht erfolgreich. Nach vielen gescheiterten Experimenten zweifeln wir an der Existenz proteolytischer Antikörper. Die von uns entwickelte Methode ist jedoch für die Selektion von Proteasen mit bestimmten Eigenschaften von großem Interesse.

Diese Thesis gibt Einblicke in wichtige Fragen rund um die Themen Amyloide und Amyloid-Krankheiten.

1 General Introduction

1.1 Amyloid

The term „amyloid“ was introduced by Rudolph Virchow in 1854 after his discovery of cerebral corpora amylacea under the microscope. He stained these structures with iodine resulting them to appear pale blue. Subsequent treatment with sulfuric acid changed their colour to violet. From this observation, he concluded these species to consist of cellulose or starch and termed them “amyloid” after the Greek word for starch, *amylon* (1). In 1859, Friedreich and Kekule disproved the assertion that amyloids consist of carbohydrates and interposed amyloids to be proteins (2).

Misfolding processes of proteins can lead to the formation of amyloid structures and development of amyloid diseases. Amyloid fibres display a cross-β fibre diffraction pattern in X-ray first observed in 1968 by Eanes and Glenner (3). Those fibrils consist of β-strands which align perpendicularly to the long axis of the fibril in each protofilament (4). This architecture is termed a cross-β amyloid fold (5). Important features of this cross-β spine were identified from fibrils either isolated from diseased tissues or *in vitro* conversion of proteins and analysed by different methods, such as solid-state nuclear magnetic resonance (NMR) as reviewed by Tycko *et al.* (6), model building by X-ray fibre and powder diffraction (7), site-directed spin labelling (8), cryo-EM (9), scanning mutagenesis (10), and single crystal X-ray diffraction (11). Eisenberg and Jucker (12) summarized from these studies general characteristics for amyloid fibers: (1) the strongest repeating feature is a set of β-sheets parallel to the fibril axis with their extended strands near perpendicular to the axis, (2) the β-sheets can appear parallel or antiparallel and (3) the sheets are in register, meaning the strands align with each other, so identical side chains lie on top of each other along the fibril axis. Protofilaments consist most often of two sheets of the peptide or protein. Within one protofilament of the fibril, the side chains of the two sheets are tightly interdigitated like the teeth of a zipper (12).
While biophysicists’ definition of “amyloid” refers to structural properties, the one by pathologists has been different and refers to extracellularly, unbranched pathological fibres capable to bind Congo red and exhibit green birefringence when viewed between crossed polarizers (12, 13). The Nomenclature Committee of the International Society of Amyloidosis (ISA) has agreed that the term “amyloid fibril” should be used for any cross-β fibril (14), but underlines the importance to the observance of different amyloid fibril classes (15).
For amyloids, the primary sequence does not predict the structure of the fibril. Even under the same growth conditions, different structures are possible (16-18). This finding can be seen as the main difference between amyloid and globular proteins which always fold into the same structure when released from the ribosome (19).

Iadanza *et al.* (5) reviewed in 2018 the mechanism of proteins to assemble into amyloid fibrils (Figure 1.1): native proteins are in a dynamic equilibrium with their less-structured, intermediate, or unfolded states. These states assemble into oligomers which elongate to fibril nuclei. They assemble into amyloid fibrils by recruiting other monomers. There are two main mechanisms which make the fibril grow, either in length at the fibril's ends, namely elongation, or in a branched manner at the fibril's surface, namely secondary nucleation. Besides secondary nucleation, also primary nucleation occurs and describes a rare process in which the aggregation is initiated by the protein itself (20). Fragmentation and depolymerization are two possible mechanisms to dismantle the fibril. When it comes to fragmentation, more fibril ends are generated which allows the genesis of new fibrils by recruiting new aggregation-prone monomers. However, dissolution of the fibril is not favoured (11). By interaction of the fibrils with each other, plaques are assembled.

The assembly of amyloid structures is typically measured using Thioflavin T (ThT), a fluorescence dye which binds amyloid structures specifically. When bound, an increase in fluorescence is observed (21).

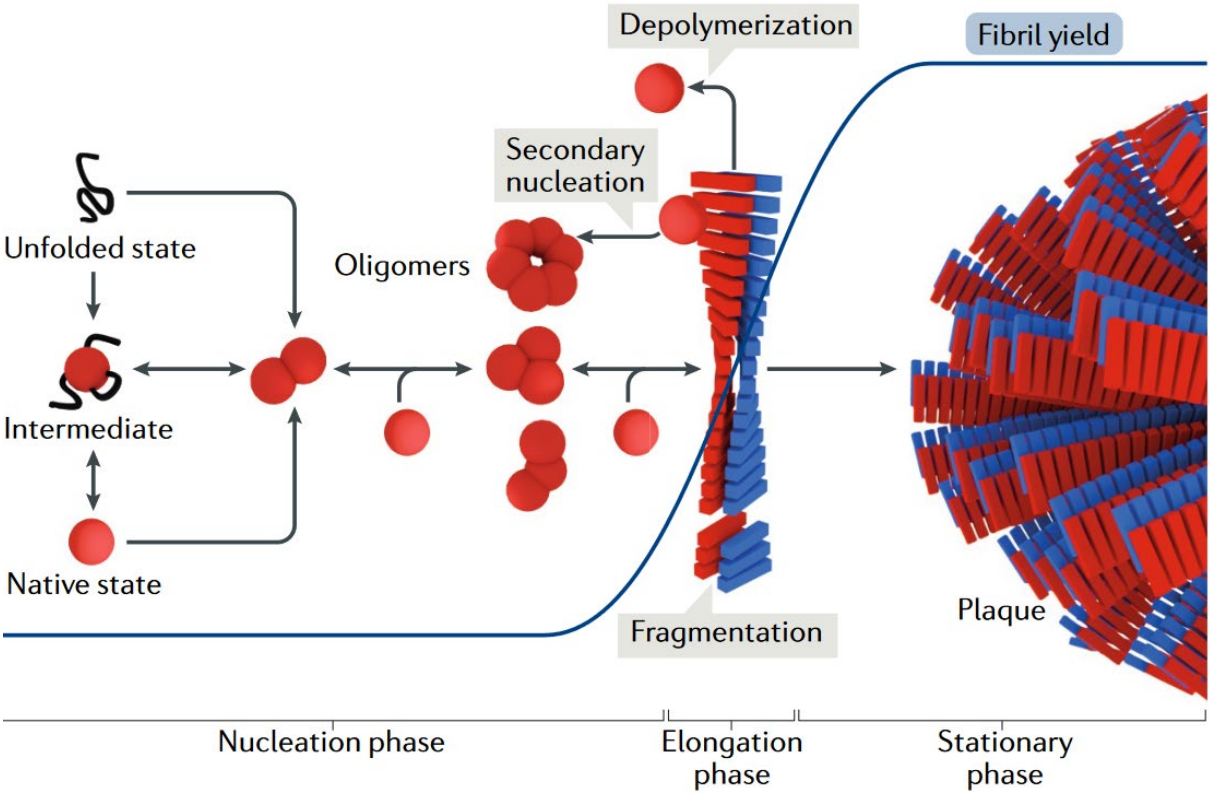

Figure 1.1: Amyloid formation – a scheme. Unfolded, intermediate and native state proteins are in dynamic equilibrium. They assemble into small oligomers which grow further into high-order oligomers and fibrils. These fibrils assemble with other fibrils to plaques. Via fragmentation, new fibril ends emerge which recruit free monomers. By this, new fibrils originate. The blue curve represents a typical *de novo* ThT curve. In the nucleation phase, fluorescence intensity is low, in elongation phase an exponential increase is observable which ends in a plateau. The image is taken from Iadanza *et al.* (5).

The amyloid state can be entered when a peptide or protein exposes its backbone amide N-H groups and C=O groups allowing the groups to connect via hydrogen bonds with other peptide or protein chains (12). Exposed backbones occur under certain conditions: denaturation (22), overexpression resulting in inclusion bodies (23), cleavage of a peptide from a protein (12) or overproduction of a intrinsically disordered protein (IDP) (24). Only the exposure of the described functional groups is not sufficient, but also the local concentration is critical (12).
Amyloids can exhibit functional properties especially in biofilm formation of bacteria (25, 26), protection against ultra violet radiation or oxidative damage in mammalians (27), or transmission success of the “Human Immunodeficiency Virus” (HIV) (28).

On the other hand, amyloids are associated with several severe human diseases.

1.2 Amyloid Diseases

Whenever a polypeptide chain fails to reach or maintain its three-dimensional structure, aggregation is a consequence (29). Folding and unfolding is connected to cellular processes like transport of molecules to organelles, control of the cell cycle or immune responses (29). This observation leads to the conclusion that the physiologically native fold of a protein correlates to a healthy organism while misfolding processes lead to malfunctions and hence to diseases (30). In mammals, most amyloid formation occurs with aging and is associated with diseases (12). Familial cases in which a pathogenic mutation leads to the overproduction of an amyloidogenic protein suggests a potential causal relationship between the formation of amyloids and amyloid toxicity (12), but most cases of disease appear sporadically.
There are over 40 different proteins or peptides which are known to assemble into amyloid fibrils associated with diseases (5, 15). These diseases include neurodegenerative disorders, like Alzheimer’s disease (AD) and Parkinson’s disease (PD), but also disorders affecting the peripheral tissues, like *Diabetes mellitus* Type 2 (T2DM). The presence of amyloid aggregates, located in- or extracellularly, is the hallmark of all of these diseases speaking for a causal connection between amyloid deposits and pathological symptoms, known as the amyloid hypothesis (31, 32). The toxicity of a protein is determined by its polymorphic structure and not by its primary sequence (33) and can result from losing the function of the certain protein or from the sequestration of other proteins (34).
Not only the buildup and presence of amyloid fibrils have been connected to the development and progression of diseases, but also oligomeric species (35-38). There are not only those which are dynamic, transient and heterogenous (39, 40), the so called on-pathway oligomers which assemble further into amyloid fibrils. Also, stable oligomers which are produced in side-

reactions exist, the so called off-pathway oligomers (41-44). In AD autopsy material, the soluble Amyloid β (Aβ) aggregated species show a higher correlation with the degree of dementia than the mass of Aβ plaques does. This suggests that the toxic species in AD might not be the clustering fibrils (36). Different multimers of Aβ were tested for toxicity in cell culture and the rodent brain and were shown to induce synaptic toxicity and dysfunction (45, 46). The same is true for α-synuclein (α-syn) associated with different synucleinopathies like PD (47) as well as for tau associated with tauopathies (48, 49). The more toxic impact of oligomers can be explained by their ability to diffuse faster through tissues and compartments whereas the amyloid plaques might bury toxic structural entities of the fibril.

In this thesis, I focus on synucleinopathies and T2DM as the amyloid proteins α-syn and islet amyloid polypeptide (IAPP), associated with these diseases, were my objects of research.

1.2.1 Synucleinopathies

The term “synucleinopathies” describes diseases associated with the aggregation of the 140-amino acid (aa) long protein α-syn. The most famous representatives of these diseases are PD (50), Lewy body dementia (51), and multiple system atrophy (52). Cellular location and pattern of α-syn deposition lead to different clinical phenotypes of diseases (53). Unifying features of synucleinopathies are autonomic failure related to neurodegeneration, orthostatic hypotension, urogenital dysfunction, gastrointestinal dysmotility, and thermoregulatory dysfunction (54) as well as rapid eye movement (REM) sleep behaviour disorder (55, 56). The pattern and severity of autonomic dysfunction with clinical symptoms differentiates the different synucleinopathies though symptoms often appear similar and overlap partially (53).
The physiological function of monomeric α-syn has been discussed intensively but is not well understood. Putative physiological roles of α-syn could comprise the regulation of synaptic plasticity and neuronal differentiation. This assumption was made due to observations including α-syn to be a presynaptic protein (57) and α-syn to interact with brain vesicles and phospholipid membranes (58). Synelfin, the bird orthologue of α-syn is upregulated during song learning processes requiring maximal neuronal plasticity (59). Additionally, α-syn is upregulated on mRNA expression level in early postnatal rat brain compared to adult rats. During this period of development, formation of synapses is of critical importance (60, 61). Synaptic development and maintenance may also be normal functions of α-syn (62). Another important physiological role of monomeric α-syn is the regulation of the biogenesis of dopamine (DA) which is reduced in patients suffering from PD. This could be explained by the role of α-syn to interact with tyrosine hydroxylase (TH) and by this inhibiting its activity as it

prevents TH of phosphorylation. When monomeric α-syn is not present anymore because it is in aggregated state, TH is present in its active state and increases DA synthesis. In case DA is too high, it cannot be removed from the cytosol sufficiently. Then, it accumulates as DA-quinone (DA-Q) and DA-associated oxyradicals which lead to neuronal cell death (63) (Figure 1.2).

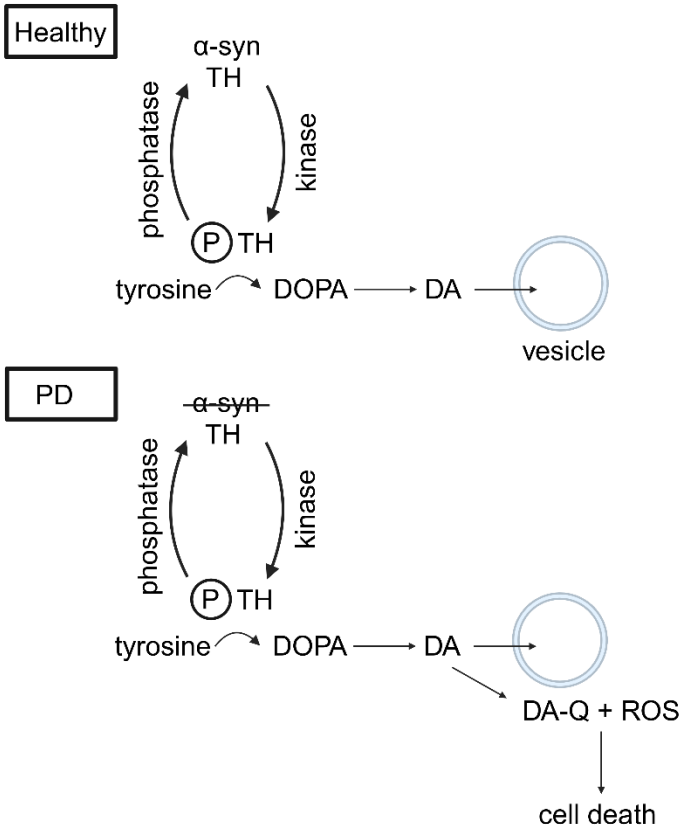

Figure 1.2: Proposed role of α-syn in dopamine synthesis in healthy people and PD patients. A-syn binds to dephospho-TH (TH). By this, it either inhibits TH phosphorylation and activity or α-syn activates a phosphatase or inhibits a kinase. In PD patients, a decreased level of soluble α-syn leads to a disinhibition of TH which elevates cytosolic dopamine (DA) in neurons triggering the generation of dopamine-quinone (DA-Q) and reactive oxygen species (ROS) which contributes to neurotoxicity. The figure was adapted from Perez *et al.* (63).

1.2.2 Diabetes mellitus Type 2

T2DM is a metabolic disease characterized by peripheral insulin resistance and later dysfunction of pancreatic β-cells. Consequences of these characteristics are defects in glucose metabolism and chronic inflammation. Of the amyloid diseases described so far in this thesis, T2DM is the disease which depends most on lifestyle. However, there are genetic dispositions favouring the development of the disease, but high caloric intake, nutrient composition, high air pollution and physical inactivity are substantial factors influencing the increasing prevalence in the population (64, 65). The number of human beings suffering from T2DM will rise to 700 million by 2045 (66). In 2035, 14.1% of the German citizens might be diseased (67) causing

not only mental and physical pain to the patients, but also a major medical economic grievance (68).

Insulin is produced by the β-cells of the Langerhans islets in the pancreas. Insulin stimulates the fusion of the glucose transporter 4 or 2 (GLUT4, GLUT2) harbouring cytoplasmic vesicles with the plasma membrane of the muscle cells or liver. This fusion leads to the increased uptake of glucose from the blood to the cell. The glucose homeostasis is regulated by the interplay of insulin and its antagonist glucagon which breaks down glycogen in the liver to glucose during fasting periods (69). When the secretion of insulin takes place, a 37-amino acid long peptide is co-secreted: IAPP. Under physiological conditions, IAPP is vital for maintaining glucose homeostasis, for controlling gastric emptying and for the suppression of glucagon release (70-72). In case of T2DM when the peripheral tissues lose their sensitivity to insulin, the demand increases. This increased demand for insulin increases the production of IAPP which has amyloidogenic properties. In high local concentrations, the probability to build oligomeric or fibrillar structures is high. It was shown that amyloid fibrils disrupt cell membranes which leads to an unregulated Ca^{2+} influx seriously affecting the normal functions of the cell (73). It was also observed that the mass of islet amyloid corresponded to the degree of β-cell destruction (74-76). A schematical overview is shown in Figure 1.3.

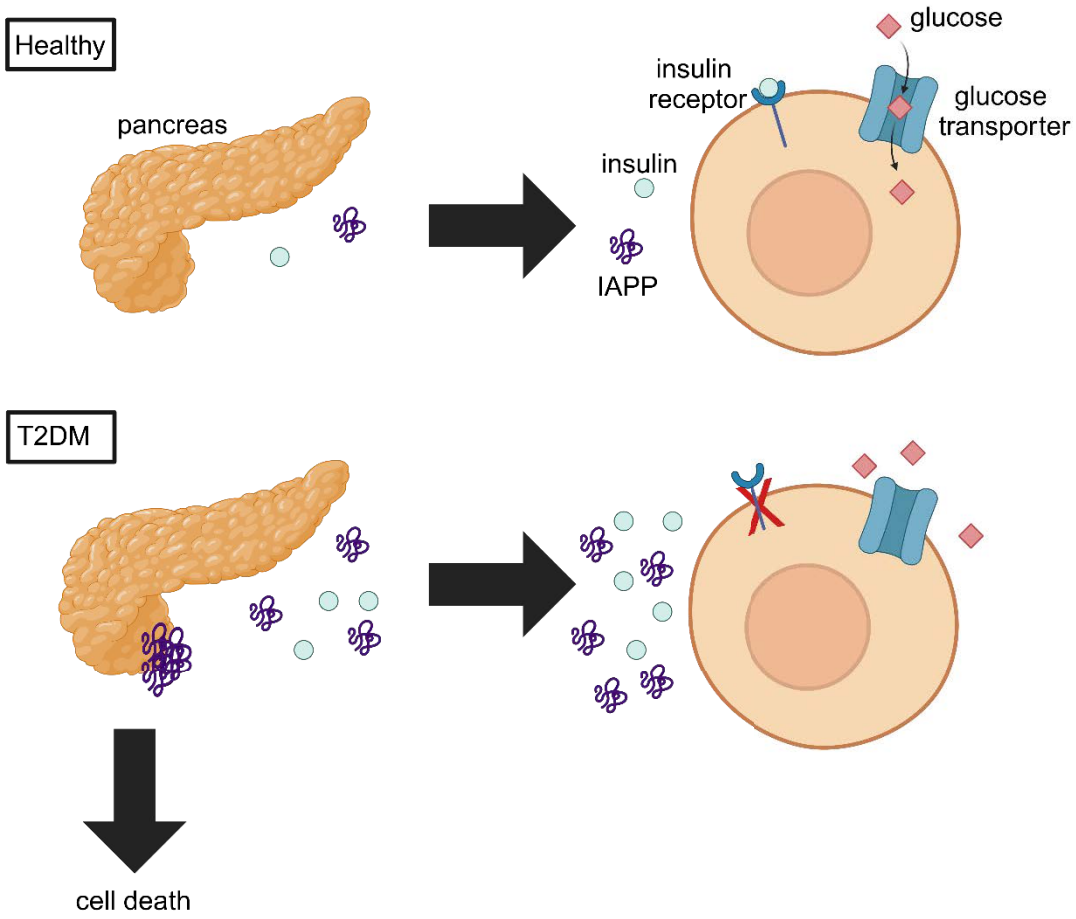

Figure 1.3: Comparative scheme of healthy and *Diabetes mellitus* Type 2 (T2DM) diseased mechanisms when blood glucose levels increase. When blood glucose levels increase, insulin is secreted. Islet amyloid polypeptide (IAPP) secretes at the same time. Insulin binds to its receptor on muscle or liver cells and glucose intake begins. In T2DM patients, insulin sensitivity is decreased. This triggers the Langerhans islets of the pancreas to secrete more insulin and simultaneously IAPP. Under high local concentrations, IAPP aggregates and has cytotoxic effects.

1.3 Treatment Approach

The quest for effective treatment of amyloid diseases is of great interest as the current approved treatments are of symptoms' improving, but not curing nature. As most of amyloid diseases occur with progressing age and the tendency of the global population to grow (77) and become older than the generations before (78), the amount of people suffering from amyloid diseases will increase dramatically.

1.3.1 Clinical Trials

Before an active agent enters the market and is accessible to patients suffering from distinct disorders, clinical trials are performed. When a promising candidate shows potency under

laboratory conditions and investors are found, it is ready to enter interventional studies which consist of four different phases (79). In Phase I studies, the active agent is tested in healthy voluntaries. This phase is used to examine the fundamental characteristics of the agent with regards to tolerability and safety in humans. In Phase II studies, the agent is tested for the first time in patients suffering from the specific disease. These studies focus on the dose. First observations on the efficacy are made. Phase III studies include many patients and are performed to gain information about the efficacy and tolerability with high precision. In Phase III studies, the patients are divided into two different groups of which only one group is treated with the active agent and the other with placebo. After Phase III studies, an active agent is ready to become a real medication. Phase IV studies are conducted when a drug has already entered the market. By this, seldom side effects can be examined.

1.3.2 Potential targets for therapy development

To approach the issue of increasing numbers of people suffering from amyloid diseases, the inhibitory options of amyloid formation must be considered. There are chemical interventions available like screening for small molecules disrupting fibril and oligomer formation. Necula *et al*. (80) investigated several small molecules and categorized them into three different classes: Class I compounds which inhibit $A\beta_{42}$ oligomerization without inhibiting fibrillization, Class II compounds inhibiting both and Class III compounds only inhibiting $A\beta_{42}$ fibrillization. In Class I there could be done another subdivision in compounds which actively promote $A\beta_{42}$ fibrillization and others which have no effect on $A\beta_{42}$ fibrillization. They could identify 29 small molecules capable of inhibiting $A\beta_{42}$ oligomer formation. Their compounds active in substoichiometric concentrations were azure C, basic blue 41 and meclocycline. Their data suggests that oligomers are amenable to drug treatment and the low dose concentration speaks for therapeutic feasibility. They identified 18 compounds to be effective in inhibiting $A\beta_{42}$ fibre formation. Of these, two, namely meclocycline and phenol red were reported previously to inhibit huntingtin aggregation (81) and IAPP fibrillization (82) suggesting them to be general aggregation inhibitors. From their data it can be suggested that selective inhibition of either $A\beta_{42}$ oligomerization or fibrillization is possible. Most Class I compounds appear to actively promote fibre formation. Since soluble Aβ aggregated species and not insoluble Aβ plaques are described as the more toxic species, the results are promising. Other compounds inhibiting amyloid formation are antibacterial substrates compared by Umeda *et al.* in 2016 (83) as the green tea compound epigallocatechin gallate EGCG, curcumin, scyllo-inositol, myricetin or the antibiotic rifampicin (83). In 1994 and 1996 Tomiyama *et al.* (84, 85) reported rifampicin to show strong inhibitory activities against Aβ fibrillization and toxicity. Rifampicin binds to oligomers and by this prevents them to interact with the membrane causing membrane damage resulting in excess influx of Ca^{2+} into the cells causing mitochondrial dysfunction and

formation of radical oxygen species (ROS). Following these studies researchers tested rifampicin against other amyloidogenic proteins, such as α-syn. Rifampicin as well inhibited α-syn fibrillization *in vitro* (86) and oligomerization within cultured cells (87). A problem of long-period intake of rifampicin is its drug-drug interactions causing other drugs to show reduced effects. Another setback of these promising results came 2013 when Molloy *et al.* (88) failed to prevent disease progression in mild-to-moderate AD patients. This only empowers rifampicin to act in preventive and early pre-symptomatic stages of neurodegenerative diseases.

Another way to inhibit amyloid formation can be achieved biologically. Overexpression of amyloidogenic proteins is one risk factor, but as long as the mechanism of how and why people express certain genes differentially is not understood, a therapeutic strategy at genetic levels is not feasible. Another risk factor is the cleavage of precursor proteins like in the case of the cleave of the amyloid precursor protein (APP) and its cleavage product Aβ and the amyloidogenic aftermath. Through the cleavage of APP by β-secretase and γ-secretase, the Aβ peptide is released (89). Introducing secretase inhibitors could theoretically be of interest, but unfortunately the usage of β-secretase and γ-secretase inhibitors resulted in detrimental cognitive effects (90-93). This suggests that the real culprit in AD is the decrease of soluble monomeric Aβ levels caused by the sequestration into brain Aβ aggregates (93) as soluble Aβ is crucial for modulation of synaptic function, neuronal growth and survival, neuroprotection against oxidative stress, neuroactive compounds, toxins and infective agents (94, 95).

An interesting candidate in clinical phase II is the D-peptide RD2, first described in 2014 (96) as a drug named contraloid, which eliminates oligomers of Aβ by probably stabilizing the monomeric state of Aβ. This was hypothesized due to the observation that the seeding potential of $A\beta_{42}$ was inhibited in presence of RD2. RD2 also improves cognitive performance of APP/PS1 mice, a mouse model which develops cognitive deficits and Aβ deposits at early age (97, 98). Even insoluble $A\beta_{42}$ plaques were reduced and no negative impact on behaviour was observed (97, 99, 100). In APPSL mice, a mouse model which exhibits increased expression of Aβ in the hippocampus, the oral intake of RD2 improved the results in the Morris water maze (101). In TBA2.1 mice, a mouse model of pyroglutamate-Aβ-induced motor neuro neurodegeneration, the intake improved their motor deficit (98). Beagles older than 10 years and cognitively impaired showed improvements in their short memory still two months after intake of RD2. RD2 has entered clinical phase II and is a promising candidate for curing AD (102).

1.3.3 Applied non-antibody treatment

There is no cure for any of the amyloid diseases. In case of AD, since 2002 there were conducted more than 400 studies testing over 200 candidates. Of these studies, 99.6% showed negative results (103). Nevertheless, there are approaches to improve the quality of living for patients.

In 1976, Davies and Maloney (104) postulated the deficit of cholinergic neurons in the basal forebrain in AD patients. These areas of the brain are associated with learning, memory, functional control, behaviour, and emotions. Overcoming this deficit is connected to the enhancement of cholinergic functions by utilizing acetylcholinesterase inhibitors (AchEIs). They block the depletion of acetylcholine. Drugs targeting the inhibition of depletion of acetylcholine are called antidementives, including the approved drugs rivastigmine and galantamine. Unfortunately, both drugs only offer a limited delay of cognitive depletion (105, 106). In a meta-study from 2015 (107) rivastigmine showed effects on cognitive improvement but due to many early terminations of the study and strong side effects including massive sweat and saliva production, urinary and stool incontinence, respiratory obstructions and tremor, the therapeutic benefits have to be considered individually. Galantamine improved cognitive features but led to a higher mortality. The German guideline suggests the administration of AchEIs in cases of mild-to-moderate AD. In moderate-to-heavy cases of AD, the administration of N-methyl-D-aspartate (NDMA) receptor antagonist memantine is suggested. It has positive effects on cognition, functions in the daily life and behaviour (108) while showing only few side effects. Another often prescribed class of drugs is extracts of ginkgo even though there is no clinical evidence of cognitive improvement (109). Ginkgo has properties of radical scavengers. However, ginkgo extracts are not standardized and therefore are considered as potentially dangerous, especially regarding interactions with other drugs (110). It is advised against the administration of piracetam, a cyclic derivate of γ-aminobutyric acid (GABA) which functions as an inhibitory neurotransmitter as the initial study suggesting cognitive improvement (111) was disproved by another independent study (112). Alternative therapies like music therapy (113) and exercise should not be underestimated in their potential. De la Rosa *et al.* (114) conclude from their studies on exercise in AD patients that lifestyle changes in presymptomatic and predementia disease stage may delay one-third of dementias worldwide. They come to this conclusion as exercise modulates inflammation, the synthesis and release of neurotrophins and the turnover of Aβ.

In case of synucleinopathies using the example of PD, there are treatments available improving motor symptoms. Treatments include levodopa preparations, dopamine agonists, and

monoamine oxidase-B (MAO-B) inhibitors. The selection of the individual optimal strategy requires considerations on benefits and risks (115). Levodopa usage results in more functional improvements, but higher risks of dyskinesia. In young individuals, anticholinergic agents can be of use, but side effects especially influencing cognition can occur. In the past, many physicians avoided levodopa for early PD treatment. They explained their caution because of misinformation generated from the interpretation of trial data and absence of clinical pathophysiologic context (116) but this changed (115). Almost half of the individuals treated with dopamine agonists, namely ropinirole and pramipexole, experienced impulse control disorders (117) resulting in the discontinuation of the study (118). A combination of treatments including uptake of MAO-B inhibitors blocking enzymes degrading dopamine, making the effects of levodopa endure longer. Exercise interventions focusing on gait and balance, strength training, aerobic exercise, music- and dance-based trainings (119), treadmill exercise (120) and tai chi (121) show beneficial effects. Another method is deep-brain-stimulation (DBS) which involves surgical placement of leads transcranially in the subthalamic nucleus or the globus pallidus interna. The leads are connected to a battery in the chest comparable to a pacemaker battery (115). During the last 25 years, the treatment evolved from experimental to standard. More than 150,000 PD patients are treated worldwide (122) experiencing improvements in motor abilities (123).

Other than AD and PD, T2DM is a disease which is preventable in many cases and in early-state still reversable. Dietary intake and physical exercise determine the energy balance. Most T2DM patients are overweight or obese (124) defined by their body mass index (BMI). The BMI is calculated by the division of the weight in kg by the height in m squared. BMI [kg/m^2] and its meaning as described by Marín-Peñalver *et al.* (125) is shown in Table 1.1.

Table 1.1:BMI [kg/m^2] and classification. Taken from (125).

BMI [kg/m^2]	Classification
18.5-24.9	Normal weight
25-26.9	Overweight grade 1
27-29.9	Overweight grade 2
30-34.9	Obesity grade 1
35-39.9	Obesity grade 2
40-49.9	Obesity grade 3 (morbid)
> 50	Obesity grade 4 (extreme)

Firstly, diet is key in prevention and treatment of T2DM. Many different diets like Mediterranean diet, vegetarian or vegan diet, low fat or low carbohydrates diet have been analysed with regards to manage T2DM treatment. The effects were modest. Advising people to follow diet plans like the mentioned diets is not effective (126). More profitable is to focus on the nutrient classes individually. The main determinant for glycaemic control is the source and amount of assimilated carbohydrates. It is preferable to only eat carbohydrates which come from raw sources like fruits, vegetables, legumes, whole grains, and dairy products (127). The suggested number of assimilated fibres is the same as for the general population (128). There are studies (126, 129) which indicate that a higher amount of fibre intake could be beneficial, but the number of fibres which should be assimilated is not feasible in reality. High-protein diets do not have a negative effect on blood sugar levels and can be utilized by T2DM patients to lose weight (130) while excessive fat and alcohol intake should be avoided (131, 132). Omega-3 fatty acids show a beneficial effect in preventing cardiovascular disease (133). In patients with hypertension sodium intake should be reduced (134). Besides diet, exercise is crucial for a healthy lifestyle without T2DM or an improved quality of living for T2DM patients. Physical exercise including resistance and aerobic exercise is associated with increased insulin sensitivity in tissues, improvement of glycaemic control, benefits in blood pressure, weight loss, and improvement of depression (127, 135, 136). Exercise also reduces the risk of developing peripheral neuropathy (137). Another important factor of cardiometabolic disease is sleep: 6 to 9 h per night is associated with a reduction of cardiometabolic risk factors (138).

Besides diet and exercise, there are also oral agents available. Metformin is the first-line treatment of T2DM. It has relatively mild side effects (125). Metformin decreases lipopolysaccharide (LPS) levels, both in circulation and liver. This is achieved by the change of composition of the microbiota of the gut and activation of mucosal adenosine monophosphate (AMP)-activated protein-kinase (AMPK) that both maintain the integrity of the intestinal barrier (125, 139). In the liver, metformin inhibits gluconeogenesis (140).
Another possibility is to treat T2DM with insulin secretagogues, particularly sulfonylureas and meglitinides. Both stimulate insulin secretion which is regulated by adenosine triphosphate (ATP) sensitive potassium ion channels in the membrane of pancreatic cells (141). Via receptor binding, both mentioned insulin secretagogues cause closure of the ATP-sensitive potassium ion channels and depolarization of the cell which results in elevated Ca^{2+} levels in the cytoplasm and subsequent insulin secretion. The main issues connected to the administration of this drug class are hypoglycaemia and weight gain. After some time of treatment, they lose their effectivity which is caused by beta cell failure (142, 143) explainable by the simultaneous release of IAPP. Another treatment is the injection of glucagon-like peptide 1 (GLP1). It is secreted when food uptake is happening and stimulates insulin secretion (144).

Insulin itself is used in all forms of *diabetes mellitus* (145). To gain enduring effects, long-acting insulin analogues are utilized. Those analogues show similar effects to insulin secretagogue meglitinide and have less side effects with regard to hypoglycaemia.
Bariatric surgery is another possibility to improve patients' conditions. In those with a BMI over 35 kg/m^2 which is denoted as "obesity grade 2", the bariatric surgery is a good option to lose weight fast.

Besides lifestyle interventions, chemical drugs and surgeries, another potent way to improve the lives of patients is immunotherapy.

1.4 Immunotherapy

Considering Aβ, α-syn and IAPP to have harming effects when aggregated, aggregated species are to target in improving the lives of patients and to find cure against the diseases associated with aggregates of the mentioned peptides. To solve this problem, immunotherapy is currently being researched to promote the breakdown of these aggregates (146-148). Immunotherapy can be divided into two groups: active and passive immunotherapy. Active immunotherapy includes vaccines while passive immunotherapy includes the use of exogenous antibodies.

1.4.1 Active Immunization

Active immunotherapy with amyloid plaques as target was a goal reported to be promising by Schenk *et al.* in Nature in 1999 (149). They reported their vaccine to be effective in reducing Aβ depositions in mice. On basis of these findings, the vaccine AN1792, targeting full-length Aβ was developed and sent to clinical trials. Unfortunately, administration of the vaccine led to severe immune response causing T-cell mediated meningoencephalitis in 6% of the patients' test group (150). The second generation of vaccines renounced T-cell epitopes and the promising candidate CAD106 was presented. The study was terminated in 2021 after brain volume loss and body weight loss as well as unexpected changes in cognitive decline were reported (151). In case of synucleinopathies, the search for vaccination strategies is also ongoing (152, 153). Two anti-α-syn vaccines, namely PD01A and PD03A (154, 155) are currently tested in Phase I studies. Both vaccines consist of small peptides in the native C-terminal region of human α-syn. In T2DM, vaccination is also an interesting aspect in targeting islet dysfunction and preventing the buildup of pathogenic aggregates. In 2020, Roesti *et al.* (156) introduced a potential vaccine specific against deposits of IAPP. In vaccinated mice, they observed less IAPP deposits and delaying onset of hyperglycemia.

1.4.2 Monoclonal Antibody Library Construction

Antibodies are glycoproteins in the group of immunoglobulins (Ig) which are used as defence against pathogens recognized by special epitopes or exogenous substances, the so-called antigens. Antibodies have special binding sites allowing the recognition of specific antigens. When a pathogen enters the organism, B-cells are activated and a cascade of their proliferation and differentiation is initiated. Each B-cell has their specificity programmed. More than 10^8 specificities are possible which is a result of the combination of different genes and the multitude of somatic mutations and recombination during evolution of the immune system. Fundamentally, an antibody consists of four polypeptide chains: two identical light and two identical heavy chains. They are connected via non-covalent bonds and disulfide bridges. The light chains exist in two different variants: the Kappa and the Lambda light chains. Both chains consist of a constant and a variable region. The variable region has a high variation of amino acid composition and thereby allows the high diversity. There are five different classes of antibodies relevant at different points of the immune response. There are three different classes of antibodies being monomers: IgD, IgE and IgG antibodies. The class of IgA antibodies describes antibodies which are in a dimeric form. IgM antibodies are pentamers. The antibody class of IgG is the most abundant class in the circulating blood. An IgG antibody is shown in Figure 1.4.

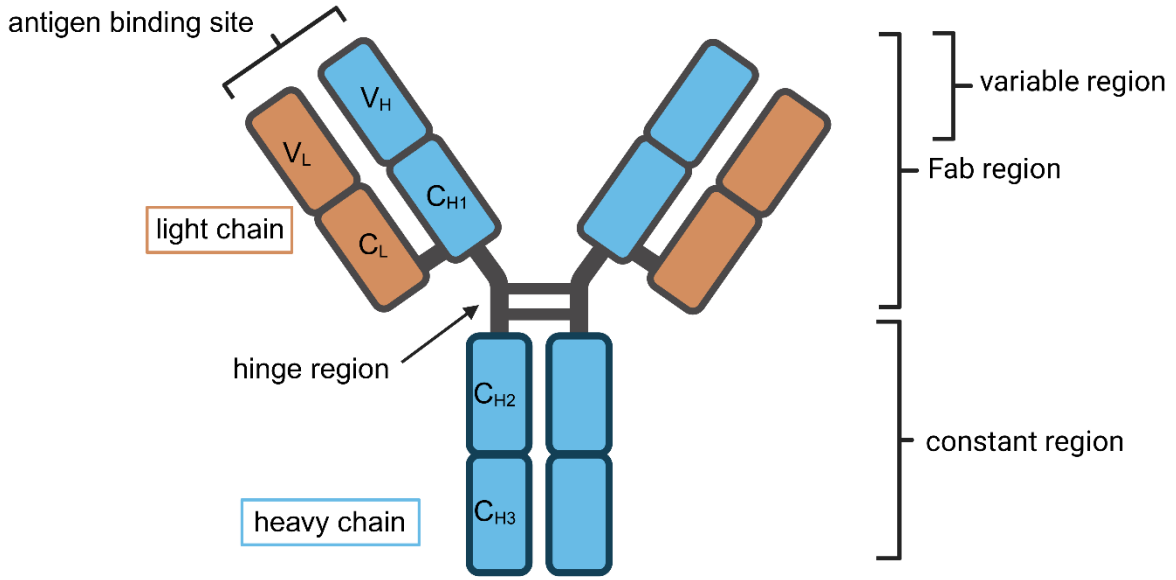

Figure 1.4: Scheme of an IgG antibody. IgG antibodies are monomers and consist of two heavy (blue) and two light (brown) chains. The antigen binding region, the variable region of the Fab region is very diverse.

The power of monoclonal antibodies was unleashed with the extraction of the genes encoding the variable regions in the late 1980s and their cloning (157, 158). Libraries have the potential to contain a large repertoire and diversity. Engineering monoclonal antibodies is useful to achieve enhanced pharmacological, easier storage conditions and better tolerability.

1.4.3 Passive Immunization

Due to the low effectiveness of active immunization, much effort has been put to passive immunization. Mechanisms which are generally considered here are the antibody opsonization of the antigen causing macrophage phagocytosis, antibody-mediated peripheral reduction of the target peptide, antibody-catalysed modification of secondary structure of the target peptide monomers and Fc-receptor-mediated outflow of antibody-antigen complexes across the blood-brain-barrier (BBB) (159-164).

In June 2021, the Food & Drug Administration (FDA) approved aducanumab for treatment of early AD. Aducanumab, commercially called aduhelm, is an IgG monoclonal antibody selective for the N-terminus of Aβ in aggregated forms (165). It lowers the plaque load in the brain (93). In November 2020, aducanumab was rejected from approval because of insufficient evidence (166). In the meantime, the Alzheimer's Association practised lobbyism for people and families with members suffering from AD and caretakers of AD patients (93). They longed for an effective treatment of AD and wished that aducanumab would be the long-awaited solution (93). The approval by the FDA is critizied extensively as it is based on an amendment in 1997 which allows the FDA to approve a new drug based on evidence of only a single study (167). Aducanumab was proven in other studies as not effective as no statistically relevant difference could be observed between the test groups (168), but is now the first available therapy on the market (159) whereas the effects are of at best delaying, not healing nature (169). In Europe, aducanumab is not approved due to the doubts mentioned (169).

Another FDA approved (170) monoclonal IgG antibody targeting soluble aggregated Aβ showing recognition across oligomers, protofibrils and insoluble fibrils is lecanemab, commercially called leqembi (171, 172). The observation that the Clinical Dementia Rating sum of boxes score (CDR-SB), a score quantifying dementia severity and progression in clinical trials, did not show a difference between the lecanemab and the placebo group after 18 months, but after 12 months gave confusion. Lecanemab showed more reductions of cognitive decline in carriers of apolipoprotein E4 (ApoE4), the biggest genetic risk factor for the development of sporadic AD (173), in comparison to non-carriers (171). In 17% of subjects, brain swellings were observed (172). Lecanemab does not cure AD, but delays the development (172). Whether an approval in Europe will happen is under review currently (172).

As reviewed by Song *et al.* (159), more monoclonal antibodies with the aim to delay cognitive decline in AD patients are tested in clinical studies currently.
The group which introduced a potential vaccination against deposition of IAPP also reports about an anti-IAPP monoclonal antibody which improved T2DM symptoms in mice (174).
Passive immunization is also interesting in PD. Recent results of Phase II trials of monoclonal antibodies were reported (175, 176). Unfortunately, both trials, investigating the effects of cinpanemab and prasinezumab, did not show benefits.

Another issue of monoclonal antibodies is their low capability to cross the BBB (177). All the issues that have not been solved so far in the fields of active and passive immunization underline the need for developing novel immunotherapeutic modalities.

1.5 Objective

The amyloid hypothesis postulates the causal relationship between accumulation of Aβ and clinical symptoms. This hypothesis can be transferred to other amyloid diseases like PD and T2DM. In the last 30 years, the goal was to antagonize Aβ accumulation. However, most of the compounds, excluding those which are still in clinical studies, failed to show therapeutic effects in patients and subjects treated at very early stages of the disease (93). The same is true for PD and T2DM. More basic research on potential inhibitors of nucleation processes and therapeutic strategies is necessary.

The first objective is the understanding of the mechanism of an inhibitor of α-syn fibril elongation. The inhibitor is composed of a monomer of α-syn and a hairpin-forming mutant of α-syn, denoted CC48. In previous studies our group proved the effectiveness of this fusion protein, but the mechanism was still uncertain. The data addressing this question is shown in Chapter 2.
The second objective is the introduction of a stable oligomer model of IAPP to be able to investigate the effects of IAPP oligomers on IAPP aggregation in general and on cells in comparison to IAPP fibrils. The data addressing this objective is shown in Chapter 3.
In Chapter 4, I show the establishment of a method, called “Proteolytic Antigen Cleavage-Mediated AmplificatioN” (PACMAN), to select proteolytically active monoclonal antibody derivatives from human blood donations. These antibodies offer the potential to not only achieve delays of disease development but could serve as a real treatment of amyloid diseases as they have many advantages compared to conventional monoclonal IgG antibodies.
Applying the PACMAN method and aiming to find antibodies against IAPP is topic of Chapter 5.

Overall, the objectives all contribute to the better understanding of amyloid diseases, prevention, and therapy – each one to its individual extent.

2 Fibril core regions in engineered α-synuclein dimer are crucial for blocking of fibril elongation

This chapter reflects content of the following publication.

2.1 Publication information

Celina M. Schulz*, Anne Pfitzer*, Wolfgang Hoyer

*: These authors contributed equally: Celina M. Schulz, Anne Pfitzer

Submitted to BBA Advances: August 31st 2023

Accepted by BBA Advances: November 9th, 2023

Available online since November 10th, 2023: https://doi.org/10.1016/j.bbadva.2023.100110

2.2 Abstract

Synucleinopathies like Parkinson's disease are neurodegenerative diseases which are associated with the deposition of fibrillar aggregates of the endogenous protein α-synuclein (α-syn). The inhibition of the elongation of α-syn fibrils is of great scientific interest and an option in the design of therapeutic strategies. Previously, we developed a disulfide-containing mutant of α-syn, called CC48, which inhibits fibril elongation by blocking of fibril ends. Surprisingly, wildtype (WT) α-syn molecules supported the blocked state, and a fusion of CC48 with WT α-syn, denoted WT-CC48, exhibited increased inhibitory potential. Here, we studied which regions of WT-CC48 are responsible for the strong inhibitory effect. To this end, we investigated a set of truncated versions of WT-CC48 by kinetic elongation assays, density gradient centrifugation, and atomic force microscopy. We show that in both the WT and the CC48 part of the fusion construct the hairpin region (residue 32–60) and NAC region (61–95), but not N- and C-terminal regions, are required for strong inhibition of fibril elongation. The required regions correspond to the segments forming the β-sheet core of α-syn fibrils. As α-syn fibrils typically consist of two protofilaments, the dimeric construct WT-CC48 provides the critical regions sufficient to cover the full β-sheetcore interface exposed at the fibril end, which can explain its high inhibitory efficiency. We suggest a mechanistic model of CC48-mediated inhibition of fibril elongation in which CC48 and WT α-syn cooperatively form an oligomer-like cap at the amyloid fibril end.

2.3 Introduction

A large number of proteins and peptides have been shown to undergo aggregation processes resulting in the loss of function and the build-up of toxic debris (34, 178-180). The aggregates often consist of fibrils with a highly ordered β-sheet core, the so-called cross-β amyloid structure (181, 182). Amyloid fibril formation is associated with many diseases, including Alzheimer's disease and Parkinson's disease (PD) (183-185). Synucleinopathies, like PD, are believed to be triggered by amyloid fibril formation of the 140 amino acid long presynaptic protein α-syn. In PD patients, it is found in Lewy bodies as insoluble inclusions (50, 186).

α-syn can assemble into several distinct fibril structures, referred to as polymorphs, which were termed, e.g., ribbons, rod, and twister (33, 187-189). Almost all α-syn fibril polymorphs resolved structurally up to this day consist of two protofilaments. In all polymorphs, the central region of α-syn comprising amino acids 30-100 contributes the largest part of the cross-β fibril core. The precise fold of the α-syn units within the fibril core, however, can be quite variable among polymorphs, including diverse protofilament interfaces.

Amyloid formation can be described as a mechanism of nucleated polymerization and is a multistep process, comprising primary nucleation, secondary nucleation and elongation (5, 190, 191). In the process of primary nucleation, monomers undergo a structural transformation to form growth-competent nuclei (192). In secondary nucleation, oligomer formation and conversion to a fibril seed is catalyzed on the surface of a pre-existing fibril (191, 193). Elongation describes the binding of a monomer to a fibril end and the structural conversion of the newly attached molecule into the cross-β amyloid structure (193, 194). As elongation is a fundamental reaction step of fibril growth, fibril mass cannot be generated under conditions that prohibit elongation. Therefore, the fibril end is an interesting target site to achieve inhibition of elongation and fibril formation in general. Moreover, the number of fibril ends is low compared to that of aggregated protein units, which may support inhibitory activities at low inhibitor concentrations (195). Different types of molecules have thus been designed and/or selected to occupy the fibril ends and block elongation, such as antibodies (196), peptides (197), or protein constructs (198-200).

Previously, our group introduced an α-syn double cysteine insertion mutant which specifically inhibits the elongation of wildtype (WT) α-syn fibrils (201, 202). The mutant, here called CC48, comprises the mutations of G41C and V48C allowing the formation of an intramolecular disulfide bond. The position of the disulfide bond was chosen to promote formation of a hairpin in the region comprising α-syn residues 32 to 60 (labeled here HP region, Figure 2.1) that was observed upon binding to the engineered protein AS69. Several studies showed that this region is of critical importance for α-syn aggregation: AS69 (203) and chaperones, peptides,

and foldamers targeting this region (204-206) inhibit α-syn aggregation; a mutant lacking from residues 36-42 (called “master manipulator” (207)) and 45-57 was shown not to aggregate under physiological pH (207, 208); the so-called preNAC segment (residues 47-56) (189) is critical for cell toxicity and fibril formation. The great significance of this region is emphasized by the fact that many disease-associated mutations are localized here, for instance E46K, H50Q, G51D, A53E and A53T (50, 51, 209-211).

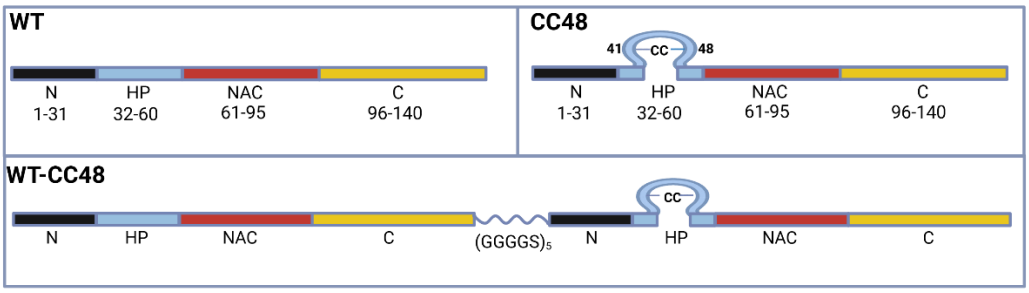

Figure 2.1: Wildtype α-synuclein (WT) illustrated by its characteristic regions: N-terminus (N) from residue 1-31 (black), hairpin (HP) from residue 32-60 (blue), non-amyloid-β component (NAC) from residue 61-95 (pink) and C-terminus (C) from residue 96-140 (yellow). The double cysteine mutant CC48 (G41C, V48C) only differs in the HP region (32-60). The WT-CC48-construct is composed of the wildtype sequence linked via a $(G_4S)_5$ linker to CC48.

CC48 is an intrinsically disordered protein just like WT α-syn, but in contrast to WT α-syn does not aggregate as long as the disulfide bond is closed (201). It inhibits elongation of WT α-syn fibrils, which could be analyzed with the framework of enzyme inhibition, with the fibril end acting as the enzyme and α-syn monomers corresponding to the substrate (202). CC48 acted as a competitive inhibitor. Interestingly, monomeric WT α-syn promoted inhibition presumably by stabilizing the blocked state at the fibril end. In line with this, a fusion construct of WT α-syn and CC48 was shown to drastically enhance the inhibitory effect (Figure 2.2A). In order to gain further mechanistic insight into α-syn fibril elongation and its inhibition, we here tested which regions of WT-CC48 are responsible for the strong inhibitory effect. For this purpose, we exploited the dimeric nature of the WT-CC48 fusion to generate fusion constructs with deletions of specific regions (Figure 2.1) either in the WT or the CC48 part. For this set of truncated versions of WT-CC48 we compared their potential to inhibit fibril elongation. The data demonstrates that the central regions of α-syn, which constitute the fibril core, are also most critical for inhibition of fibril elongation.

2.4 Results

2.4.1 Fusion of α-syn WT and the disulfide mutant CC48 inhibits fibril elongation by blocking fibril ends

To test the effect of inhibitors on fibril elongation, we applied a well-established assay in which 2.5 μM pre-formed fibrils (concentration in monomer units) are added to 25 μM α-syn monomers at neutral pH, followed by monitoring of fibril growth under quiescent conditions to suppress nucleation of new fibrils (202, 212). The amount of amyloid is detected using the amyloid specific fluorescent dye, Thioflavin T (ThT), which changes intensity dramatically upon binding to amyloids (Figure 2.2B). Inhibition of fibril elongation can be displayed by calculating the ratio of the initial rates of increase in ThT fluorescence with inhibitor (R) vs. without inhibitor (R_0) (Figure 2.2C). The dependence of R/R_0 on inhibitor concentration can be explained by a competition of inhibitor and WT substrate for the binding sites at the fibril ends (competitive inhibition model, more specifically the FI model, devised in (202)). In presence of WT-CC48, a complete inhibition of fibril elongation could be detected at nanomolar concentrations (Figure 2.2B and C). At the end of the kinetic assay, elongation of the pre-formed fibril seeds was confirmed by atomic force microscopy (AFM), with higher fibril length in the absence of inhibitor (Figure 2.2D and E).

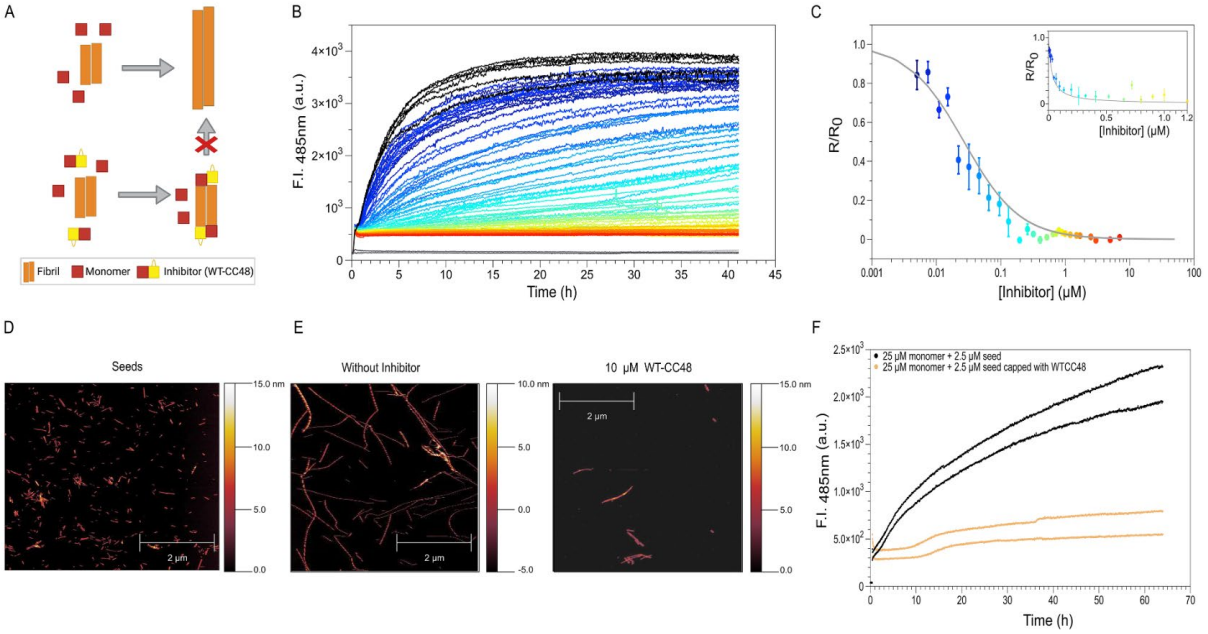

Figure 2.2: WT-CC48 inhibits fibril elongation at low substoichiometric ratios. **A:** Schematic overview of the suggested mode of action of WT-CC48 (202). Monomeric α-syn WT is shown as a red square, while the CC48 part is shown as a yellow square with a disulfide-bound. In the presence of pre-formed fibrils monomeric WT can bind to the fibril end and the fibril grows in length. However, in the presence of WT-CC48, WT-CC48 can get incorporated in the fibril structure and stops fibril growth. **B:** ThT assay performed at pH 7.4 with 25 μM α-syn WT monomers, 2.5 μM seeds and different inhibitor concentrations between 5 nM and 10 μM, shown in a color gradient from blue to red, under quiescent conditions. The measurement was performed in triplicates. Negative controls are shown in gray shades and positive control (NoWT-CC48) in black. **C:** Relative rates of fibril elongation were plotted against the inhibitor concentration (μM) with logarithmic scale or linear scale (inset). The solid line is a fit to a model of competitive inhibition (FI model). **D, E:** AFM of **D** fibril seeds and **E** fibrils generated in the ThT assays of α-syn WT without inhibitor and with 10 μM WT-CC48. **F:** ThT assay using seeds that were pre-incubated with a 1to1 ratio of WT-CC48 or α-syn WT. Pre-incubation was done overnight and seeds were isolated by centrifugation at 100.000 xg for 1 h. The measurement was performed in duplicates.

In our previous study, we hypothesized that binding of CC48-based inhibitors to the fibril end would lead to a templating-incompetent, i.e., blocked, state (202). To obtain further evidence for this mechanism, we tested if fibrils lose the ability to elongate upon pre-incubation with WT-CC48 followed by fibril isolation. The pre-formed fibrils were incubated with 25 μM WT-CC48 and as a control with α-syn WT monomers overnight at 37 °C under quiescent conditions. Subsequently, the fibrils were separated by centrifugation and used as pre-formed fibrils in the ThT assay. The sample containing pre-formed fibrils pre-incubated with WT-CC48 did not show any increase in ThT signal, in contrast to the control sample (Figure 2.2F). Two conclusions can be drawn from this experiment: I) WT-CC48 binds α-syn fibrils with high kinetic stability of the bound state, II) WT-CC48 inhibits fibril elongation. This is in line with WT-CC48 inhibiting fibril elongation by capping of fibril ends.

2.4.2 The WT part of WT-CC48 promotes inhibition of fibril elongation due to its HP and NAC regions

To identify the regions of the WT part of WT-CC48 that interact with the fibril end, different truncations of the WT part were generated. Structurally, α-syn is commonly divided into three distinct regions: the amphipathic N-terminus (amino acids 1-60), the central hydrophobic region termed NAC (amino acid 61-95), and the acidic C-terminus (amino acids 96-140) (Figure 2.1). In this study, we further subdivided the N-terminus into two parts: The very N-terminus (amino acids 1-31) and the HP region (amino acids 32-60). Our experimental goal was to investigate the relevance of these regions in the inhibitory mechanism of WT-CC48 on fibril elongation. To this purpose, eight fusion constructs were designed in which the N, HP, NAC or C region, or combinations thereof, were removed from the WT part of WT-CC48 (Figure 2.3).

Truncation of the N-terminus (WTΔN-CC48) did not change the inhibitory strength compared to the full-length construct (Figure 2.3A, SI Figure 2.1A). However, further removal of the HP region (WTΔNΔHP-CC48) led to a strong reduction of the capability of the inhibitor (Figure 2.3A, SI Figure 2.1B). Additional reduction of inhibitory strength is caused by the deletion of the NAC region (WTΔNΔHPΔNAC-CC48) (Figure 2.3A, SI Figure 2.1C). Truncation of the C-terminus only (WTΔC-CC48) showed a moderate decrease in inhibition strength, whereas additional deletion of the NAC region (WTΔNACΔC-CC48) strongly decreased inhibition potency (Figure 2.3B, SI Figure 2.2). From these results we infer that the removal of the NAC and HP regions lead to strong reductions in inhibition of fibril elongation. However, the removal of the N or C termini has only minor effects, which was confirmed by a fusion construct which lacks both termini (WTΔNΔC-CC48) (Figure 2.3C, SI Figure 2.3A). This construct shows the same inhibitory efficiency as full-length WT-CC48. Interestingly, removal of either the HP or

NAC region reduced the inhibitory effect of the fusion construct dramatically, indicating that both regions are required for potent inhibition (Figure 2.3C, SI Figure 2.3B,C).

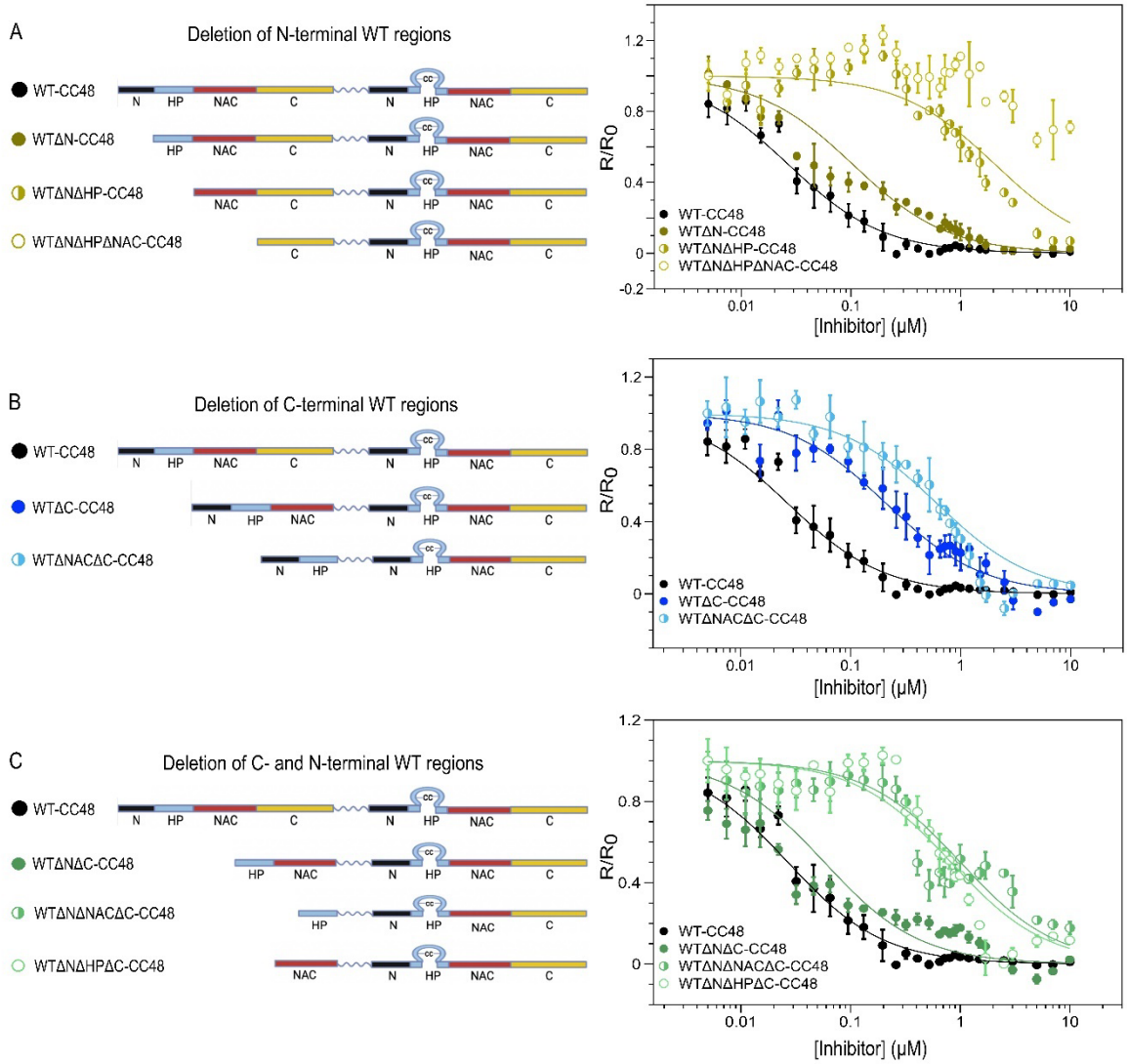

Figure 2.3: Truncations of α-syn WT regions in the WT-CC48 constructs affect inhibition of fibril elongation. Left, Schematic representation of the constructs visualizes the truncation of the N-terminal WT regions **A**, the deletion of the C-terminal WT regions **B** and the deletion of both C- and N-terminal WT regions **C**. The individual α-syn regions are displayed in different colors: N-terminus (residues 1–31) in black, hairpin region (residues 32–60) in blue, NAC region (residues 61–95) in pink and the C-terminus (residues 96–140) in yellow. The HP region of the CC48 part is shown as a loop. Right, relative rates of fibril elongation obtained from elongation assays (SI Figures 2.1–3) were plotted against the inhibitor concentration (μM). For the constructs WTΔNΔHPΔNAC-CC48, WTΔNΔHP-CC48, WTΔNACΔC-CC48, WTΔNΔNACΔC-CC48, and WTΔNΔHPΔC-CC48 the r/r0 values were normalized to 1.0 for the lowest inhibitor concentration, as the R/R0 values at low inhibitor concentrations were stable at a value above 1.0 for these constructs (see SI Figures 1–3 for the non-normalized data). Solid lines are fits to a model of competitive inhibition (FI model).

The inhibitory effects observed in the kinetic assay were confirmed by sucrose density gradient centrifugation (DGC) and AFM. Size distribution analysis by DGC showed that α-syn in the absence of inhibitor formed high molecular weight (HMW) assemblies which sedimented in the bottom fractions (Figure 2.4A). AFM confirmed that these aggregates were amyloid fibrils

(Figure 2.4A). 10 µM WTΔC-CC48, with only the C-terminus removed, ensured that α-syn remained predominantly in monomeric form (Figure 2.4B). The less effective inhibitor WTΔNΔNACΔC-CC48, which lacks the important NAC region, retained α-syn only partially in monomeric form (Figure 2.4C).

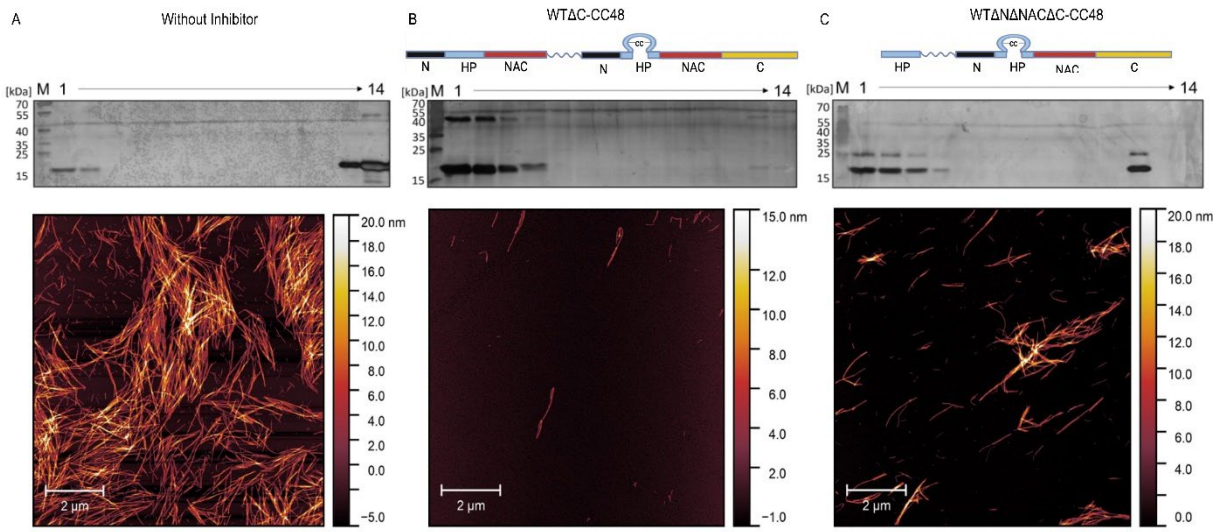

Figure 2.4: Different efficiency of inhibition of fibril elongation of truncated WT-CC48 constructs. Sucrose DGC and AFM imaging of samples at the end of the kinetic aggregation for α-syn WT without inhibitor **A**, with 10 µM WTΔC-CC48 **B**, or with 10 µM WTΔNΔNACΔC-CC48 **C**. DGC fractions, analyzed by SDS-PAGE (15% tris-glycine gel), are numbered from 1 to 14, with low-density fractions given lower numbers and higher density fractions higher numbers. M, marker. α-syn monomers are obtained in low-density fractions 1–4, whereas α-syn aggregates are found in high-density fractions 12–14 (213). In SDS-PAGE, α-syn runs at an apparent MW of ~17 kDa. WTΔC-CC48 and WTΔNΔNACΔC-CC48 co-migrate with α-syn in DGC and run in SDS-PAGE at apparent MWs of ~45 and 25 kDa,respectively.

2.4.3 The HP and NAC regions of the CC48 part of WT-CC48 are crucial for strong inhibition of fibril elongation

The inhibitor CC48 differs from WT monomer only by the introduction of two cysteines at position 41 and 48 and retains the intrinsically disordered nature of WT α-syn (201). The fusion of the inhibitor CC48 and its co-inhibitor, WT, increases the inhibition strength (202). Assuming that WT promotes inhibition by binding to fibril ends, the question arises whether the binding of the structurally similar CC48 to fibril ends occurs by the same mechanism. We wondered whether removal of the different regions in the CC48 part had the same effect on inhibition as truncation of the corresponding regions in the WT part. In one of the constructs, the C-terminal and N-terminal region of the CC48 part were removed (WT-CC48ΔNΔC). For this construct, the inhibition is in the same nanomolar range as for the full-length construct (Figure 2.5 and SI Figure 2.4A). In contrast, additional removal of the NAC (WT-CC48ΔNΔNACΔC) region decreased the inhibitory effect (Figure 2.5 and SI Figure 2.4B). We finally compared the effects of truncations of corresponding regions in the two parts of the fusion construct, WT or CC48.

Deletion of N- and C-terminus in either the WT or the CC48 part did not have a clear effect on the inhibitory potential (SI Figure 2.5A). However, the NAC region is required in both parts to maintain their high inhibitory potency (SI Figure 2.5B). Thus, we suggest that both, the WT part and the CC48 part, require the NAC and HP regions for optimal interaction with the protofilaments' cross-β core interfaces at the fibril end.

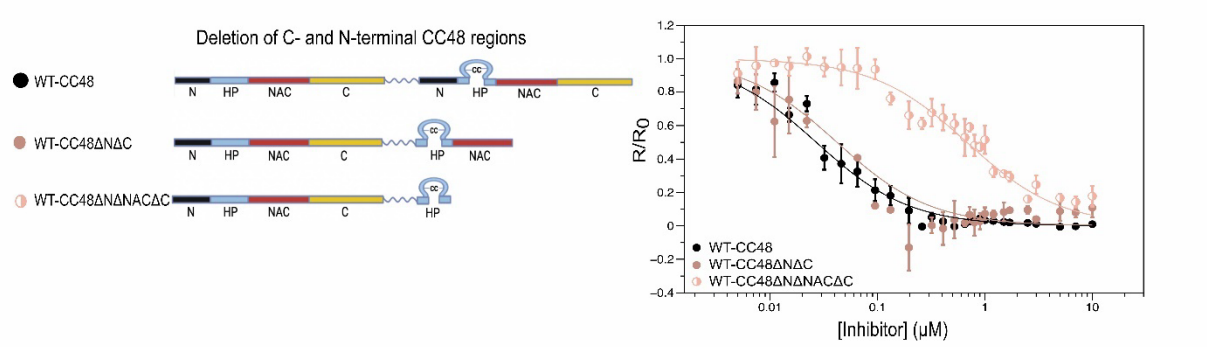

Figure 2.5: Truncations of CC48 regions of the WT-CC48 constructs affect inhibition of fibril elongation. Left, schematic representation of the constructs visualizes the deletion of C- and N-terminal regions. The different regions of α-syn are displayed in different colors: N-terminus (residues 1–31) in black, hairpin region (residues 32–60) in blue, NAC region (residues 61–95) in pink and the C-terminus (residues 96–140) in yellow. The HP region of the CC48 part is shown as a loop. Right, relative rates of fibril elongation obtained from elongation assays (SI Figure 2.4) were plotted against the inhibitor concentration (μM). Solid lines are fits to a model of competitive inhibition (FI model).

As a control experiment, we investigated two concentrations of all constructs on the same microtiter plate using the same seed preparation in a ThT experiment (SI Figure 2.6A-E) to ensure that any observed differences in inhibitory activity were not due to or compromised by differences between seed preparations. In addition, the insoluble vs. soluble fractions post aggregation were analyzed by ultracentrifugation followed by SDS-PAGE (SI Figure 2.6F-I). The data confirmed the previous observations regarding the relative inhibitory activity of the different fusion constructs.

2.5 Discussion

In this study we could confirm that WT-CC48 is a potent inhibitor of fibril elongation of α-syn. Comparing the IC50 values of all investigated constructs, we find that all constructs containing the HP and the NAC region in both WT and CC48 part show strong inhibition similar to that of full-length WT-CC48 (Figure 2.6A). This indicates that both, the HP and the NAC region (together residues 32–95), of both, the WT and CC48 part of the fusion construct, are necessary for the nanomolar inhibitory strength. In contrast, the N- and C-termini do not play an important role in CC48-mediatied inhibition of fibril elongation (Figure 2.6A). Regardless of the fibril polymorph, the region between residues 32–95 lies in the fibril core (189, 214-220). At the fibril ends, this region exposes the open cross-β structure as an interface for monomer attachment and as a template for their conversion into the fibril conformation. Since almost all

α-syn fibril polymorphs reported to date consist of two protofilaments, this open cross-β structure interface extends over two HP and NAC regions (Figure 2.6B). The observation that two HP and two NAC regions are required to maximize inhibition suggests that the full cross-β interface can be recruited for interaction with the inhibitor WT-CC48.

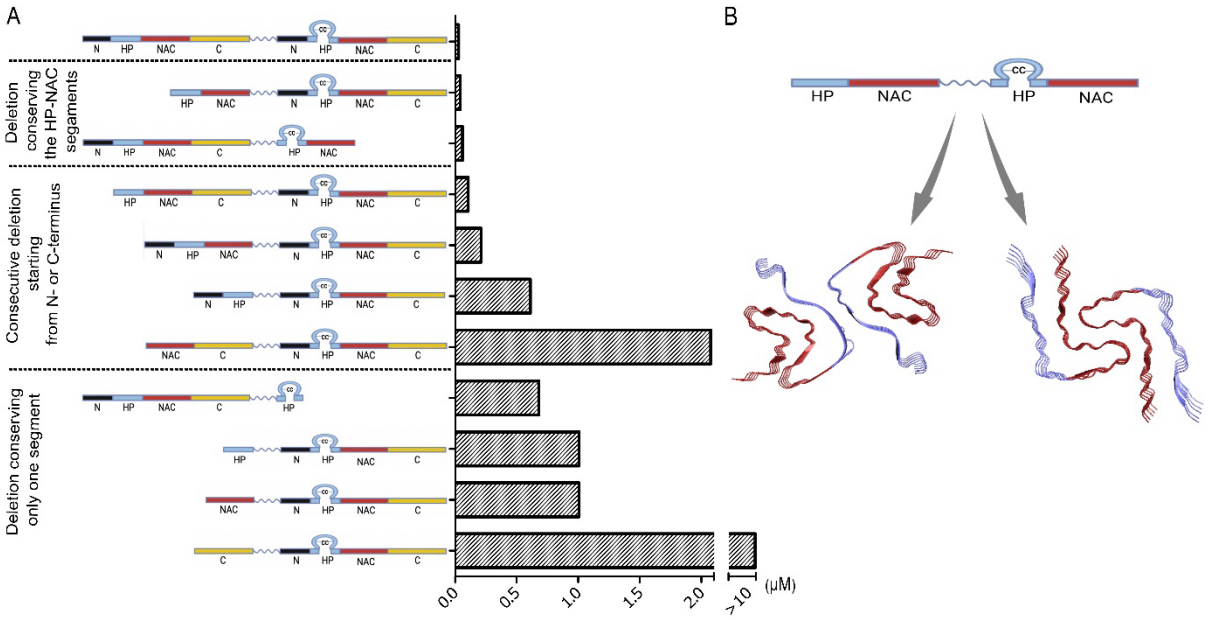

Figure 2.6: Overview of important regions in WT-CC48 for inhibition of fibril elongation. A: IC50 values of the investigated constructs derived from the fits to the competitive inhibition model. **B:** From the data, it can be concluded that in both parts of the constructs, WT and CC48, the HP and the NAC region are of great importance for the inhibition of the α-syn fibril elongation. Both parts, HP and NAC region, build the fibrillar core of α-syn fibrils, suggesting that elongation is driven by self-interactions between HP and NAC regions at the fibril end and in the inhibitor. The polymorphs shown here are taken from (189), PDB codes 6CU7 (rod polymorph) and 6CU8 (twister polymorph).

The data obtained here for the WT-CC48 fusion constructs allows to refine a model describing how CC48 achieves inhibition of fibril elongation, and how WT molecules support this activity. The model is illustrated in Fig. 7, in which CC48 corresponds to the inhibitor (yellow), whereas the supportive WT molecules are displayed in red. Note that the WT-CC48 fusion would in this scheme correspond to the linkage of the yellow CC48 inhibitor with a red WT molecule. The fact that the same regions are required for fibril inhibition as for fibril elongation supports a model in which CC48 establishes similar interactions with the fibril end as WT monomers but prohibits conformational conversion into the templating-competent structure of the seed fibril (Figure 2.7). CC48 may bind to one protofilament, engaging in largely the same interactions as a WT monomer would (Figure 2.7, point 2). A WT monomer can bind to the second protofilament and stabilize the CC48-bound state. However, due to the presence of CC48, it does not adopt precisely the same conformation as the other WT units in the seed fibrils, resulting in a fibril end that is not anymore templating-competent (Figure 2.7, point 3). Kinetic

analysis previously suggested that even more than one WT unit supports fibril end blocking (202). This can be explained by formation of an oligomer-like cap, consisting of a few α-syn molecules, on the fibril end (Figure 2.7, point 4). By the direct linkage of CC48 with WT within the fusion constructs, their cooperative action is exploited to achieve blocking of fibril ends at two orders of magnitude lower inhibitor concentration than for CC48 alone (202). The strategy applied here to interfere with fibril formation is based on recruitment of self-interactions between an amyloidogenic protein and an inhibitor that is a modified version thereof. The results indicate that for this type of inhibitor rather large protein segments are required to achieve sufficient inhibition activity. In the case of α-syn, we find that the HP and NAC regions are important to maximize the inhibitory efficiency. The particular need for HP and NAC once again highlights the role of self-interactions in amyloid assembly and inhibition. Fusion of the HP and NAC regions of WT α-syn might be a useful strategy to improve the activity of fibril elongation inhibitors.

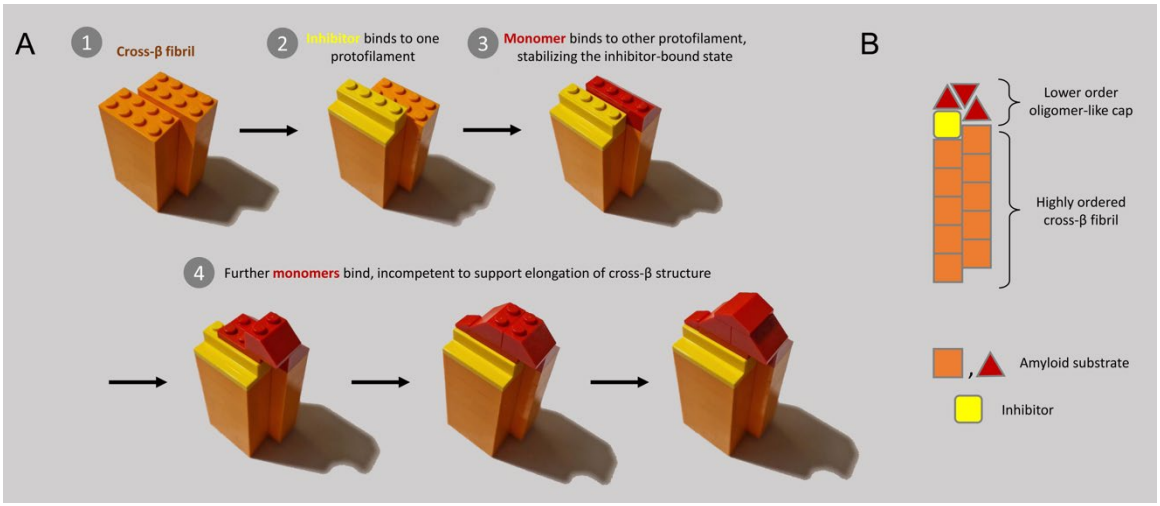

Figure 2.7: Model of CC48-mediated inhibition of fibril elongation. this scheme, CC48 corresponds to the inhibitor (yellow), whereas the supportive WT molecules are displayed in red. Note that the WT-CC48 fusion would in this scheme correspond to the linkage of the yellow CC48 inhibitor with a red WT molecule. 1) α-syn fibril polymorphs typically consist of two protofilaments, each exposing at the fibril end an open cross-β interface (pins on the click brick) consisting of HP and NAC region. 2) CC48 (yellow) may bind to one protofilament, engaging in largely the same interactions as a WT monomer (orange) would. 3) WT monomer (red) can bind to the second protofilament, stabilizing the CC48-bound state that is incompetent to template further elongation of the ordered fibril structure. 4) Further WT monomers can add to the fibril end, creating an oligomer-like cap.

2.6 Materials and Methods

2.6.1 Transformation, expression and purification of α-syn and the WT-CC48 variants

α-syn was encoded in the expression vector pT7-7 and expressed in *Escherichia coli* (*E. coli*) strain BL21(DE3). The WT-CC48 variants were encoded in the expression vector pET11-a purchased from GenScript Biotech and expressed in *E. coli* BL21(DE3). For transformation, the cells were thawed on ice for 10 min. Then, 10 ng of the plasmid was added to the cells and incubated on ice for another 10 min. After that, heat shock was performed by heating the cells to 42 °C for 60 s. The cells were immediately placed on ice again for 2 min. Preheated (37 °C) LB medium was added to the cells, and they were incubated at 37 °C 800 rpm for 1 h. The cells were plated on LB-agar plates supplemented with 100 µg/ml ampicillin and incubated at 37 °C overnight. The next day, a preculture of 50 ml 2YT supplemented with 100 µg/ml ampicillin was prepared and incubated at 37 °C and 160 rpm overnight. The next day, the main culture (500 ml in a 2 l Erlenmeyer flask) was inoculated with 5 ml of the preculture. It was incubated at 37 °C and 110 rpm until a OD_{600} of 0.6 was reached and induced with a final concentration of 1 mM IPTG. The culture was incubated for growth for 4 h at 37 °C and 110 rpm. The cells were harvested at 5000 x g, 4 °C for 20 min. The supernatant was discarded. The pellet was resuspended in 10 ml distilled water. Protease inhibitor was added. The cells were frozen at -20 °C. α-syn and fusion constructs were purified as described previously (202, 212, 221).

2.6.2 Elongation Assay

For seed preparation 25 µM of α-syn, 20 µM ThT, 0.04% NaN_3 and 20 mM MOPS pH 7.4, 50 mM NaCl were incubated in a volume of 1 ml with an added glass bead at 37 °C at 800 rpm for 72 h. Before addition to the 96-well plate, the seeds were pipetted to a 2 ml Eppendorf tube and sonicated at 70% for 30 s twice using UP200St Ultrasonic Processor from Hielscher.

In the elongation assay 25 µM α-syn monomers supplemented with 20 µM ThT, 0.04% NaN_3 in 20 mM MOPS pH 7.4, 50 mM NaCl were incubated with different concentration of the WT-CC48 constructs. Seeds were added to a final concentration of 2.5 µM. As controls, the seeded monomer without any WT-CC48 construct, the unseeded monomer without any WT-CC48 construct, the WT-CC48 constructs only and the seeds only were used. All components except for the seeds were added to a 96-well half-area, non-binding surface, black with clear bottom, polystyrene plate (3881, Corning) and incubated at 37 °C for 10 min. Then, the sonicated seeds were added to start the elongation kinetics. The ThT fluorescence was observed over 40 h.

The ThT signal was measured at 482 nm after excitation at 448 nm in a BMG FLUOstar Omega platereader. Measurements were done every 100 s in circle 1 to 110 and every 300 s in the following cycles. The fluorescence measurement was set in a ring with 12 points with a diameter of 3 mm.

For evaluation of elongation kinetics, the slope in the initial stages of the experiment (i.e., in the time window between 1 and 3 h after addition of seeds to monomers) was calculated, yielding the rate R. For comparing inhibitory activity between fibril elongation samples containing different seed preparation, we found it imperative to normalize the elongation rate to that of an uninhibited control (R_0), yielding R/R_0 (202). Some of the constructs exhibited R/R_0 values consistently above 1.0 at low inhibitor concentrations. We normalized these R/R_0 data sets to a value of 1.0 for the lowest inhibitor concentration investigated. The non-normalized R/R_0 data is shown in the SI. The R/R_0 data was fitted to a model of competitive inhibition (FI model), assuming that the inhibitor competes with WT molecules for the fibril end (202):

$$\frac{R}{R_0} = \frac{K_m + [\mathrm{M}]}{[\mathrm{M}] + K_m(1 + \frac{[\mathrm{I}]}{K_i})}$$

K_m and K_i are the dissociation constants of WT monomer or inhibitior, respectively, binding to the fibril end, and [M] and [I] are the concentrations of WT monomer and inhibitor, respectively. IC50 values were obtained from the fits to the FI model. In the elongation assay with WT-CC48 with capped seeds, 25 µM WT-CC48 were incubated with 25 µM (monomer concentration) pre-formed fibrils overnight at 37 °C, 800 rpm. The seeds were spun down for 1 h at 100,000 x g. The supernatant was discarded, and the pellet resuspended in 20 mM MOPS pH 7.4, 50 mM NaCl supplemented with 20 µM ThT and 0.04% NaN_3. The elongation assay was prepared as described above.

2.6.3 Preparation and SDS-PAGE of soluble and insoluble fractions after elongation assay

After the elongation assay serving as a further control (inhibitor concentrations: 0.5 µM and 5 µM), the soluble and the insoluble fractions were separated by ultracentrifugation at 100,000 x g for 1 h. The supernatant was transferred to a new reaction tube and the pellet resolved in 20 mM MOPS pH 7.4, 50 mM NaCl in a volume equivalent to the volume of the supernatant. The samples were diluted 1:4 with SDS-loading buffer (200 mM Tris–HCl pH 6.8, 400 mM DTT, 8% SDS, 0.4% bromophenol blue, 40% glycerol) followed by 15% Tris-Glycine-SDS-PAGE. PageRuler Protein Ladder was used. Gel electrophoresis was performed at 120 V.

2.6.4 Density gradient centrifugation (DGC) and SDS-PAGE

The samples from the 96-well plates after ThT measurements were taken and loaded on a discontinuous sucrose gradient and centrifuged for 3 h at 259,000 x g at 4 ◦C in a TLS-55 rotor (Beckmann). The sucrose gradient (as described in (213)) contained the following volumes and concentrations (w/w, from bottom to top): 300 µl of 60%, 200 µl of 50%, 200 µl of 25%, 400 µl of 20%, 400 µl of 15%, 150 µl of 10% and 400 µl of 5%. The gradient was layered stepwise in a 11 × 34 mm polyallomer centrifuge tube (Beckmann). After fractionating the gradient, each fraction was diluted 1:6 with SDS-loading buffer (50 mM Tris–HCl pH 7.4, 12% glycerol, 4% SDS, 2% β-mercaptoethanol) and analysed by 15% Tris-Glycine-SDS-PAGE. PageRuler Protein Ladder was used. Gel electrophoresis was performed at 120 V.

2.6.5 Atomic Force Microscopy (AFM)

AFM images were taken with a Bruker Multimode 8 (Billeric) with ScanAsyst-Air cantilevers (Camarillo) using the ScanAsyst PeakForce Tapping Mode in air. 10 µl of the protein solution was applied to a freshly cleaved mica and incubated for 10 min at RT under humified conditions. The sample was washed with 100 µl distilled water five times. Then, the sample was dried using gaseous N_2. Afterwards, the software Gwyddions was used for processing the AFM images.

2.7 Supplementary Information

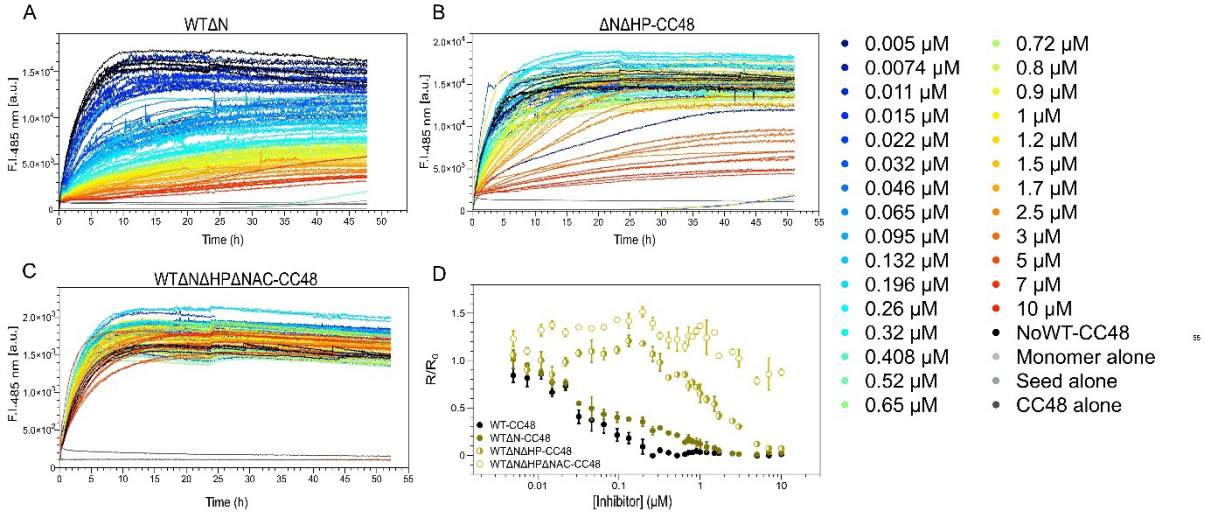

SI Figure 2.1: Elongation of α-syn in the presence of different WT-CC48 fusion constructs with deleted N-terminal WT regions Detection of the change in ThT fluorescence with 25 μM of monomeric α-syn incubated in the presence of 2.5 μM pre-formed fibrils under quiescent conditions at pH 7.4. Inhibitors: WTΔN-CC48 **A**, WTΔNΔHP-CC48 **B**, and WTΔNΔHPΔNAC-CC48 **C**. The assay was performed with different inhibitor concentrations from 5 nM to 10 μM shown in a color gradient from blue to red. The negative controls are shown in grey shades and the positive control (NoAS69) in dark red. **D:** Relative rates of fibril elongation (R/R0) obtained from elongation assays in panels A-C plotted against the inhibitor concentration.

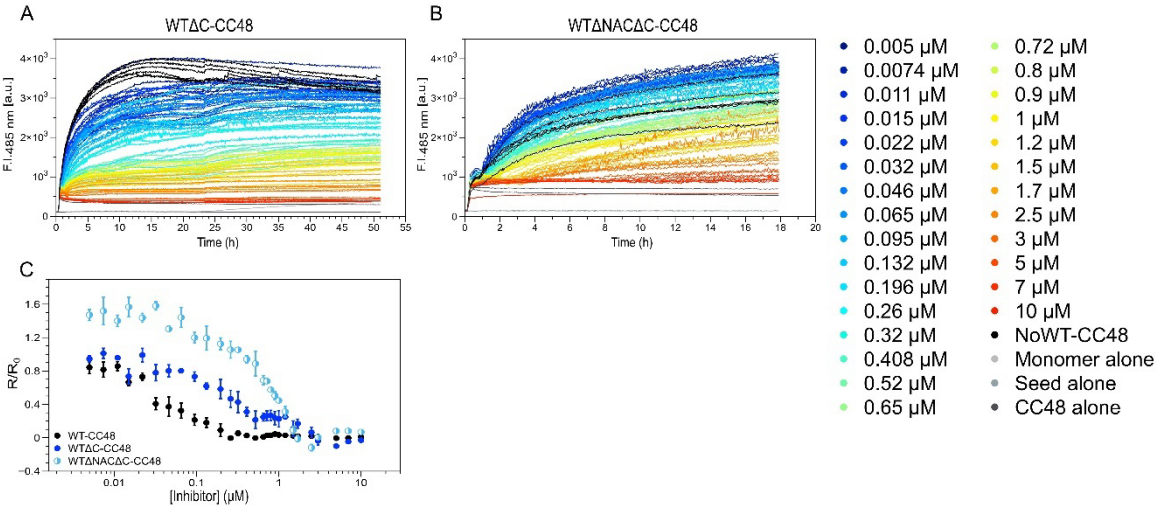

SI Figure 2.2: Elongation of α-syn in the presence of different WT-CC48 fusion constructs with deleted C-terminal WT regions Detection of the change in ThT fluorescence with 25 μM of monomeric α-syn incubated in the presence of 2.5 μM pre-formed fibrils under quiescent conditions with added inhibitor constructs. Inhibitors: WTΔC-CC48 **A** and WTΔCΔNAC-CC48 **B**. The assay was performed with different inhibitor concentration from 5 nM to 10 μM shown in a colour gradient from blue to red. The negative controls are shown in grey shades and the positive control (NoAS69) in dark red. **C:** Relative rates of fibril elongation (R/R0) obtained from elongation assays in panels A and B were plotted against the inhibitor concentration.

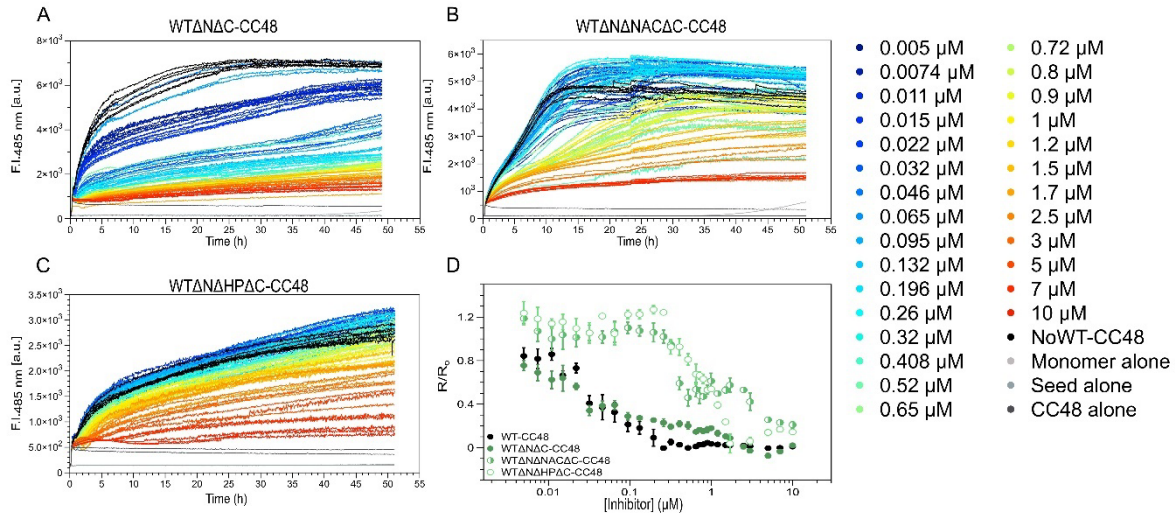

SI Figure 2.3: Elongation of α-syn in the presence of different WT-CC48 fusion constructs with deleted N-terminal and C-terminal WT regions Detection of the change in ThT fluorescence with 25 μM of monomeric α-syn incubated in the presence of 2.5 μM pre-formed fibrils under quiescent conditions with added inhibitor constructs. Inhibitors: WTΔNΔC-CC48 **A**, WTΔNΔNACΔC-CC48 **B**, and WTΔNΔHPΔC-CC48 **C**. The assay was performed with different inhibitor concentration from 5 nM to 10 μM shown in a colour gradient from blue to red. The negative controls are shown in grey shades and the positive control (NoAS69) in dark red. **D:** Relative rates of fibril elongation (R/R0) obtained from elongation assays in panels A-C were plotted against the inhibitor concentration.

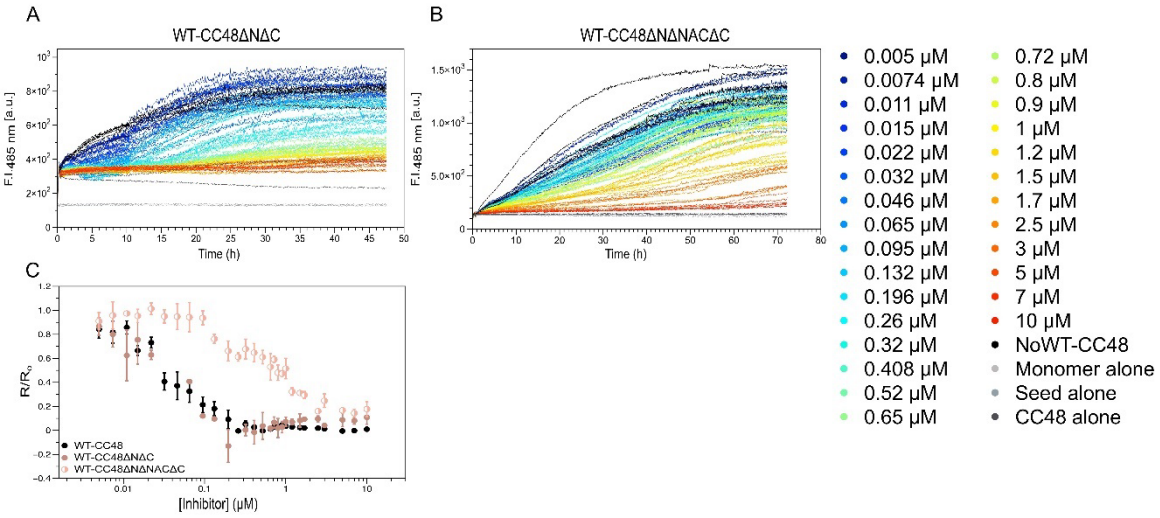

SI Figure 2.4: Elongation of α-syn in the presence of different WT-CC48 fusion constructs with deleted N-terminal and C-terminal CC48 regions Detection of the change in ThT fluorescence with 25 μM of monomeric α-syn incubated in the presence of 2.5 μM pre-formed fibrils under quiescent conditions with added inhibitor constructs. Inhibitors: WT-CC48ΔNΔC **A** and WT -CC48ΔNΔNACΔC **B**. The assay was performed with different inhibitor concentration from 5 nM to 10 μM shown in a colour gradient from blue to red. The negative controls are shown in grey shades and the positive control (NoAS69) in dark red. **C:** Relative rates of fibril elongation (R/R0) obtained from elongation assays (SI Figures 4A-B) were plotted against the inhibitor concentration.

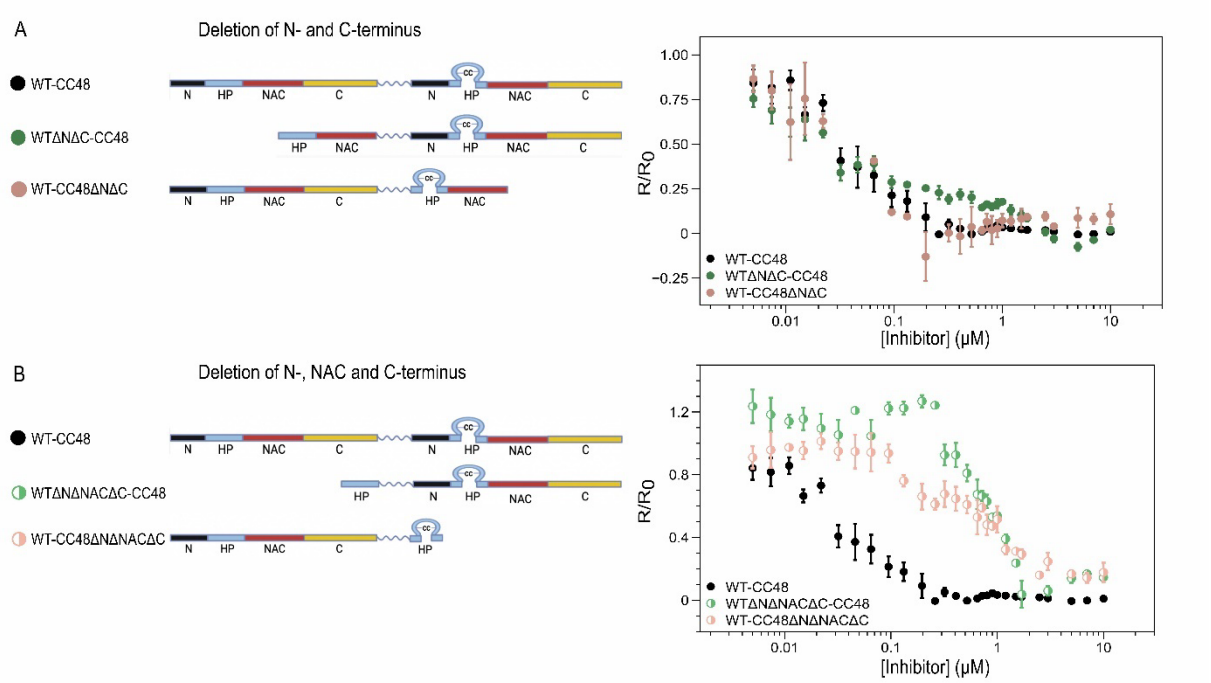

SI Figure 2.5: Truncations of the same regions of α-syn WT and CC48 results in similar inhibition efficiency. Left, schematic representation of the constructs visualizing the truncation of the N- and C- terminus in the WT part and the CC48 part **A**, as well as the deletion on N-, NAC and C-terminal region in the WT part and the CC48 part of the fusion construct **B**. Different regions of α-syn are shown in different colours: N-terminus (1-31) in black, hairpin region (HP) in blue (32-60), NAC region in pink (61-95) and C-terminus in yellow (96-140). Additionally, the HP region of the CC48 part is shown as a loop. Right, relative rates of fibril elongation were plotted against the inhibitor concentration.

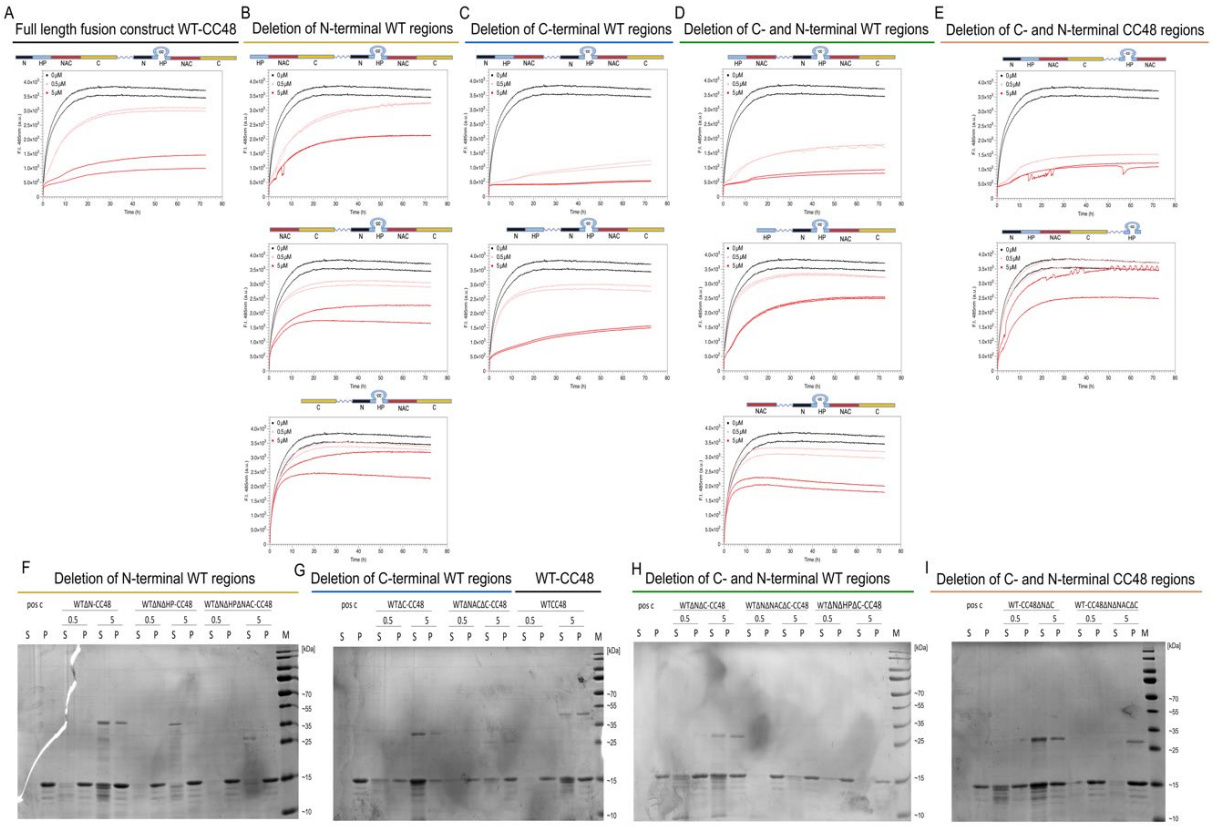

SI Figure 2.6: Validation of inhibitory potentials of all constructs using the same seed preparation. A-E: Two concentrations (0.5 µM (light red) and 5 µM (red)) of all constructs were investigated on the same microtiter plate using the same seed preparation in a ThT experiment. Detection of the change in ThT fluorescence using 25 µM of monomeric α-syn incubated in the presence of 2.5 µM pre-formed fibrils under quiescent conditions at pH 7.4 in absence (black) and presence of inhibitors (red shades). The inhibitors are classified in full length WT-CC48 **A**, deletion of N-terminal WT regions **B**, deletion of C-terminal WT regions **C**, deletion of C- and N-terminal WT regions **D** and deletion of C- and N-terminal CC48 regions **E. F-I:** Insoluble vs. soluble fractions post aggregation, analysed by SDS-PAGE (15% tris-glycine gel), denoted S for soluble (supernatant) fractions and P for insoluble (pellet) fractions. M, marker. The inhibitors are classified in deletion of N-terminal WT regions (F), deletion of C-terminal WT regions and full length WT-CC48 **G**, deletion of C- and N-terminal WT regions **H** and deletion of C- and N-terminal CC48 regions **I**. Alongside all inhibitor samples a positive control (pos c, without inhibitor) is applied on each gel.

3 An islet amyloid polypeptide oligomer model for the study of amyloid aggregation and oligomer induced pathophysiology

This chapter reflects content of the following publication.

3.1 Publication information

Anne Pfitzer*, Celina M. Schulz*, Robin Backer, Filip Hasecke, Wolfgang Hoyer

*: These authors contributed equally: Anne Pfitzer, Celina M. Schulz

To be submitted to FEBS Journal

3.2 Abstract

Type 2 *diabetes mellitus* (T2DM) is a multifactorial metabolic and widespread disease. In patients' pancreas islet amyloid polypeptide (IAPP) is found as aggregates. The aggregation process and toxicity of different aggregate species of IAPP are under intense investigation. As for other disease-related amyloidogenic proteins, oligomeric species of IAPP have been suggested to exhibit cytotoxic activity. Here, we developed an IAPP model, denoted dimIAPP, which assembles into curvilinear oligomers (dimIAPP-O) and remains stable in this conformation. DimIAPP is an engineered dimer of an IAPP cysteine mutant (C2S, C7S) connecting two monomers via a flexible $(G_4S)_4$ linker. We investigated the effect of this stable oligomer model, first, on the amyloid aggregation of IAPP and second, on stress gene transcription in pancreatic rat cells RIN-m5f. The aggregation of IAPP is partially inhibited by dimIAPP-O, indicating that it is not being incorporated into IAPP fibrils in the same manner as IAPP monomers but instead prevents amyloid assembly. DimIAPP-O as well as IAPP fibrils trigger stress responses in RIN-m5f cells, albeit IAPP fibrils upregulate more stress genes than dimIAPP-O do. We conclude the model to be a useful tool to gain further insights in the aggregation of IAPP and to characterize the effect of stable, curvilinear oligomers on cells.

3.3 Introduction

Loss of β-cell function in T2DM is caused by a multitude of insults. Islet amyloid was found in the pancreatic parenchyma of more than 90% of T2DM patients and is believed to inflict cytotoxicity (222-229). The main constituent of islet amyloid is IAPP, a 37-residue long peptide hormone co-secreted with insulin (230). It plays a role in gastric emptying (231), glucose homeostasis (232), regulating satiety (233) and suppression of glucagon release (234). Amyloid deposits are found in a plethora of diseases, including T2DM, Alzheimer's disease

and Parkinson's disease. The unifying feature of these peptides is the characteristic cross-β structure adopted by their amyloid aggregates (235-237). In T2DM, prominent hyaline lesions were first described in 1901, more than 120 years ago (238, 239), in the pancreas of a young patient suffering from hyperglycemia and was later identified as amyloid depositions of IAPP in 1986 (240, 241).

Oligomeric IAPP species have gained increased attention as they might be important players in the pathogenic processes (35, 70, 226-229, 242-247). In support of this, a poor correlation of IAPP amyloid load with β-cell death was observed (248). Different natural and synthetic IAPP oligomer preparations were characterized and found to exhibit variable levels of toxicity, e.g. to induce apoptosis (249) or disrupt the cell membrane (250). The exact linkage between IAPP oligomer formation and toxicity is unknown. It has been suggested that IAPP oligomers are related to the formation of a membrane channel inducing an upregulated Ca^{2+} influx or membrane disruption causing stress of the endoplasmic reticulum (ER) (73, 251). However, oligomers are difficult to study, due to their transient nature (252), low population under standard conditions, and structural heterogeneity (253). This complicates the identification of the most critical species in amyloid diseases (254, 255). It also leads to an uncertainty regarding the position of different types of oligomers on or off the pathway towards amyloid fibrils (253, 256-258). Therefore, it is crucial to invent reliable models for studying oligomers.

Studies on oligomers are not only of great interest in T2DM, but also in over 50 other diseases (5) associated with the assembly of amyloids, like Alzheimer's disease (259-261). For Alzheimer's Amyloid-β (Aβ) it was shown that low-molecular weight species are more toxic than monomers and fibrils (262). Previously, our group invented a model for oligomer-forming Aβ40, called dimAβ (263-265). DimAβ is a polypeptide containing two units of Aβ40 connected by a flexible glycine-serine linker. The linkage of two Aβ units does not affect Aβ conformation, but results in an increased local concentration which promotes the highly concentration-dependent oligomer formation. DimAβ assemble into stable curvilinear oligomers that faithfully reflect the properties of off-pathway Aβ oligomers previously observed in many labs, including the binding to dendritic spines and induction of Tau missorting, a key factor in tauopathies (264, 266). DimAβ oligomers provided insight into the properties of off-pathway Aβ oligomers and their relationship to amyloid fibrils (263-265). For example, metastable dimAβ oligomers bind to the surface of Aβ fibrils and inhibit secondary nucleation (265). Furthermore, studies employing dimAβ allowed to identify the importance of low pH, as present in endosomal/lysosomal compartments, for rapid Aβ oligomer formation (264).

IAPP oligomer models are of great importance to improve our understanding of this type of aggregate species. As stable IAPP oligomers cannot be obtained directly from monomeric human IAPP for the reasons stated above, we tested here if oligomers can be obtained using

an IAPP construct analogous to dimAβ. This approach is motivated by the sequence similarity of IAPP and Aβ (267, 268). Moreover, certain Aβ and IAPP oligomers may be structurally and functionally related, as suggested by the cross-reactivity of oligomer-specific antibodies (35) . We introduce an engineered dimer of an IAPP mutant called dimIAPP (Figure 1A), in which both subunits are connected via a flexible linker in a head-to-tail fashion. With the help of this model, we obtained insights into the effect of oligomers on IAPP aggregation and pathophysiology.

3.4 Results

3.4.1 DimIAPP assembles into curvilinear oligomers

We developed an artificial dimer of an IAPP mutant called dimIAPP (Figure 3.1A), in analogy to the design of the artificial Aβ dimer dimAβ. In dimIAPP, two IAPP units are connected by a $(G_4S)_4$ linker. The linker is supposed to provide sufficient flexibility to the IAPP units, such that they are not restricted in adopting all assembly types accessible to natural IAPP. In order to avoid formation of aberrant disulfide bonds, the cysteines at positions 2 and 7 of both IAPP units were exchanged to serines. This modification leads to loss of the disulfide loop connecting IAPP residues 2 and 7 under oxidizing conditions. In fibrils, amino acids (aa)1-12 are not part of the core but located at the periphery (237, 269, 270), indicating that the Cys-to-Ser exchanges are not essential for IAPP aggregation. This is confirmed by kinetics studies (271), which show that loss of the disulfide loop actually promotes IAPP amyloid fibril formation. Furthermore, we note that dimIAPP is not C-terminally amidated.

While IAPP formed amyloid fibrils upon incubation in 50 mM MES pH 6.5, 50 mM NaCl, dimIAPP assembled into spherical and curvilinear oligomers, as imaged by atomic force microscopy (AFM) (Figure 3.1B, SI Figure 3.1). These oligomers, which we name dimIAPP-O, are reminiscent of the metastable off-pathway oligomers formed by dimAβ (263-265) (Figure 3.1C). DimIAPP-O exhibit a tendency to assemble into clusters (Figure 3.1B, SI Figure 3.1), which has also been observed for dimAβ oligomers at this slightly acidic pH (264).

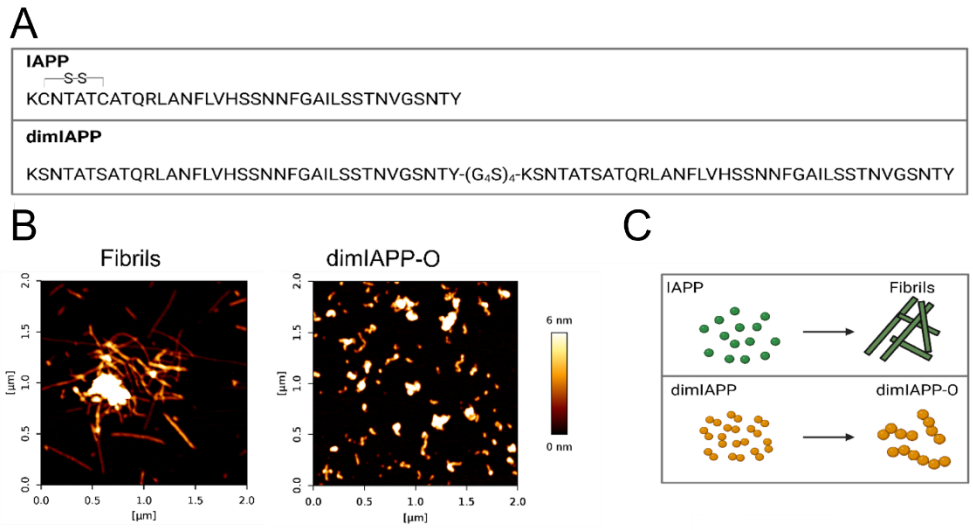

Figure 3.1: Model system for IAPP oligomers utilizing a tandem IAPP construct called dimIAPP. A: Amino acid sequences of IAPP and dimIAPP. dimIAPP is an engineered dimer of $IAPP_{C2S,C7S}$. The subunits are connected via a flexible $(G_4S)_4$ linker to provide conformational freedom. **B**: Morphologies of IAPP fibrils and dimIAPP-O after 16 h of quiescent incubation at 37 °C in 50 mM MES pH 6.5, 50 mM NaCl, imaged using atomic force microscopy (AFM). Colour scale: height. **C:** IAPP forms amyloid fibrils while dimIAPP forms stable oligomers.

3.4.2 DimIAPP-O inhibit aggregation of IAPP

We next investigated the effect of dimIAPP-O on IAPP amyloid fibril formation. To this end, we performed aggregation kinetics using the amyloid specific dye thioflavin T (ThT). DimIAPP-O, prepared by pre-incubation of dimIAPP for 16 hours, did not exhibit ThT fluorescence over the course of 10 h under shaking conditions (Figure 3.2A, SI Figure 3.2D over 25 h) and remain oligomers (Figure 3.2I). In contrast, initially monomeric IAPP exhibits an increase in ThT fluorescence (Figure 3.2A, grey curve) attributed to the formation of fibrils (Figure 3.2J) containing a cross-β structure. The ThT-negativity is a feature that distinguishes dimIAPP-O from dimAβ oligomers but does not provide insights into the structural organization of these oligomers, as the molecular basis of ThT binding to oligomers lacking cross-β structure is not well understood.

The addition of dimIAPP-O to 3 µM monomeric IAPP inhibits the aggregation of IAPP when comparing monomer concentrations of IAPP and dimIAPP-O, namely 2 molecules of IAPP equilibrate 1 molecule of dimIAPP-O from the monomeric point of view (Figure 3.2B-H). This indicates dimIAPP-O to act differently from IAPP monomers.

Adding sub-stoichiometric concentrations of dimIAPP-O (in monomer units) to 3 µM monomeric IAPP decelerates or completely inhibits the aggregation of IAPP (Figure 3.2B-E). This suggests small concentrations of dimIAPP-O to actively stop the nucleation or growth of the substrate IAPP.

However, when adding dimIAPP-O in higher ratios than 1:1 to 3 µM IAPP, we observe no difference in the lag time in comparison to the 3 µM IAPP control (Figure 3.2F-H). This indicates that in high concentrations dimIAPP-O do not interfere with IAPP. Considering the higher plateau and the observation to act differently as monomers, dimIAPP might get triggered by IAPP monomers to leave their off-pathway state and built ThT-positive cross-β structures. In line, the formation of fibrils by dimIAPP was observed by AFM when dimIAPP monomers were incubated at a concentration of 10 µM (SI Figure 3.2C). After kinetic measurements, fibril structures were detected by AFM, whereas IAPP and dimIAPP fibrils could not be distinguished and exhibited the same appearance as the 3 µM IAPP control (Figure 3.2K).

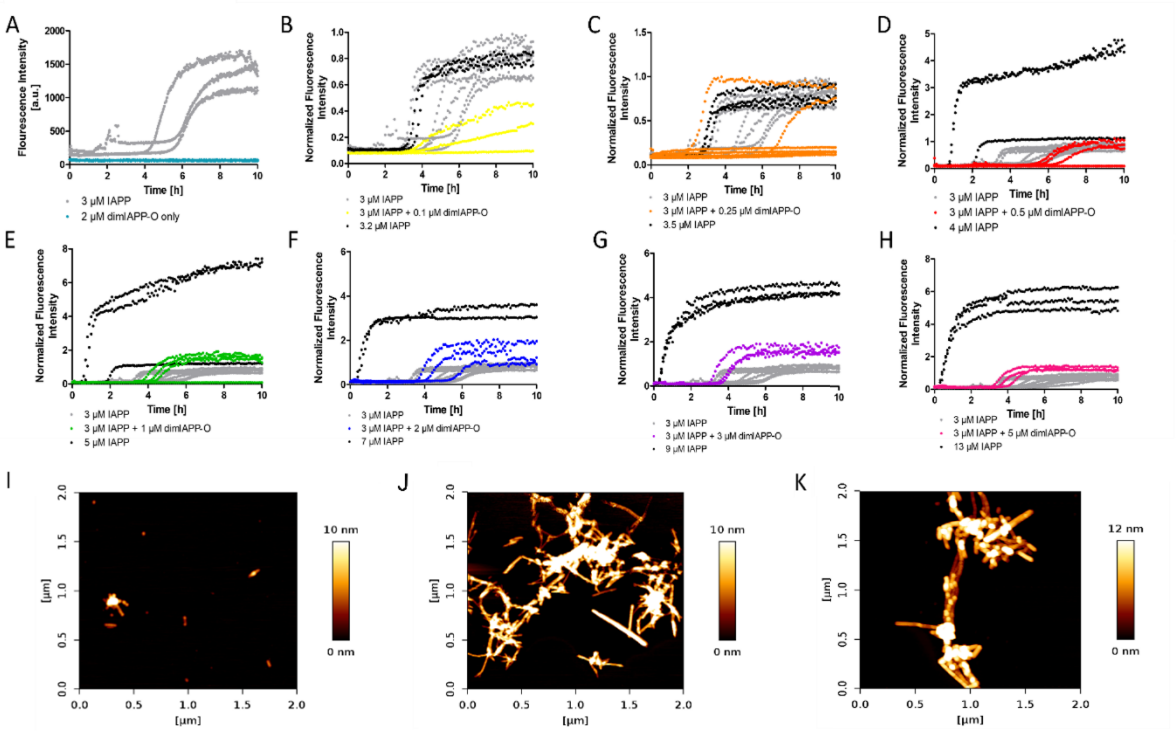

Figure 3.2: Influence of dimIAPP-O in low and high concentrations on IAPP aggregation kinetics. All kinetic assays were performed in 50 mM MES pH 6.5, 25 mM $MgCl_2$ under shaking conditions (300 rpm before each cycle). dimIAPP-O were always prepared in 1 µM and then pooled to 20 µM (AFM image SI figure 2). **A**: Aggregation kinetics of 3 µM IAPP (black) starting from monomeric material in 10 h and aggregation kinetics of 2 µM dimIAPP-O (petrol blue). dimIAPP-O is Thioflavin-T (ThT) negative and does not show any change after 25 h (shown here: 10 h, 25 h: SI figure 2) of kinetic measurement. **B**: 3 µM IAPP (grey), 3 µM IAPP with 0.1 µM dimIAPP-O added before kinetic measurement (yellow) and 3.2 µM IAPP (black). **C**: 3 µM IAPP (grey), 3 µM IAPP with 0.25 µM dimIAPP-O added before kinetic measurement (orange) and 3.5 µM IAPP (black). **D**: 3 µM IAPP (grey), 3 µM IAPP with 0.5 µM dimIAPP-O added before kinetic measurement (red) and 4 µM IAPP (black). **E**: 3 µM IAPP (grey), 3 µM IAPP with 1 µM dimIAPP-O added before kinetic measurement (green) and 5 µM IAPP (black). **F**: 3 µM IAPP (grey), 3 µM IAPP with 0.2 µM dimIAPP-O added before kinetic measurement (blue) and 7 µM IAPP (black). **G**: 3 µM IAPP (grey), 3 µM IAPP with 3 µM dimIAPP-O added before kinetic measurement (purple) and 9 µM IAPP (black). **H**: 3 µM IAPP (grey), 3 µM IAPP with 5 µM dimIAPP-O added before kinetic measurement (pink) and 13 µM IAPP (black). **I**: AFM image of dimIAPP-O alone (A, petrol blue). Colour scale: height in nm. Size of image: 2x2 µm. **J:** AFM image of 3 µM IAPP after aggregation kinetics (black curve). Colour scale: height in nm. Size of the image: 2x2 µm. **K**: AFM image of 3 µM IAPP + 3 µM dimIAPP-O after aggregation kinetics (D, purple). Colour scale: height in nm. Size of image: 2x2 µm.

DimIAPP-O is capable of inhibiting amyloid aggregation of IAPP. DimIAPP-O open the possibility to apply off-pathway oligomers in more complex systems as no additional agent is added to achieve the off-pathway oligomeric state.

3.4.3 Exposure of RIN-m5f cells to dimIAPP-O and IAPP fibrils result in stress response

Next, aim was to gain more insights on how the presence of the different aggregation species, IAPP fibrils or dimIAPP curvilinear oligomers, affects the induction of stress phenotypes in pancreatic RIN-m5f cells. Therefore, the upregulation of transcripts of stress markers associated to ER and mitochondrial oxidative stress was investigated. We were interested exclusively in the effect of externally added IAPP fibrils and dimIAPP-O on stress genes. Therefore, the RIN-m5f cell line, derived from *Rattus norwegicus* was selected as the model cell line because rodent IAPP is aggregation incompetent due to six mutations primarily localized between aa 20 and 29. Contrary, human pancreatic cell lines express aggregation competent IAPP innately. The origin of the observed effect would not have been clearly assigned by the external addition of the species to human pancreatic cells.

Oxidative stress is believed to play a pivotal role in the pathogenesis of T2DM (272, 273). In other diseases connected to the amyloid aggregation of peptides, such as Alzheimer's disease, a higher production of ROS is observed (274). Key oxidative stress markers are superoxide dismutase 2 (Sod2) and catalase (Cat). Sod2 converts two superoxide anion molecules into H_2O_2 while Cat reduces H_2O_2 to water (Figure 3.3A). After exposure to dimIAPP-O, *sod2* expression was significantly upregulated (20-fold) while treatment with IAPP fibrils did not alter the expression level compared to untreated cells. Contrary to that a distinct effect was seen for *cat* expression. Exposure of RIN-m5f to dimIAPP-O resulted in a significant downregulation while exposure to IAPP fibrils resulted in almost 5-fold increased *cat* expression (Figure 3.3B).

When stressed, the cell activates different pathways to rescue itself before apoptosis is initiated. Here, we investigated the influence of dimIAPP-O and IAPP fibrils to four main players involved in ER stress response (Figure 3.3A). Three of them are involved in rescuing mechanisms: Activating transcription factor 6 (Atf6), Pancreatic eukaryotic translation initiation factor 2α kinase (PERK) and Inositol-requiring protein 1 (IRE1) (275). When those transducers are activated, they induce UPR transcription factors X-box binding protein 1 (Xbp1) and activating transcription factor 4 (Atf4) (275). One of the downstream targets of Atf4 is CCAAT-enhancer-binding protein homologous protein (Chop) (276). Chop is key player in apoptosis (277). Here, all tested stress markers for ER stress, namely *atf6* (10-fold)*, xbp1* (4-fold)*, atf4* (6-fold) and *chop* (5-fold) were significantly upregulated after the treatment with IAPP fibrils

while only *chop* was upregulated approximately 3-fold after the treatment with dimIAPP-O (Figure 3.3C).

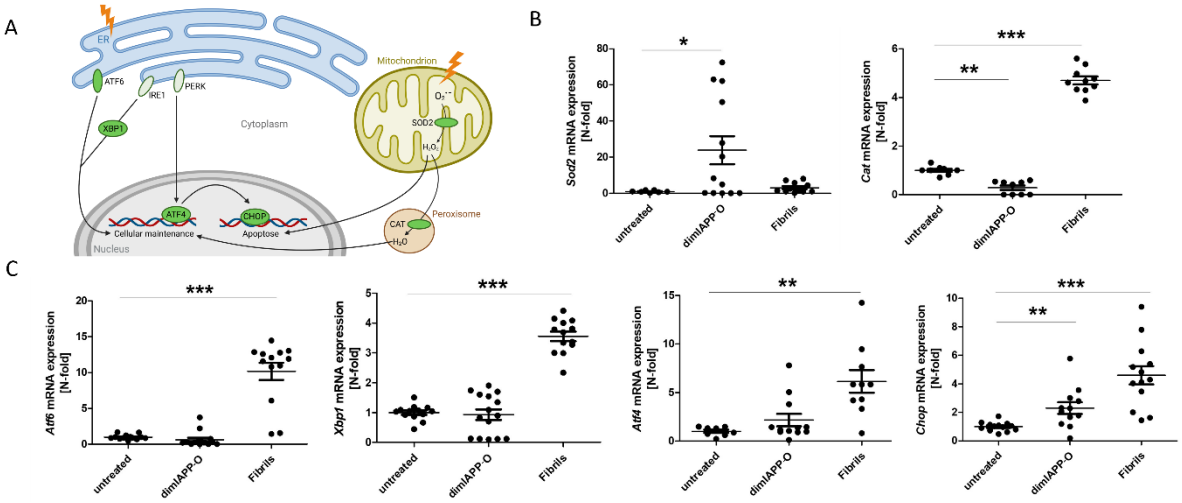

Figure 3.3: Influence of dimIAPP-O and IAPP fibrils on transcription of different ER stress and oxidative stress markers. A: Once the cell is stressed, different stress markers get activated and transcribed more. Activating transcription factor 6 (Atf6) and X box-binding protein 1 (Xbp1) activate mechanism of cell maintenance. Atf4 as a master manipulator controls on the one side adaptive genes of the unfolded protein response (UPR) and on the other hand CCAAT-enhancer-binding protein homologous protein (CHOP) which controls apoptotic UPR genes. Stress also influences transcription of genes involved in oxidative stress response like Superoxide Dismutase 2 (Sod2) and Catalase (Cat). Sod2 reduces superoxide anions to hydrogen peroxide which is then further decomposed into water and gaseous oxygen. Figure inspired by Inagi *et al.* (275). **B**: Influence of dimIAPP-O and IAPP fibrils on the transcription of marker genes for oxidative stress. *Sod2* transcription is significantly increased in cells which were treated with dimIAPP-O while transcription of *cat* is significantly decreased. Cells which were treated with IAPP fibrils exhibit an upregulated transcription of *cat.* **C**: Influence of dimIAPP-O and IAPP fibrils on the transcription of marker genes for ER stress. The transcription rates of RIN-m5f cells were investigated. Both, dimIAPP-O and IAPP fibrils were used in a concentration of 1 µM. Treatment of the cells with IAPP fibrils results in a significant upregulation of ER stress markers *atf6, xbp1, atf4* and *chop. Chop* is also upregulated in cells which were treated with dimIAPP-O. qPCR analysis was performed in 5 technical replicates and 3 biological replicates. Statistical analysis was applied using an unpaired student's t-test and a Grubb's outlier analysis. * = $p < 0.05$, ** = $p < 0.01$.

Another mechanism to react to stress situations is the formation of stress granules (SG) (278) whose formation is triggered by the phosphorylation of the downstream target of PERK and upstream regulator of Atf4: eukaryotic translation initiation factor 2α (eIF2α) (279). Stress granules are condensates composed of untranslated RNA and proteins forming by liquid-liquid phase separation (LLPS) (280-282). The protein class of Ras-GTPase-activating protein (GAP)-binding proteins (G3BP) is the central node of condensate assembly with specificity for unfolded RNA (283) to inhibit RNA-RNA interactions. This supports G3BP to act as an RNA chaperone (284).

We studied liquid-liquid phase separation (LLPS) induced build-up of stress granules by using G3BP1 as a marker protein (Figure 3.4A). We could observe a clustering of G3BP1 in the dimIAPP-O- and IAPP fibril-treated cells while this clustering could not be monitored in the untreated cells (Figure 3.4B, bigger scale: SI Figure 3.4). Both, dimIAPP-O and IAPP fibrils trigger SG formation.

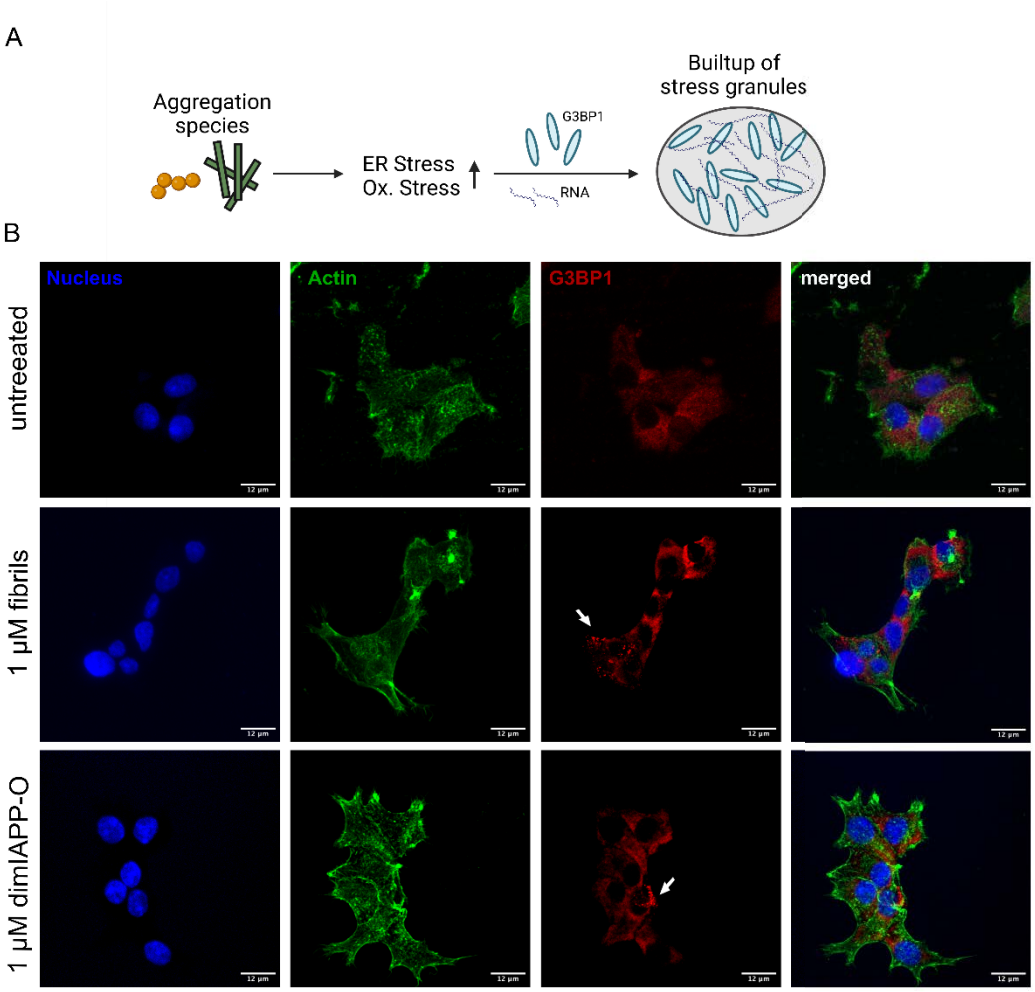

Figure 3.4: Influence of dimIAPP-O and IAPP fibrils on granular stress. A: Using different aggregation species, ER stress and oxidative stress markers get activated and induce the formation of RNA-protein clusters known as stress granules. G3BP1 is one of the proteins involved in this mechanism and is the schematic representation of all proteins involved. **B**: Representative images of RIN-m5f cells treated with 1 µM IAPP fibrils or 1 µM dimIAPP-O (scale bar = 12 µm). G3BP1 is distributed equally in the untreated cells, while it localizes in clusters in the treated cells (white arrows).

3.5 Discussion

We have introduced dimIAPP-O as a stable oligomer model. In this work, we performed initial experiments on the effect of dimIAPP-O on the aggregation of IAPP as well as cell stress mechanisms in comparison to IAPP fibrils. In terms of aggregation, dimIAPP-O acts differently than IAPP monomers by slowing down aggregation of IAPP in sub-stoichiometric ratios. The data suggests dimIAPP-O to interfere with the aggregation mechanism of IAPP by inhibition of nucleation and/or fibrillar growth. Off-pathway oligomeric species are already known to inhibit fibril formation (43, 285-290). This finding is not only known for IAPP, but several other peptides and is explainable by their competition for monomers and the consequence that the number of free monomers available for nucleation processes decreases (257).

In our study setup, we investigated the effect of IAPP fibrils and dimIAPP-O detached from the possibility of internal IAPP to aggregate as we chose murine pancreatic cells. This difference to most other studies as well as the difficult determination of real, stable oligomers in experimental setups might be the reason for the observation that fibrils were more toxic than oligomers. Though Saravanan *et al.* (291) described the existence of non-toxic oligomers we state that our dimIAPP-O model is of great relevance as it still has upregulating effects on *chop* expression. However, the physiological relevance of curvilinear oligomers is elusive (292). We would like to make clear that it is not easy to guarantee the real appearance of the "oligomers" used utilizing human IAPP (258). Understanding the mechanisms behind IAPP oligomer toxicity is crucial for developing targeted therapeutic strategies to prevent or halt the progression of T2DM. It is of great scientific interest to explore ways to inhibit oligomer formation, promote their clearance, or interfere with their interactions with cell membranes triggering UPR, all in an effort to mitigate the toxic effects of IAPP oligomers and potentially improve diabetes management. Huang *et al.* (293, 294) have already shown that the addition of human IAPP to INS-1 rat insulinoma cells also induces the upregulation of ER stress markers on protein level. Similarly, our results indicate IAPP fibrils and dimIAPP-O to be stressful for RIN-m5f cells on transcription level which is in line with Gurlo *et al.* (295). The difference and absolute advantage of our system is the guarantee of the oligomeric species' appearance as no upregulated IAPP is used to trigger stress responses but defined aggregated species. The applicability of an artificial dimeric model in cell culture experiments has also been shown by our group before (264). The reason for the development of LLPS induced SG is not clearly understood but in our study, we could show the addition of external dimIAPP-O and IAPP-fibrils induces LLPS induced SG besides ER stress and oxidative stress responses. Curvilinear oligomers of dimAβ do not show effects of cytotoxicity but altered expression of Alzheimer's related Tau. In agreement with our results, it has been shown that the IAPP aggregate elicits a stress response in cells similar to the cellular responses observed in diabetes mouse experiments (296) confirming the relevance of external added IAPP species to cells to gain complete understanding of T2DM-associated mechanisms.

3.6 Materials & Methods

3.6.1 Protein preparation

DimIAPP expression cassette was purchased by GenScript in the expression vector pET11-a. The expression cassette consists of a 6xHis-tag, the IAPP β-wrapin HI18, a $(G_4S)_3$ flexible linker, another β-wrapin HI18, a $(G_4S)_3$ flexible linker, a TEV cleavage site, the IAPP sequence, a $(G_4S)_4$ flexible linker and again the IAPP sequence. This design is inspired by Mirecka *et al.* (297). *E.coli* BL21(DE3) was transformed by thawing 200 µl of the cells for 10 min on ice, adding 10 ng of the plasmid, letting them rest for 10 min on ice, heat shock at 42 °C for 1 min, letting them rest for 2 min on ice, adding 450 µl of prewarmed to 37 °C 2YT-medium and letting the cells incubate for 1 h at 37 °C under constant agitation of 800 rpm. Afterwards, the cells were plated on LB-agar-Amp-plates and incubated at 37 °C overnight.

A preculture was prepared in a volume of 50 ml. The next day, 2 l of main culture were inoculated with a OD_{600} of 0.1. They were incubated at 37 °C at constant agitation of 120 rpm until OD_{600} of 0.6 was reached. Expression was performed for 3 h at 37 °C 120 rpm. The harvesting was performed for 10 min at 5,000 xg at 4 °C. The bacteria pellet was frozen at -20 °C.

The pellet was dissolved in 10 ml NaPi pH8, 500 mM NaCl, 6 M Urea and 0.4 mM PMSF. The cells were disrupted with a cell disruptor and spun down for 30 min at 40,000 xg at 4 °C.

An IMAC purification was performed in 20 mM NaPi pH8, 500 mM NaCl, 6 M Urea, washed with 20 mM NaPi pH8, 500 mM NaCl, 6 M Urea plus 20 mM imidazole. The elution was performed with 20 mM NaPi pH8, 500 mM NaCl, 6 M Urea plus 450 mM imidazole. The sample was concentrated to 500 µl using a concentrator with 3 MWCO.

SEC was performed using a Superdex200 10/300 Increase column by Cytiva using 20 mM Tris pH8, 50 mM NaCl using NGC liquid chromatography system (Bio-Rad).

TEV cleavage was performed overnight. HPLC run was performed using a gradient over 40 min from 20-64% can, 0.1% TFA. A Zorbax C8 SB300 9.4x250 mm semipreparative column was used.

IAPP (human) was purchased from Pepscan (purity 93.2%) and monomerized by resolving 1 mg which was aliquoted using 1,1,1,3,3,3-hexfluoro-2-propanol (HFIP) in 500 µl 6 M guanidine hydrochloride solution. Subsequently, a SEC was performed using a Supedex75 10/300 Increase column in 10 mM 2-(N-morpholino) ethanesulfonic acid (MES)/NaOH buffer, pH 6 using NGC liquid chromatography system (Bio-Rad) collected in Eppendorf Protein LoBind Tubes.

3.6.2 DimIAPP-O preparation

DimIAPP was aliquoted in 1 µg aliquots using HFIP. DimIAPP was dissolved in 4 µl 50 mM NaOH. Then, 92 µl 50 mM MES pH 6.5, 50 mM NaCl were added. Afterwards, 4 µl 50 mM HCl were added. The dissolved protein was incubated at 37 °C for 16 h quiescently.

DimIAPP-O were spun down at 11,000 xg for 10 min at 20 °C and the buffer was discarded. The oligomers were dissolved in buffer at a concentration of 20 µM. For all applications, oligomers were diluted to the desired concentration. The centrifugation process did not alter the appearance of the oligomers (SI figure 3A).

For cell culture experiments, the oligomers were dissolved in RPMI medium. IAPP fibrils cannot be spun down, therefore they were added to the medium in the buffer in which they were initially prepared.

3.6.3 IAPP fibril preparation

IAPP was dissolved in 50 mM MES pH 6.5, 50 mM NaCl in a concentration of 100 µM in 50 mM MES pH 6.5, 50 mM NaCl and incubated under constant agitation at 800 rpm for 5 days.

3.6.4 ThT fluorescence assays

Aggregation kinetics were monitored by ThT fluorescence. Freshly SEC prepared monomerized IAPP was taken. The *de novo* assays were run in 50 mM MES pH 6.5, 25 mM $MgCl_2$ supplemented with 0.04% NaN_3 and 20 µM ThT in 96-well Half Area Black/Clear Flat Bottom Polystyrene NBS Microplate, 3881, Corning. Respective concentrations of dimIAPP-O were added to the samples. ThT measurements were recorded in a BMG FLUOstar Omega microplate reader with Reader Control software from BMG at 37 °C using excitation wavelengths of 448-10 nm and emission wavelengths of 482-10 nm. Each data point reflects to the average of orbitally measured value over 3 mm with 20 flashes per well. The plate was shaken at 300 rpm before each cycle. The observed effects are not caused by the addition of dimIAPP-O buffer (SI Figure 3D).

Each data point was normalized to the highest value of the control sample (3 µM IAPP only) run in the same measurement to equalise differences due to different gain settings.

3.6.5 AFM imaging

For the AFM imaging of different species after preparation, 10 µl were put onto a freshly cleaned muscovite mica surface and dried by incubating for 2 min. Subsequently, the mica was washed 3 times with Milli-Q H_2O and blown dry with a steam of N_2. The imaging mode

was intermittent contact mode (AC mode) using a JPK NanoWizard 3 AFM run with NanoWizard Control Software v.5 version 5.0.84 by JPK. The cantilever had a silicon tip (OMCL-AC160TS-R3, Olympus) with a tip radius of 9 ± 2 nm, a force constant of 26 N/m and a resonance frequency of 300 kHz. For each sample, an area of 25 μm^2 was scanned to get an overview. For the AFM imaging after ThT kinetics, the plates (96-well Half Area Black/Clear Flat Bottom Polystyrene NBS Microplate, 3881, Corning) were put into a sonication bath for 10 s. Subsequently, 10 µl of the samples were taken out of the plate and prepared like described above.

3.6.6 Cultivation of RIN-m5f cells

RIN-m5F cells (ATCC, CRL-11605, Manassas, VA, USA) were cultured in RPMI-1640 medium (Thermo Fisher ATCC modification, Germany) supplemented with 10% fetal calf serum (Sigma, F9665) and 1% penicillin/streptomycin (ThermoFisher, 15140122) in T75 tissue culture flasks (Sarstedt, 83.3911.002) in a humidified incubator with 5% CO_2 at 37 °C. Depending on their confluence, cells were passaged every three to five days.

For the experiments, cells were seeded in well plates (Sarstedt, Cell+ treated). When 80-90% confluence was achieved, cells were treated with 1 µM IAPP (the same amount of buffer) or 1 µM dimIAPP for 24h at 37°C. For RNA isolation, cells were incubated with trypsin for 10 min at 37 °C and then harvested by centrifugation at 5,000 rpm for 5 min. After counting the cells using Neubauer chamber, the cells were dissolved in TRIzol™ normalized to the same number of cells.

3.6.7 RNA isolation and cDNA synthesis

RNA was isolated TRIzol™ reagent by Thermo Fisher. Subsequently, RNA was adjusted in all groups and reverse transcriped to cDNA by using SuperScript™ III Reverse Transcriptase Kit by Thermo Fisher.

3.6.8 qPCR and evaluation

qPCR was performed using Luna Universal qPCR Master Mix from New England Biolabs. The 2x master mix was mixed with 0.25 µM forward and reverse primer (primer sequences are shown in Table 3.1) and measured at qTOWER^3 by Analytik Jena.

Table 3.1: Primers used for qPCR.

Name of primer	Sequence of primer (5' → 3')
Actb fwd	ACCGAGCATGGCTACAGCGTCACC
Actb rev	GTGGCCATCTCTTGCTCGGAGTCT
Atf4 fwd	AAGGCAGATTCTCTCGCCAA
Atf4 rev	TTCTTCCCCCTTGCCTTACG
Atf6 fwd	CGAGGGAGAGGTGTCTGTTTC
Atf6 rev	GTCTTCACCTGGTCCATGAGG
Cat fwd	CAGGGATGCCATGTTG
Cat rev	GGCTATGGATAAAGGATGGAAA
Cbp fwd	GGTGGCAGTGTCCTG
Cbp rev	CTTCTGAGTCCACGTACTG
Chop fwd	AGGAGAGAAACCGGTCCAA
Chop rev	GGACACTGTCTCAAAGGCGA
Gapdh fwd	CACTGAGCATCTCCCTCACAA
Gapdh rev	TGGTATTCGAGAAGGGAGG
Sod2 fwd	AGGGCCTGTCCCATGATGTC
Sod2 rev	AGAAACCCGTTTGCCTCTACTGAA
Xbp1 fwd	CCACTTGGTACAGACCACTCC
Xbp1 rev	AGACACTAATCAGCTGGGGG

For this study we decided to present the results as N-fold expression changes and not by using ΔΔCt-method as it was not possible to us to find suitable, expression-stable housekeepers (SI figure 3.3C).

3.6.9 Cell viability assay

Cell viability was verified using Cell Titer Blue® assay (Promega, G8080) in a 48 well plate (Sarstedt, 83.3923.300) (SI Figure 3.3A). Cells were treated with 1 µM IAPP fibrils or 1 µM dimIAPP-O. Different puromycin concentration served as negative controls. After an additional incubation time of 24 h at 37 °C, the supernatant was decarded and 100 µl OptiMEM was added. Then, 25 µl of the CellTiter-Blue® reagent was added to each well, followed by a four-

hour incubation at 37 °C. Afterwards, 50 µl supernatant was transferred in a half area 96 well plate (Corning, 3881). The fluorescence was measured at 535/590 nm using a plate reader (Caraustar, BMG LABTECH, Ortenberg, Germany). Results are represented as the percentage of CTB reduction, assuming that the absorbance of positive control was 100%.

3.6.10 Immunocytochemistry

For confocal imaging, the cells were seeded on coverslips. Four coverslips were transferred into one well of a 6-well plate (Sarstedt, 83.3920.300). The plates with the coverslips were left under the UV-lamp for 30 min. Each well containing the coverslips was washed five times with 500 µl of PBS. 500 µl of Poly-D-lysin was added and the coverslips were incubated for 1 h at 37 °C. After the incubation, Poly-D-lysin was discarded and the coverslips were washed five times with 500 µl PBS. Then the cells were seeded on the coverslips.

After the treatment, the medium was discarded and the wells were washed 6 times with 1 ml of PBS. 350 µl of 4% PFA was added, followed by an incubation of 20 min at RT. 4% PFA was discarded and the wells were washed eight times with 1 ml of PBS. Subsequently, the wells were then filled with 1.5 ml of PBS and the plates were stored at 4 °C until immunocytochemistry was performed.

The coverslips containing the cells were removed from the wells. They were incubated with solution 1 (Table 3.2) for 2 min at room temperature. The cells were blocked at room temperature for 1 h by pipetting 100 µl solution 3 (Table 3.2) on the coverslips. This was followed by a further incubation step with the primary antibody Rabbit-anti-G3BP1 (ThermoFisher, PA5-29455) for 1 h at room temperature. The primary antibody was diluted 1:200 in in solution 4 (Table 3.2). Afterwards, the coverslips were washed three times with solution 2 (Table 3.2). At room temperature, the secondary antibodies 647-Goat-anti-Rabbit conjugated with Alexa Fluor™ 647 (ThermoFischer, A-21245) and Alexa Fluor™ Plus 555 Phalloidin (ThermoFisher, A30106), diluted 1:500 in solution 4 (Table 3.2) were incubated for 1 h in the dark. Afterwards, the cells were washed six times with solution 2 (Table 3.2) and the cells were incubated with 300 µM DAPI for 5 min at room temperature. The cells were washed four times with solution 2 (Table 3.2) and then twice with PBS. The coverslips were then shortly dipped in MQ-H_2O and glued onto microscopic slides using Immu-Mount. Confocal microscopy was performed on a Leica AF6000LX inverted microscope equipped with a Hamamatsu C9100-02-LNK00 EM CCD camera. For the excitation of 647 nm, 555 nm and DAPI, a 405 nm laser diode was used, and the fluorescent light was filtered with a 450/50 bandpass filter, respectively. Afterwards, the images were processed with the software Fiji to add a scale bar.

Table 3.2: Solutions for the preparation of immunocytochemically stained RIN-m5f cells.

Solution	Chemicals
1	40 ml PBS + 100 µl TritonX-100
2	20 ml solution 1 + 20 ml PBS
3	10 ml solution 2 + 0.25 g BSA
4	5 ml solution 3 + 5 ml PBS

A false-positive result caused by unspecific binding of the secondary antibody was excluded (SI Figure 3.4).

3.7 Supplementary Information

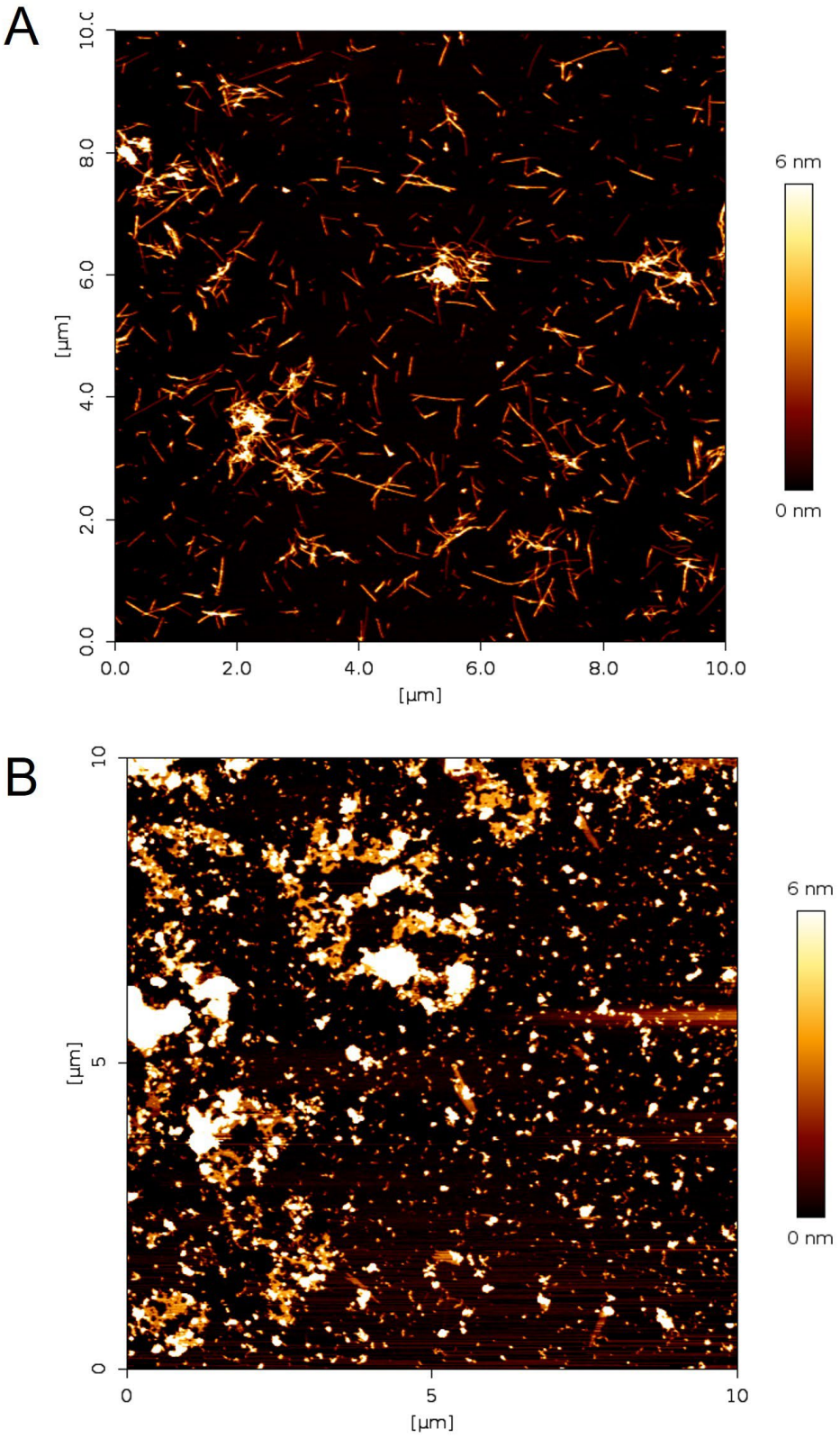

SI Figure 3.1: AFM images of IAPP fibrils (A) and dimIAPP-O (B) after 16 h of quiescent incubation at 37 °C. Colour scale: height in nm, size of images: 10x10 µm.

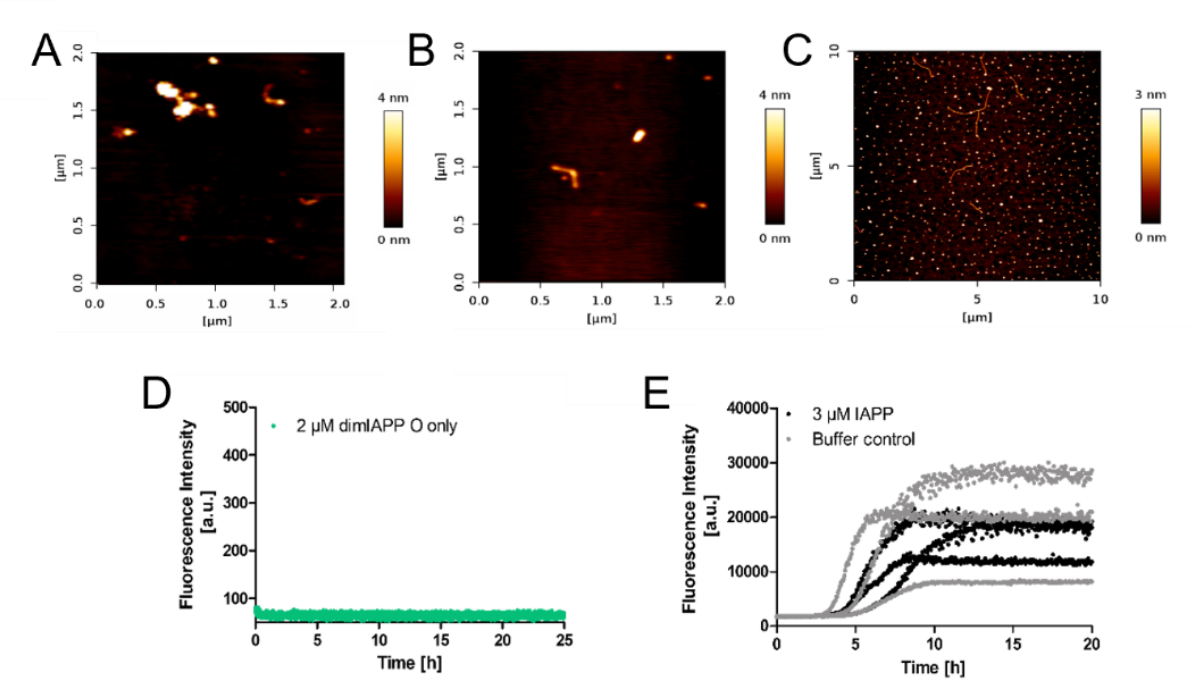

SI Figure 3.2: *In vitro* data on dimIAPP-O. A: dimIAPP-O were formed at a concentration of 1 µM under quiescent conditions for 16 h at 37 °C. After formation, they were centrifuged for 10 min at 11,000 xg and all the buffer but 5 µl were removed. Then, each 5 µl were pooled and sonicated in an ultrasonic water bath for 5 s. In the AFM image there was observed the appearance of dimIAPP-O after the centrifugation step. The appearance of the oligomers did not changed. Colour scale: height in nm. Size of image: 2x2 µm. **B:** AFM image of a completely inhibited aggregation of 3 µM IAPP. No fibrils, but oligomeric species were observed. Colour scale: height in nm. Size of image: 2x2 µm. **C:** dimIAPP-O prepared at a concentration of 10 µM in 50 mM MES pH 6.5, 50 mM NaCl. Under this condition, fibril formation is possible. **D:** 2 µM of dimIAPP-O only after 25 h of kinetic measurement. No increase of ThT fluorescence is observed. **E:** Aggregation kinetics of 3 µM IAPP (black) during 20 h and buffer control. The same volume of dimIAPP-O preparation buffer (50 mM MES pH 6.5, 50 mM NaCl) was added as in the condition of 2 µM dimIAPP-O (grey). The buffer has no influence on the aggregation behaviour of IAPP.

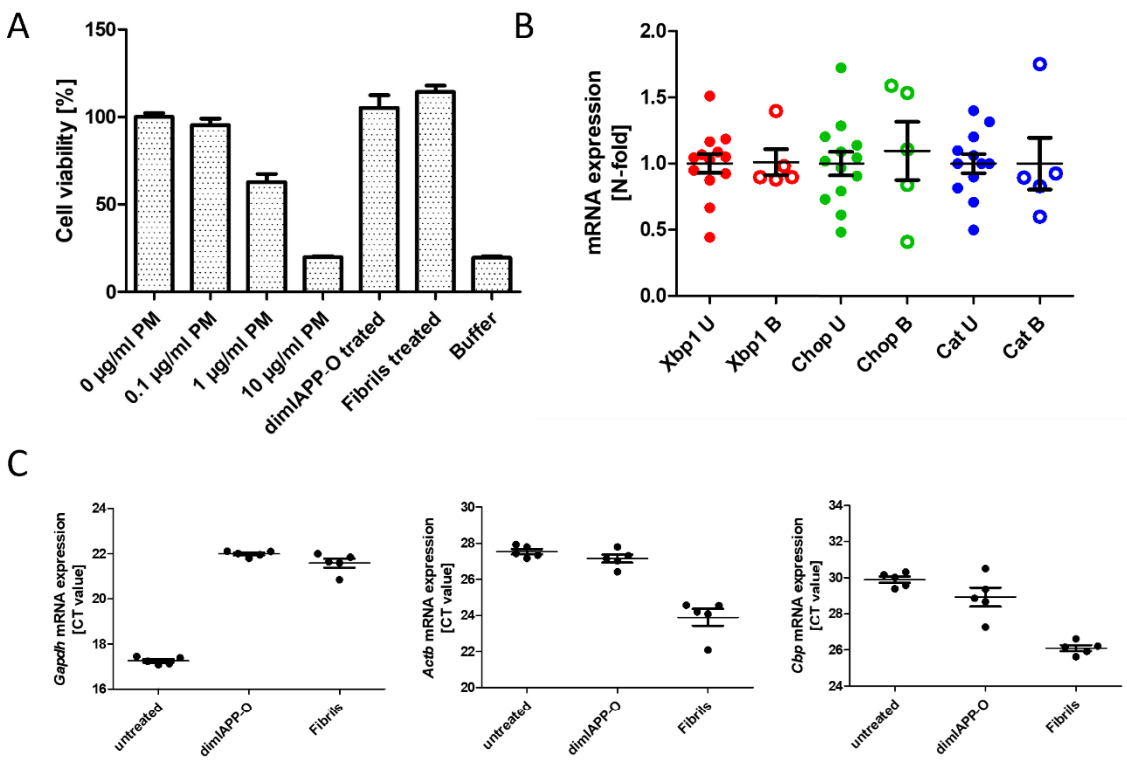

SI Figure 3.3: ***In vivo*** **data on the treatment of RIN-m5f cells with dimIAPP-O and IAPP fibrils. A:** CellTiter-Blue® assay of RIN-m5f cells. Cell viability decreases to 62% when 1 µg/ml puromycin was added and decreases further to 19% when 10 µg/ml puromycin was added. The cell viability of dimIAPP-O and IAPP fibril treated cells did not decrease. **B:** RIN-m5f cells do not show an altered transcription (example: *Xbp1, Chop,* Cat) when the same volume of buffer was added to the cells as for 1 µM of IAPP fibrils. The effect observable in figure 3 is no buffer artefact. U = untreated, B = buffer treated. **C:** No reliable housekeeper genes could be identified. This is the reason for not choosing the ΔΔCt method for evaluation.

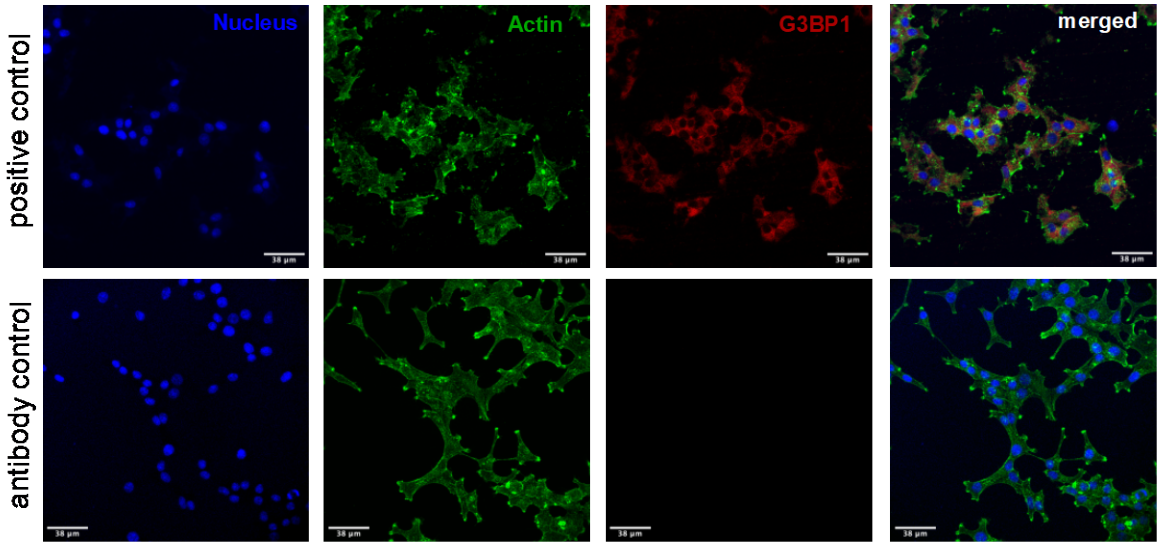

SI Figure 3.4: Representative images of untreated RIN-m5f cells. Cells were treated using DAPI to stain the nucleus (blue) and Phylloidin-555 to stain actin (green). Upper row: For staining G3BP1 the first antibody rabbit-anti-G3BP1 was used to detect G3BP1 and afterwards the second antibody 647-goat-anti-rabbit (red) to stain the first antibody. Lower row: As an antibody control, cells were only treated using the secondary antibody. In this sample no signal was observed for G3BP1, so no false positive signal is detected caused by unspecific binding. Scale bar = 38 µm.

4 PACMAN: A High-Throughput Method for Selecting Proteases with Special Properties

This chapter reflects content of the following publication.

4.1 Publication information

Filip Hasecke*, Anne Pfitzer*, Nadine Teichweyde, Charlotte Esser, Wolfgang Hoyer

*: These authors contributed equally: Filip Hasecke, Anne Pfitzer

To be submitted to Nature Communications

4.2 Abstract

High-throughput screening methods have revolutionized the field of protein engineering, enabling the identification of enzymes with specific functions against challenging substrates in a short period of time. However, balancing constructive screening of large libraries and maintaining general applicability remains a complex challenge. To address this, we introduce a novel selection approach termed "Proteolytic Antigen Cleavage-Mediated AmplificatioN" (PACMAN).

PACMAN utilizes paramagnetic streptavidin-coated microbeads binding biotinylated primers and fluorophore tagged target peptides. In a first step, a DNA library is mixed with the microbeads to enable binding of not exceeding one DNA molecule per microbead. In the second step, the microbeads get saturated with multiple copies of this DNA amplified via polymerase chain reaction in a water-in-oil emulsion (emPCR). After emulsion breakage and recovery of microbeads, DNA is converted into functional proteases in a new emulsion harbouring *in vitro* transcription and translation (IVTT) components. Successful cleavage occurs when the appropriate target peptide is bound to the same microbead as the synthesized protease. Flow cytometry analysis identifies populations of microbeads with successful proteolysis, which are then sorted for subsequent screening rounds. To validate PACMAN, a protease from Tobacco-Etch Virus (TEV) and its target were utilized as a proof of concept. The coupling of 10^6 target peptide molecules per microbead provided a suitable resolution between control and cleaved populations. Furthermore, precise size distribution of the emulsions' compartments ensured effective genotype-phenotype coupling with only one microbead per droplet.

To demonstrate the efficiency of PACMAN, an input DNA sample was subjected to multiple selection cycles. In the second round, strongly diluted input achieved even higher enrichments showcasing the power of this method for efficient protein selection.
In conclusion, PACMAN presents a user-friendly and high-throughput screening tool for selecting proteases against specific targets. Its ability to handle large libraries, achieve significant enrichment, and identify functional enzymes makes it an asset for protein engineering and diverse scientific applications. PACMAN represents a promising advancement in the field of high-throughput screening, unlocking new possibilities for accelerating protein discovery and optimization.

4.3 Introduction

The demand for effective and easy to apply screening and selection methods is very high. Reconciling constructive screening of large libraries and general applicability is a challenge and has occupied the scientific community for decades. There are several high throughput screening methods, rather conventional and more sophisticated ones. There are several methods utilizing fluorescence activated cell sorting (FACS), like entrapment of a fluorescent product in the cell (298). Another possibility are cell surface display methods of which there are now many. In 1985, Smith introduced phage display to select antibodies against specific targets (299). Phage display is widely used, e.g. in the selection of antibodies for clinical purposes (300). Rapidly, phage display was complemented by bacterial display (301, 302) and yeast display (303). Mimicking cells is possible by *in vitro* compartmentalization (IVC) allowing to circumvent transformation efficiency and host cell regulatory and metabolic interactions with the desired reaction. In the early 1990s, the idea of “one-bead-one-compound” emerged and beads of diameters of 100-200 µm were coupled to multiple copies of individual peptide sequences by the split-and-pool method (304). With this method, target specific binding of antibodies (304) and binding motifs for streptavidin (304), e.g., could be identified. Beads are excellent delivery vehicles because of their ability to harbour multiple copies (305), not only of peptides, but also of genes (306).

Implementing beads in cell-like compartments touches the field of microfluidics which is used to produce droplets of a certain size (303, 307). Since 2014, encapsulating beads in droplets is possible with the help of a “suspension hopper” which tackles the issue of settling of the beads. With this method, it is possible to introduce 176,000 beads within 5.5 h. The method is precise in terms of size distribution of droplets, but slow which justifies still using bulk emulsification where 10^7 to 10^{11} compartments can be generated in 10 min (308) for selective applications of larger libraries (309).

Here, we introduce a novel IVC on-bead method, called “Proteolytic Antigen Cleavage-Mediated AmplificatioN” (PACMAN), to select proteins with proteolytic activity against certain targets (Figure 4.1). Starting point of the method are paramagnetic streptavidin-coated microbeads. They are decorated with biotinylated primers as well as a biotinylated target peptide N’- and C’-terminally tagged with two different fluorophores, here 5-FAM (green) and Cy5 (red) as shown in Figure 4.1, step 1. The next step is the emulsification in a water-in-oil emulsion with an oil phase consisting of fluorinated oil and an aqueous phase harbouring the decorated microbeads, the DNA library and polymerase chain reaction (PCR) solution (Figure 4.1, step 2). An emulsion PCR (emPCR) is performed to amplify the DNA variants monoclonally within a distinct droplet and let them bind to the microbeads. After breakage of the emulsion and recovery of the microbeads including extensive washing steps (Figure 4.1, step 3), a new water-in-oil emulsion is prepared with an oil phase based on mineral oil and ABIL® EM 90 and an aqueous phase harbouring the microbeads and all components for *in vitro* transcription and translation (IVTT) (Figure 4.1, step 4). During the incubation of the emulsion, the DNA bound to the microbeads is transcribed and translated to functional proteolytically active protein and in case the target bound to the same bead withing the distinct droplet, the protease variant cleaves its target (Figure 4.1, step 5). After breakage of the emulsion and extensive washing (Figure 4.1, step 6), FACS is performed and the altered ratio of green to red fluorescence compared to a non-cleaved sample determines microbeads populations of successful digestion and those of unsuccessful digestions. Successful populations are sorted (Figure 4.1, step 7), the DNA reamplified (Figure 4.1, Step 8) and the next PACMAN round is ready to start (Figure 4.1, step 2).

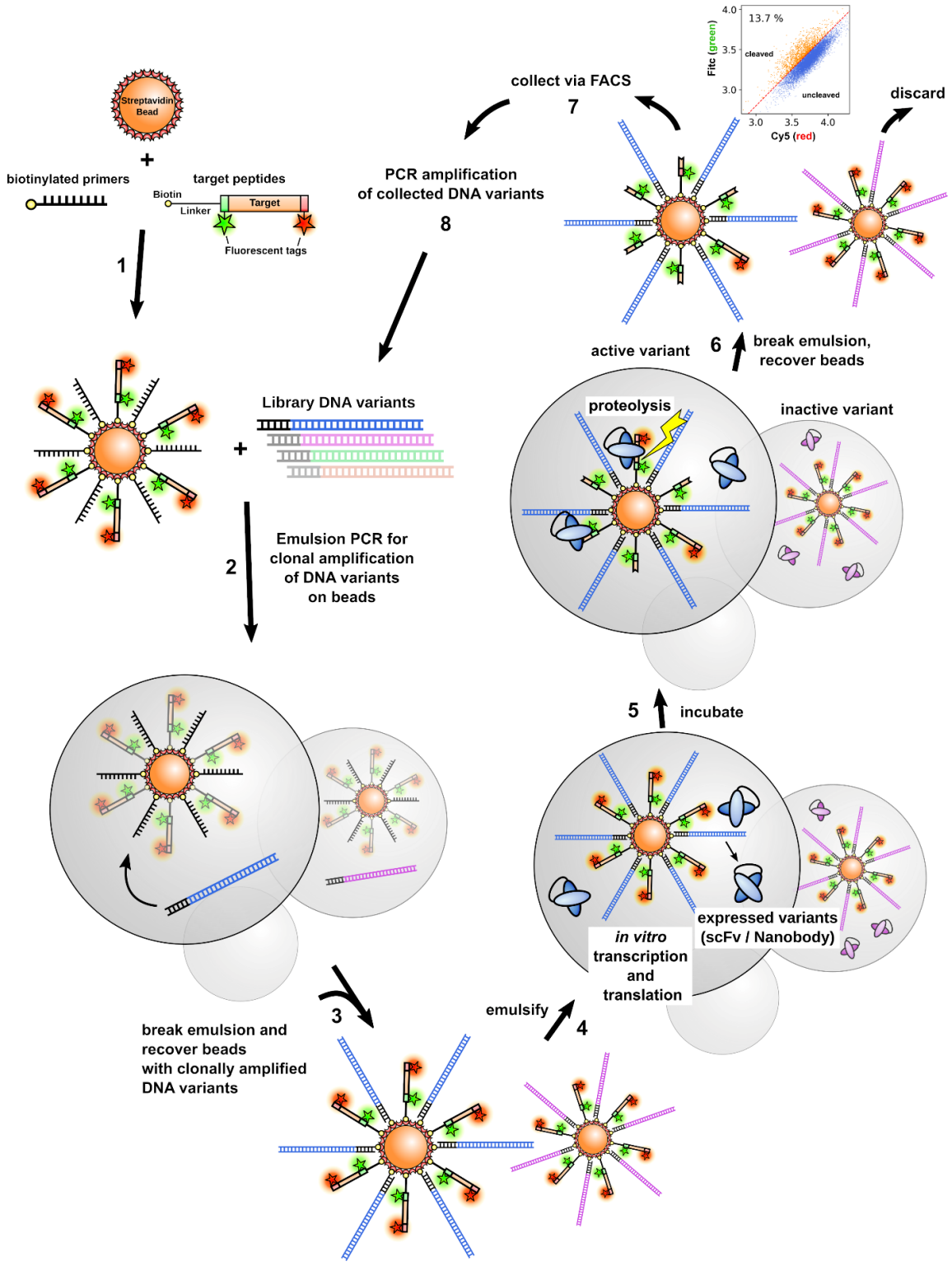

Figure 4.1: PACMAN scheme. The principle of PACMAN illustrated. **1:** The paramagnetic streptavidin-coated microbeads are decorated with biotinylated primers and target peptides N'- and C'-terminally tagged with two different fluorophores, here 5-FAM (green) and Cy5 (red). **2:** An emulsion is prepared using a fluorinated oil phase and an aqueous phase harbouring the decorated microbeads, the DNA library, and the PCR solution. After monoclonal amplification of the DNA library, the emulsion is broken **(3)** and extensively washed. **4:** A new emulsion utilizing mineral oil and ABIL® EM 90 as the oil phase and an IVTT system as the aqueous phase harbouring the microbeads and the IVTT solution. **5:** During incubation, proteolytically active proteins are synthesized and in case the target within the distinct droplet is suitable, the cleavage reaction takes place. **6:** After breaking the emulsion and extensive washing, FACS **(7)** is performed and the population with the altered green to red ratio collected. **8:** After reamplification of the collected DNA variants, the next PACMAN round is ready to start from step 2.

Here, we utilized a protease from Tobacco-Etch Virus (TEV) and its target as an example for the proof of concept of our novel selection method. Our method does not require sophisticated equipment and is therefore easy to use.

4.4 Results

4.4.1 Coupling of TEV target to streptavidin coated microbeads and cleavage reaction monitoring

Selection methods which are easy to apply are crucial for a broad application. The proof of concept of PACMAN was achieved by utilizing a protease from TEV and its target (Figure 4.1A). The target (Figure 1A) was N'- and C'-terminally tagged with two different fluorophores, namely N'-terminally 5-FAM and C'-terminally Cy5. Additionally, a molecule of biotin was coupled N'-terminally to the TEV-target peptide. Via this biotin molecule, the target was coupled to a paramagnetic streptavidin-coated microbead with a diameter of 3 µm. The coupling was performed with different amounts of the target peptide: 10^5, 10^6 and 10^7 peptides per microbead. The coupled microbeads were incubated over night with added purified TEV-protease. The success of cleavage was analysed via flow cytometry (Figure 4.2B). Empty, non-coupled microbeads are shown in grey, microbeads harbouring the target peptide in blue shades and microbeads harbouring the target peptide after incubation with TEV protease in orange shades. As shown in Figure 4.2B, the TEV-peptide was coupled to the microbeads successfully. The fluorescence intensity was increased with increased number of molecules per microbead. Successful cleavage was detected by a decreased intensity of Cy5 signal and a simultaneous increase in 5-FAM signal. The increase in 5-FAM signal is explainable by the loss of its Förster resonance energy transfer (FRET) partner Cy5 as 5-FAM and Cy5 are known to be FRET partners (310). From the data monitored in Figure 4.2B, we decided to couple 10^6 molecules of target peptide per microbead as the resolution between control (blue) and cleaved (orange) population was sufficient. The IVTT emulsions based on mineral oil and ABIL® EM 90 (image taken via Total Internal Reflection Fluorescence (TIRF) microscopy, Figure 4.2C) were prepared and analysed concerning their diameter (Figure 4.2D). The analysis revealed that most of the droplets exhibit a diameter of around 20 µm, resulting in an average volume of 1.1 - 1.5 pl, leading to the assumption of 1.2 - 1.6x10^7 compartments in each IVC sample consisting of 550 µl volume. This estimation is important for the screening applicability of the emulsion for the desired library. The chosen condition had the advantage of compartmentalizing the majority of microbeads separately, meaning only one microbead per droplet (Figure 4.2E). This is another crucial point as genotype-phenotype coupling was only possible under this condition. In case, the majority of microbeads would not be separated, the screening would be extended drastically.

The analysis of flow cytometry data was facilitated by adding a population boundary (Figure 4.2F, red dashed line). In the lower area, microbead events exhibiting a high Cy5 fluorescence signal are shown in blue while microbeads exhibiting a lower Cy5 but increased 5-FAM fluorescence are shown in the area above in orange. This means, the blue population represents the non-cleaved targets and the orange microbeads the cleaved targets. Only one copy of TEV protease encoding DNA coupled to one microbead did not give sufficient results in terms of cleavage success caused by low expression rates (Figure 4.2F). This was found by coupling one copy of TEV protease encoding DNA to the microbeads and mixing these microbeads in a ratio of 1:10 with microbeads without DNA. When the microbeads were emulsified, 2.9% of the microbeads were found in the orange population, meaning the cleaved population, and could be distinguished from the control population. In contrast, when 1000 molecules of TEV protease encoding DNA were added to the microbeads, the “IVTT only”-sample showed a shift towards the population boundary but could not be distinguished at all from the control sample. When IVC was applied, 15.6% of the microbeads appeared in the upper area, so the cleaved population. Interestingly, 5.6% more than expected could be observed in this area which is explainable by the fact that a small part of the droplets of the emulsion harboured more than one microbead (Figure 4.2E).

Because of the genotype-phenotype-dependent setup of PACMAN, it is not possible to add more than one molecule per microbead by adding higher concentrations of DNA to the aqueous phase. This issue led us to optimize of the technique of on-bead emPCR where a copy of a DNA is amplified in a compartment monoclonally.

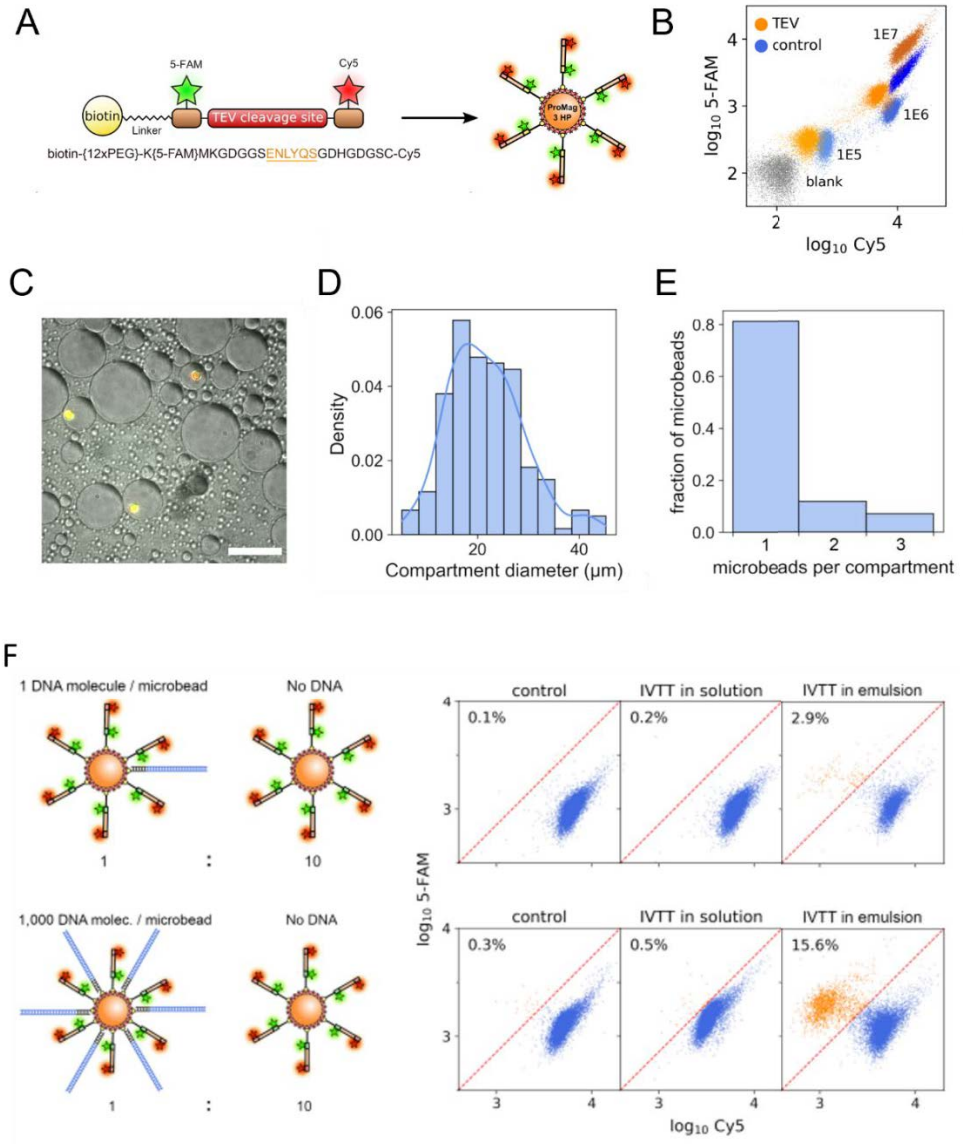

Figure 4.2: Pre-experiments to PACMAN. A: The starting material is a paramagnetic ProMag 3HP microbead. Due to its streptavidin surface, it is capable of binding biotinylated compounds. Therefore, the double fluorophore (5-FAM, Cy5) labelled TEV target was biotinylated and attached to the microbeads. **B:** Analysis on the amount of target peptides bound to the microbeads are reasonable in terms of screening sufficiency. 10^5, 10^6 and 10^7 target peptides per microbead were tested. Grey: blank microbeads, blue: microbeads with bound TEV target not incubated with TEV protease. Orange: microbeads with bound TEV target incubated with TEV protease and therefore shifted to less Cy5/more 5-FAM signal. **C:** TIRF image of mineral oil and ABIL® EM 90 based/IVTT emulsion with encapsulated target bound microbeads. Scalebar: 25 µm. **D:** Histogram analysis of the compartment diameter of microbead harbouring compartments. N = 181. **E:** Histogram of fraction of microbeads harbouring 1, 2 or 3 microbeads per compartment. N = 76. **F:** Scheme to visualize the input material and flow cytometry data. DNA and target peptide bound microbeads were used in a ratio of 1:10 to only DNA bound microbeads. A control sample, a sample incubated in IVTT solution without emulsion and an emulsified sample are shown. The red dashed line simplifies the visualisation of successful cleavage reaction. Non-cleaved population: blue, cleaved population: orange. Percentage of cleaved material is given in the plots.

4.4.2 Proof of Principle

To provide the proof of principle of the PACMAN method, two populations of microbeads were recovered from the emulsions and analysed via flow cytometry. These microbead populations were a) microbeads harbouring DNA encoding for TEV protease and b) microbeads harbouring DNA encoding for a random DNA exhibiting approximately the same number of nucleotides termed $scFv_{nc}$. To obtain information on the success of enrichments via PACMAN visualized in flow cytometry, PACMAN was performed using microbeads' mixtures of 1:1, 1:10, 1:100 and 1:1000 of TEV protease encoding DNA and $scFv_{nc}$ encoding DNA (Figure 4.3). As expected, the percentage of cleavage success (orange population above the red dashed line) correlated with the ratio of TEV protease encoding input DNA, illustrated best in 1:1 ratio where 53.2% of all analysed microbeads were in the area of cleaved microbeads and 1:1000 ratio where 0.5% of all analysed microbeads were in the mentioned area.

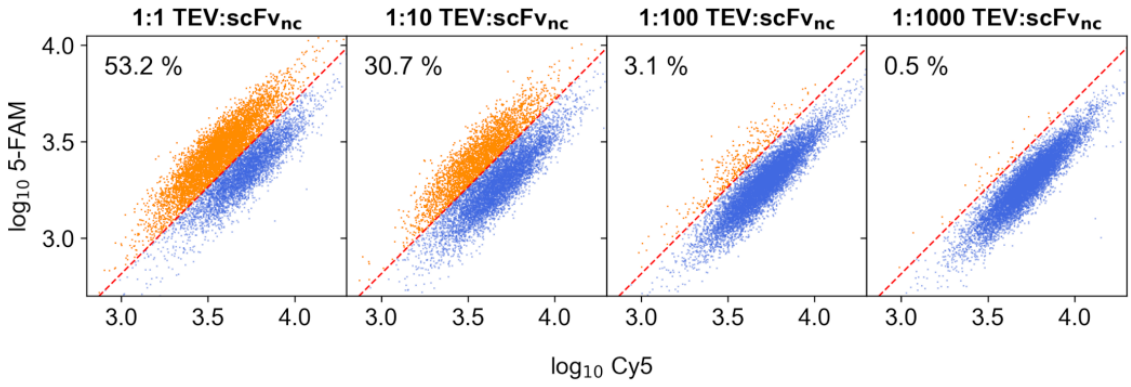

Figure 4.3: Correlation of cleavage success and input DNA. Four different mixtures of TEV protease encoding DNA and $scFv_{nc}$ encoding DNA microbeads were prepared and emulsified. PACMAN was performed, recovered, and analysed via flow cytometry. In a ratio of 1:1, 53.2% of microbeads were found in the cleavage-positive area above the red dashed line and in a ratio of 1:1000, 0.5% of the analysed microbeads were found in the cleavage-positive area.

Finally, the proof of concept was verified by sequential enrichment of TEV protease encoding DNA via PACMAN from a strongly diluted input DNA sample. The 1:1000 TEV: $scFv_{nc}$ sample was used and 1,000 microbeads detected in the cleavage-positive area, so the area above the red dashed line, were sorted. Afterwards, the TEV protease was reamplified from the microbeads using PCR. For the evaluation of the enrichment, the DNA was cloned into a plasmid fulfilling the requirements for further steps, termed pIgV (see 4.6.1) and *E. coli* XL1-Blue Competent Cells were transformed. Colony PCR was applied using gene specific primers to determine the ratio of TEV protease encoding to $scFv_{nc}$ encoding DNA (Figure 4.4). After the first PACMAN selection cycle, the initial ratio of TEV protease encoding DNA to $scFv_{nc}$ encoding DNA was accumulated from 1:1000 to 1:3 as shown in the first column of Figure 4.4. This means a 333-fold enrichment of TEV protease encoding DNA in the selected area compared to the input. The second PACMAN round was performed twice with different

amounts of input DNA served as input in emPCR: in the conventional second cycle of PACMAN, $4x10^6$ molecules of input DNA were inserted while in the “less input”-cycle 2 only $1x10^6$ molecules were used. This was done to observe the possibility of increasing the selection specificity and hence enhancing the cumulative enrichment of TEV protease encoding DNA. A surprisingly high enrichment of 3,800-fold was observed in the conventional second cycle of PACMAN. Even more successful was the enrichment of the “less input”-cycle 2 of PACMAN where a 98,000-fold enrichment was observed and of 98 colonies none was $scFv_{nc}$ positive.

This experiment clearly demonstrated the proof of principle of PACMAN.

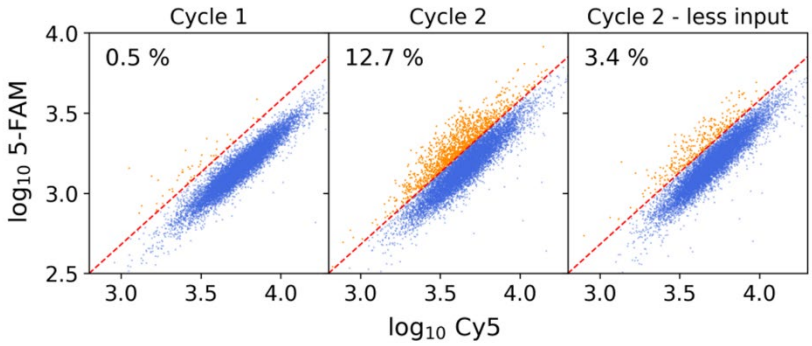

Input DNA DNA molecules per 10^6 beads	$4x10^6$	$4x10^6$	$1x10^6$
Sort gate	0.5%	1.5%	1.1%
Colonie PCR ratio of TEV to $scFv_{nc}$	12 to 36	42 to 11	98 to 0
Cumulative enrichment	333-fold	3,800-fold	98,000-fold

Figure 4.4: Cumulative enrichment of TEV protease encoding DNA after PACMAN cycles. After the first cycle of PACMAN, the cumulative enrichment was 333-fold. When using only a fourth of input DNA in cycle 2, the enrichment was even enhanced to 98,000-fold compared to using the standardized amount of $4x10^6$ molecules of input DNA per bead.

4.5 Conclusion

The introduced PACMAN method offers the possibility to screen for protease activity from DNA libraries effectively. DNA and target peptide presenting microbeads in combination with bulk emulsions containing IVTT solutions are the main characteristics of PACMAN. In this study we could show the power of this new method. During two rounds of PACMAN, irrelevant DNA was completely displaced although used in large excess. Considering TEV protease optimization, PACMAN might be utilized to screen for a TEV protease mutant preferring ENLYFQ|M instead of ENLYFQ|G/S. Besides TEV proteases, PACMAN can be applied to screen for any specific protease activity or even for the discovery of completely new enzymes with proteolytic activity starting from just DNA libraries.

4.6 Material & Methods

4.6.1 Plasmids

The plasmid used in PACMAN is termed pIgV and derived from the PURExpress® In Vitro Protein Synthesis kit by New England Biolabs. The gene in this plasmid, DHFR, was removed and a new cloning site containing the restriction sites SalI and NotI were introduced. The plasmid map is shown in Figure 4.5.

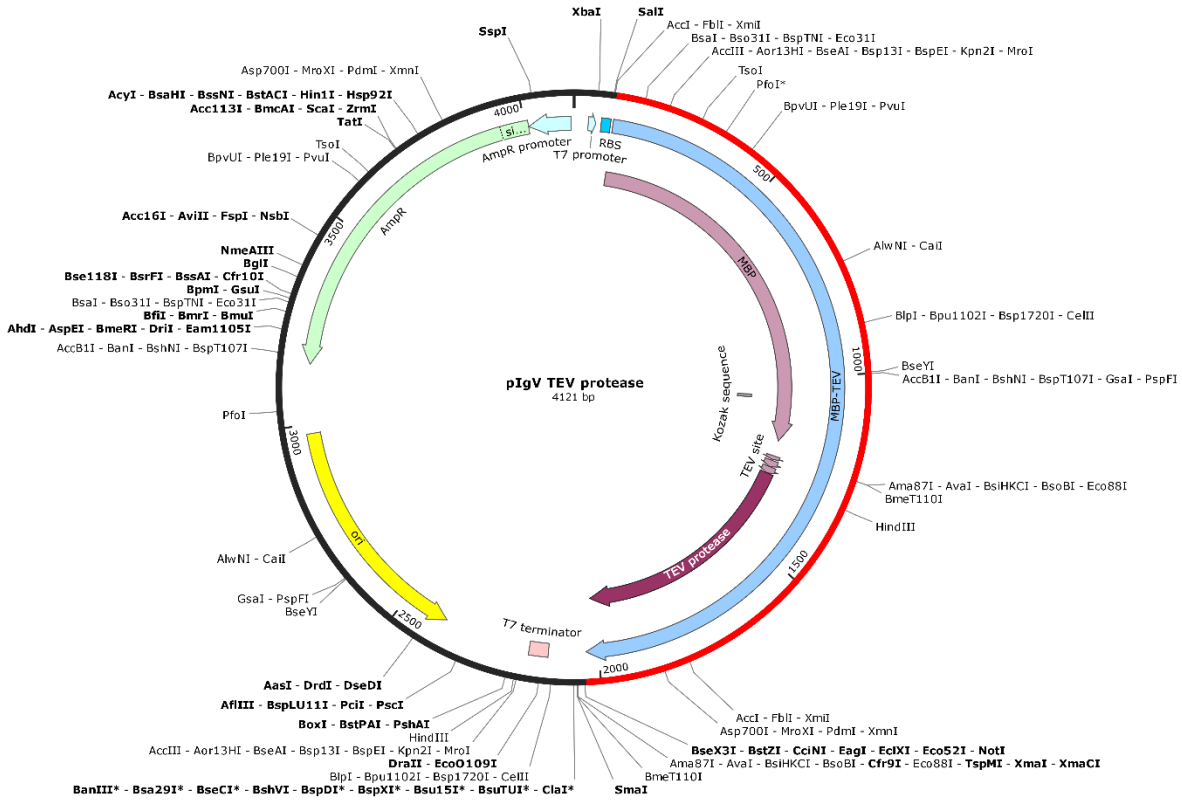

Figure 4.5: Plasmid map of the pIgV TEV protease.

The sequence of the pIgV TEV protease plasmid is shown in the following. The gene encoding for the TEV protease is printed in small letters.

CCCCGAAAAGTGCTAGTGGTGCTAGCCCCGCGAAATTAATACGACTCACTATAGGGTCT
AGAAATAATTTTGTTTAACTTTAAGAAGGAGAGTCGACatgaaaactgaagaaggtaaactggtaatct
ggattaacggcgataaaggctataacggtctcgctgaagtcggtaagaaattcgagaaagataccggaattaaagtcaccgttg
agcatccggataaactggaagagaaattcccacaggttgcggcaactggcgatggccctgacattatcttctgggcacacgacc
gctttggtggctacgctcaatctggcctgttggctgaaatcaccccggacaaagcgttccaggacaagctgtatccgtttacctggg
atgccgtacgttacaacggcaagctgattgcttacccgatcgctgttgaagcgttatcgctgatttataacaaagatctgctgccgaa
cccgccaaaaacctgggaagagatcccggcgctggataaagaactgaaagcgaaaggtaagagcgcgctgatgttcaacct
gcaagaaccgtacttcacctggccgctgattgctgctgacgggggttatgcgttcaagtatgaaaacggcaagtacgacattaaa
gacgtgggcgtggataacgctggcgcgaaagcgggtctgaccttcctggttgacctgattaaaaacaaacacatgaatgcagac
accgattactccatcgcagaagctgcctttaataaaggcgaaacagcgatgaccatcaacggcccgtgggcatggtccaacatc
gacaccagcaaagtgaattatggtgtaacggtactgccgaccttcaagggtcaaccatccaaaccgttcgttggcgtgctgagcg
caggtattaacgccgccagtccgaacaaagagctggcaaaagagttcctcgaaaactatctgctgactgatgaaggtctggaag
cggttaataaagacaaaccgctgggtgccgtagcgctgaagtcttacgaggaagagttggcgaaagatccacgtattgccgcca
ccatggaaaacgcccagaaaggtgaaatcatgccgaacatcccgcagatgtccgctttctggtatgccgtgcgtactgcggtgat
caacgccgccagcggtcgtcagactgtcgatgaagccctgaaagacgcgcagactaattcgagctcgaacaacaacaacaat
aacaataacaacaacctcgggatcgagggaaggggagaaaatctttatttcaaggtcatcatcatcatcatcatggagaaa
gcttgtttaaggggccgcgtgattacaacccgatatcgagcaccatttgtcatttgacgaatgaatctgatgggcacacaacatcgtt

gtatggtattggatttggtcccttcatcattacaaacaagcacttgtttagaagaaataatggaacactgttggtccaatcactacatg
gtgtattcaaggtcaagaacaccacgactttgcaacaacacctcattgatgggagggacatgataattattcgcatgcctaaggat
ttcccaccatttcctcaaaagctgaaatttagagagccacaaagggaagagcgcatatgtcttgtgacaaccaacttccaaacta
agagcatgtctagcatggtgtcagacactagttgcacattcccttcatctgatggcatattctggaagcattggattcaaaccaagga
tgggcagtgtggcagtccattagtatcaactagagatgggttcattgttggtatacactcagcatcgaatttcaccaacacaaacaa
ttatttcacaagcgtgccgaaaaacttcatggaattgttgacaaatcaggaggcgcagcagtgggttagtggttggcgattaaatgc
tgactcagtattgtgggggggccataaagttttcatggtgaaacctgaagagccttttcagccagttaaggaagcgactcaactcat
gaatcgtcgtcgccgtcgctaataaGCGGCCGCGCTAGCGGTCCCGGGGGATCGATCCGGCTGCT
AACAAAGCCCGAAAGGAAGCTGAGTTGGCTGCTGCCACCGCTGAGCAATAACTAGCAT
AACCCCTTGGGGCCTCTAAACGGGTCTTGAGGGGTTTTTTGCTGAAAGGAGGAACTATA
TCCGGAAGCTTGGCACTGGCCGACCGGGGTCGAGCACTGACTCGCTGCGCTCGGTCG
TTCGGCTGCGGCGAGCGGTATCAGCTCACTCAAAGGCGGTAATACGGTTATCCACAGA
ATCAGGGGATAACGCAGGAAAGAACATGTGAGCAAAAGGCCAGCAAAAGGCCAGGAAC
CGTAAAAAGGCCGCGTTGCTGGCGTTTTTCCATAGGCTCCGCCCCCCTGACGAGCATC
ACAAAAATCGACGCTCAAGTCAGAGGTGGCGAAACCCGACAGGACTATAAAGATACCA
GGCGTTTCCCCCTGGAAGCTCCCTCGTGCGCTCTCCTGTTCCGACCCTGCCGCTTACC
GGATACCTGTCCGCCTTTCTCCCTTCGGGAAGCGTGGCGCTTTCTCATAGCTCACGCTG
TAGGTATCTCAGTTCGGTGTAGGTCGTTCGCTCCAAGCTGGGCTGTGTGCACGAACCC
CCCGTTCAGCCCGACCGCTGCGCCTTATCCGGTAACTATCGTCTTGAGTCCAACCCGCT
AAGACACGACTTATCGCCACTGGCAGCAGCCACTGGTAACAGGATTAGCAGAGCGAGG
TATGTAGGCGGTGCTACAGAGTTCTTGAAGTGGTGGCCTAACTACGGCTACACTAGAAG
AACAGTATTTGGTATCTGCGCTCTGCTGAAGCCAGTTACCTTCGGAAAAAGAGTTGGTA
GCTCTTGATCCGGCAAACAAACCATCGCTGGTAGCGGTGGTTTTTTTGTTTGCAAGCAG
CAGATTACGCGCAGAAAAAAAGGATCTCAAGAAGATCCTTTGATCTTTTCTACGGGGTCT
GACGCTCAGTGGAACGAAAACTCACAGATCCGGGATTTTGGTCATGAGATTATCAAAAA
GGATCTTCACCTAGATCCTTTTAAATTAAAAATGAAGTTTTAAATCAATCTAAAGTATATAT
GAGTAAACTTGGTCTGACAGTTACCAATGCTTAATCAGTGAGGCACCTATCTCAGCGAT
CTGTCTATTTCGTTCATCCATAGTTGCCTGACTCCCCGTCGTGTAGATAACTACGATACG
GGAGGGCTTACCATCTGGCCCCAGTGCTGCAATGATACCGCGAGACCCACGCTCACCG
GCTCCAGATTTATCAGCAATAAACCAGCCAGCCGGAAGGGCCGAGCGCAGAAGTGGTC
CTGCAACTTTATCCGCCTCCATCCAGTCTATTAATTGTTGCCGGGAAGCTAGAGTAAGTA
GTTCGCCAGTTAATAGTTTGCGCAACGTTGTTGCCATTGCTACAGGCATCGTGGTGTCA
CGCTCGTCGTTTGGTATGGCTTCATTCAGCTCCGGTTCCCAACGATCAAGGCGAGTTAC
ATGATCCCCCATGTTGTGCAAAAAAGCGGTTAGCTCCTTCGGTCCTCCGATCGTTGTCA
GAAGTAAGTTGGCCGCAGTGTTATCACTCATGGTTATGGCAGCACTGCATAATTCTCTTA
CTGTCATGCCATCCGTAAGATGCTTTTCTGTGACTGGTGAGTACTCAACCAAGTCATTCT
GAGAATAGTGTATGCGGCGACCGAGTTGCTCTTGCCCGGCGTCAATACGGGATAATAC

CGCGCCACATAGCAGAACTTTAAAAGTGCTCATCATTGGAAAACGTTCTTCGGGGCGAA
AACTCTCAAGGATCTTACCGCTGTTGAGATCCAGTTCGATGTAACCCACTCGTGCACCC
AACTGATCTTCAGCATCTTTTACTTTCACCAGCGTTTCTGGGTGAGCAAAAACAGGAAGG
CAAAATGCCGCAAAAAAGGGAATAAGGGCGACACGGAAATGTTGAATACTCATACTCTT
CCTTTTTCAATATTATTGAAGCATTTATCAGGGTTATTGTCTCATGAGCGGATACATATTT
GAATGTATTTAGAAAAATAAACAAATAGGGGTTCCGCGCACATTT

4.6.2 Primers

Table 4.1: Primer sequences

Name of primer	Sequence 5' → 3'
Link-T7 fwd	AAGTGCTAGTGGTGCTAGCC
No-Ext-T7 rev	CAAAAAACCCCTCAAGACCCG
Vector Amplification For	GGTGCAGCAGAGCAGAAA
Vector Amplification Rev	CATGTCGACTCTCCTTCTTAAA
b-TEG-TGS-Link-T7p Fwd	[biotin][TEG]TGTGTGTGTGTGTGTGTGTGTGTGAAGTGCTAGTGGTGCTAGCC

4.6.3 Preparation of input DNA for PACMAN

The input DNA was composed of a 5' untranslated region (UTR), the T7 promotor sequence, a ribosome binding site (RBS), the gene of interest, a 3' UTR and a T7 terminator sequence (Figure 4.6). The input DNA was prepared using two primers (Figure 4.6, termed Link-T7-fwd and No-Ext-T7-rev).

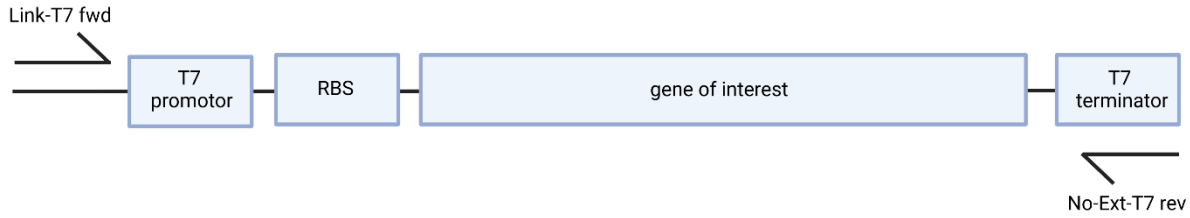

Figure 4.6: Input DNA for PACMAN

The input DNA was prepared by PCR (composition and temperature profile shown in Table 4.2 and 4.3).

Table 4.2: Reagents for preparation of input DNA for PACMAN. Primer sequences shown in Table 4.1.

Reagent	Volume [µl]
5 x HF buffer	10
dNTPs [10 mM each]	1
Primer [10 µM]: Link-T7-fwd	2.5
Primer [10 µM]: No-Ext-T7 rev	2.5
DMSO	1.5
Template DNA [100 pg]	1
Milli-Q Water	31
Phusion Polymerase	0.5

Table 4.3: PCR temperature profile of preparation of input DNA for PACMAN

Temperature [°C]	Time	Cycles
98	2 min	
98	30 s	
57	30 s	|
72	1 min	35 x
72	5 min	|
15	hold	

After PCR, the products were loaded to an 1% agarose gel and extracted. After concentration determination, the DNA was used in PACMAN reaction.

4.6.4 Preparation of agarose gel

1% (w/v) agarose gel was prepared using 1 x tris-acetate-EDTA (TAE) buffer. 3 µl 10,000 x GelRed DNA staining solution was added after cooling. DNA samples were mixed with 6 x DNA loading buffer, loaded to the gel and run at 120 V for 1 h. DNA was visualized using a G:Box gel documentation system. For extraction, the bands were cut out using a scalpel while being illuminated using a TruBlu Blue Light Transilluminator. The band was extracted using NucleoSpin Gel and PCR Clean-up Mini kit by Macherey-Nagel. DNA was eluted using 30 µl 5 mM Tris pH 8.5 supplied in the kit after heating to 65 °C at 800 rpm for 5 min.

The cloning of the reamplified DNA was done using Gibson assembly. The DNA fragments harbouring homologous ends to the pIgV plasmid were mixed in a ratio of 1:3 with the 1.33 x Gibson assembly mixture (starting material, 5x Isothermal Gibson Buffer: 25% PEG-8000, 500 mM Tris pH 7.5, 50 mM $MgCl_2$, 50 mM DTT, 5 mM NAD, 1 mM of each of the four dNTPs. Gibson assembly mixture: 50 µl 5x Isothermal Gibson Buffer, 0.625 µl in-house Taq DNA ligase (1600 U/µl), 0.5 µl in-house T5 exonuclease (2 U/µl), 3.1 µl Phusion polymerase (2 U/µl), 133.3 µl Milli-Q water) and incubated for 1 h at 50 °C.

4.6.5 Determination of DNA concentration

The concentration of the DNA was measured using a NanoDrop 2000 photospectrometer. 1.5 µl of the nucleic acid solution was applied. A spectrum was measured and the concentration measured by the absorbance at 260 nm.

4.6.6 Gibson Assembly

For Gibson assembly reactions, the pIgV plasmid was linearized via PCR reaction (composition and temperature profile shown in Table 4.4 and 4.5).

Table 4.4: Reagents for linearization reaction of the pIgV plasmid. Primer sequences shown in Table 4.1.

Reagent	Volume [µl]
2x CloneAmp HiFi PCR Mix	25
Primer Vector Amplification [10 µM] fwd	2.5
Primer Vector Amplification [10 µM] rev	2.5
Template DNA: pIgV plasmid [100 pg]	1
Milli-Q Water	19

Table 4.5: PCR temperature profile of the linearization of the pIgV plasmid

Temperature [°C]	Time	Cycles
98	2 min	
98	30 s	
57	30 s	|
72	2 min	35 x
72	5 min	|
15	hold	

4.6.7 Purchased peptide

The TEV target ([biotin][PEG12]K(5-FAM)MKGDGGSENLYQSGDHGDGSC(Cy5)) with a size of 4.1799 kDa was purchased by Pepscan. The peptide was stored as 1.66 nmol aliquots using hexafluoroisopropanol (HFIP) and lyophilization.

4.6.8 Coupling of biotinylated primers and target peptide to the microbeads

$5x10^7$ streptavidin coated microbeads were used. They were washed three times with 200 µl bind/wash buffer (20 mM Tris pH 7.5, 1 M NaCl, 1 mM EDTA, 0.05% Triton X-100) and resuspended in 50 µl of the same buffer. 120,000 molecules of biotinylated primers (b-TEG-TGS-Link-T7p Fwd, see Table 1) were used per microbead by taking 1 µl of 10 µM of the biotinylated primers, adding and respectively quick vortexing to disperse the primers and microbeads evenly. Subsequently, the microbeads were incubated at 1400 rpm at RT for 30 min. 10^6 TEV target peptides were coupled per bead. For this, one 1.66 nmol aliquot was dissolved in 500 µl 1x PBS. 25 µl of the solution was added to the microbead suspension and incubated over night at 1400 rpm at 7 °C. Afterwards, the microbeads were washed three times

using 200 µl breaking buffer (10 mM Tris pH 8, 100 mM NaCl, 1% Triton X-100, 1% SDS) using a magnetic rack and then incubated over night at 1400 rpm at 7 °C. The microbeads were washed three times with 200 µl bind/wash buffer and resuspended in 100 µl bind/wash buffer supplemented with 0.1% NaN_3 and store at 4 °C for several months.

4.6.9 On-bead emPCR

The on-bead emPCR was performed as described in Hasecke *et al.,* in preparation. As optimized by the authors, 10^6 ProMag HP3 streptavidin coated microbeads coupled to 120,000 biotinylated primers (see Table 4.1) per microbead were used. The microbeads were washed three times with 100 µl Milli-Q water and resuspended in a concentration of 500,000 microbeads/µl in Milli-Q water. The PCR solution was prepared as shown in Table 4.6.

Table 4.6: Reagents for on-bead emPCR. Primer sequence shown in Table 4.1.

Reagent	Volume [µl]
10x Titanium Taq buffer	1.8
dNTPs [10 mM each]	0.45
Primer No-Ext-T7 [10 µM] rev	1.8
Milli-Q water	10.05
Microbeads in Milli-Q water	2
Template DNA ($4x10^6$ molecules/µl)	1
Titanium Taq polymerase	0.9

The PCR solution was vortexed shorty. Subsequently, 54 µl 2% FluoSurf (Dolomite Microfluidics) were added to the PCR solution in a 200 µl PCR tube. The tube was vortexted for 5 min at RT using a VWR VV3 vortex device on speed setting 5 of 6. PCR was performed to the temperature profile shown in Table 4.7.

Table 4.7: PCR temperature profile of the on-bead emPCR

Temperature [°C]	Time	Cycles
94	2 min	
94	30 s	|
48	30 s	30 x
72	2-4 min	|
72	5 min	
45	5 min	
25	20 min	
15	hold	

After the PCR, the emulsion was broken, and the microbeads were recovered. Therefore, the emulsion was transferred to a fresh 0.5 ml low-bind reaction tube. The PCR tube was rinsed with 200 µl breaking buffer (see: 4.6.8 Coupling of biotinylated primers and target peptide to the microbeads) and transferred to the new reaction tube. 60 µl Fluoro-Stop (Dolomite Microfluidics) was added. The tube was shaken to break the emulsion. By a quick spin-down centrifugation the aqueous and the organic phases were separated. In the upper, aqueous phase, the microbeads were located. This phase was transferred into a new 1.5 ml reaction tube. With the help of a magnetic rack, the microbeads were collected on the side of the tube allowing easy removal of the liquid. The microbeads were washed three times with 200 µl breaking buffer and incubated over night at 7°C at 1400 rpm. The next day, the microbeads were washed three times with 200 µl bind/wash buffer (see: 4.6.8 Coupling of biotinylated primers and target peptide to the microbeads) and incubated over night at 7 °C at 1400 rpm. Then, the microbeads were washed three times with 200 µl TE-buffer (10 mM Tris pH 8, 1 mM EDTA).

4.6.10 IVTT

After on-bead emPCR, the microbeads were washed twice with 100 µl 1x PBS and twice with 100 µl 1x PBS with supplemented 1 mg/ml ultrapure BSA. The aqueous solution was removed and the microbeads were resuspended in 50 µl PURExpress IVTT solution (New England Biolabs). From this point onwards, the mixture was kept on ice. A total volume of 500 µl of mineral oil supplemented with 2% ABIL® EM 90 and 0.05% Triton X-100 was placed in a 2 ml glass vial (Agilent HPLC supplies) with a 2x7 mm stirring bar. The glass vial was placed into the iTrapR (a self-made stirring device) surrounded by crushed ice and water. The speed was

set to 1,200 rpm and a timer was set to 10 min. The PURExpress IVTT mix was prepared as shown in Table 4.8.

Table 4.8: Reagents used for IVTT

Reagent	Volume [µl]
Solution A (PURExpress kit, NEB)	20
Solution B (PURExpress kit, NEB)	15
RNAse inhibitor, murine (NEB)	0.5
PURExpress disulfide bond enhancer 1 (NEB)	2
PURExpress disulfide bond enhancer 2 (NEB)	2
DnaK (Genefrontier)	2
GroE Mix (Genefrontier)	2
GroE Mix dilution buffer (Genefrontier)	1.33
UltraPure BSA (Invitrogen)	1
Triton X-100 [10 %]	2.5
Trace Metal Mix A5 with Co (1:100 in Milli-Q water)	0.5
Milli-Q water	2

The IVTT solution was mixed by pipetting up and down and added in steps of 10 µl per minute to the stirring mineral oil. Right before transferring each aliquot, the IVTT solution was sonicated in a sonication bath quickly. After the whole IVTT solution was added, the stirring continued for another 5 min. The emulsion transferred to a 1.5 ml reaction tube. The emulsion was incubated at 37 °C for 4 h without shaking. During the incubation time, the TEV protease was expressed, and the cleavage reaction took place. The microbeads were recovered from the emulsion by a centrifugation step at 16,000 xg at RT for 15 min. The supernatant was removed, and the pellet resuspended in 200 µl of breaking buffer (see: 4.6.8). 1 ml of diethyl ether was added, and the reaction tube was vortexed. By a brief centrifugation step, the aqueous and the oil phase were separated. The upper diethyl ether phase was discarded. The microbeads were collected using a magnetic rack and the liquid was removed. The microbeads were washed with 200 µl breaking buffer, resuspended in 100 µl breaking buffer and transferred to a new 1.5 ml reaction tube. The microbeads were washed twice more with 100 µl breaking buffer and incubated at 1,400 rpm at 7 °C over night. The next day, the microbeads were washed another three times with breaking buffer and subsequently five times with 1x PBS before analysed and sorted using FACS.

4.6.11 FACS

Fluorescence-activated cell sorting was performed using a BD FACS ARIA III or a Beckman Coulter CytoFLEX SRT device. The microbeads were diluted with 1x PBS in a 5 ml flow cytometry tube. Single microbeads were gated using the forward scatter (FSC) and side scatter (SSC) using a linear scale. The cleavage status was evaluated using the FITC and the APC channel. The sort gate was determined as described in the result section. The microbeads were sorted in 96-well plates which were used for PCR reamplification of the DNA coupled to the microbeads. Data analysis was performed using python version 3.8, FlowCal version 1.3.0 and matplotlib version 3.3.0.

4.6.12 Reamplification of the DNA coupled to the sorted microbeads

The DNA coupled to the sorted microbeads was reamplified using PCR. The PCR was performed as shown in Table 4.9.

Table 4.9: Reagents used for reamplification PCR after PACMAN. x indicates the volume of sorted microbeads.

Reagent	Volume [µl]
5x HF-buffer	10
dNTPs [10 mM each]	1
Primer Link-T7 [10 µM] fwd	2.5
Primer No-Ext-T7 [10 µM] rev	2.5
DMSO	1.5
Milli-Q water	32 minus x
Phusion Polymerase	0.5

The temperature profile shown in Table 4.3 was applied.

5 PACMAN selection against Islet Amyloid Polypeptide

5.1 Project information

This chapter reflects content of the following project.

The following people contributed to this project:

Anne Pfitzer, Filip Hasecke, Stefanie Williams, Robin Backer, Wolfgang Hoyer

5.2 Abstract

Type 2 *diabetes mellitus* (T2DM) is a prevalent and escalating global health concern linked to the aggregation of islet amyloid polypeptide (IAPP) in the pancreas. While various treatments exist, none provides a cure for T2DM. Here, we introduce a potentially groundbreaking strategy for T2DM cure using proteolytically active antibodies capable of cleaving cytotoxic IAPP aggregates. Utilizing the method of Proteolytic Antigen Cleavage-Mediated AmplificatioN (PACMAN), we aimed to select antibodies targeting IAPP. The antibodies were derived from human DNA antibody libraries focusing on nanobodies and single-chain variable fragments (scFv). The PACMAN process involved iterative rounds of antibody selection against a double fluorophore labelled IAPP target peptide. The cleavage success was assessed using reversed-phase chromatography (RP-HPLC). While initial tests were promising, subsequent experiments revealed complexity and ambiguous results. The project has nevertheless established a foundation for future investigations. Involving mass spectrometry and optimization of the antibody library could unlock solutions. Beyond T2DM, the use of proteolytic antibodies is promising for addressing other diseases associated with protein aggregation.

5.3 Introduction

Diabetes mellitus Type 2 (T2DM) is an uncurable disease associated to the fibrillar aggregation of islet amyloid polypeptide (IAPP) (230). In more than 90% of T2DM patients, IAPP deposits are found in the pancreas (222-224). IAPP is co-secreted with insulin and prone to aggregation. These aggregates are known to have cytotoxic effects on the Langerhans islets of the pancreas. As more than 480 million people around the world are affected and the number is constantly increasing (311), the demand for effective treatment is very high. The current treatments include radical changes of lifestyle including diet and exercise (125). Another widely used treatment is the oral intake of metformin (312) inhibiting gluconeogenesis through different mechanisms after arrival in the liver (140). There are more oral agents as sulfonylureas and meglitinides triggering insulin secretion (313) and alpha-glucosidase

inhibitors reducing postprandial hyperglycaemia to name only a few (125). In addition also injectable agents are available like glucagon-like peptide-1 (GLP1) stimulating insulin release (314) or insulin directly (145). Other treatments include colesevelam reducing low density lipoprotein (LDL) cholesterol in patients with hypercholesterolemia or bromocriptine lowering the blood glucose level (125). All of these treatments improve quality of living but have side-effects and do not cure T2DM.

A curing mode of action could be the utilization of proteolytically active antibody variants (315) cleaving the cytotoxic IAPP aggregates on site (Figure 5.1).

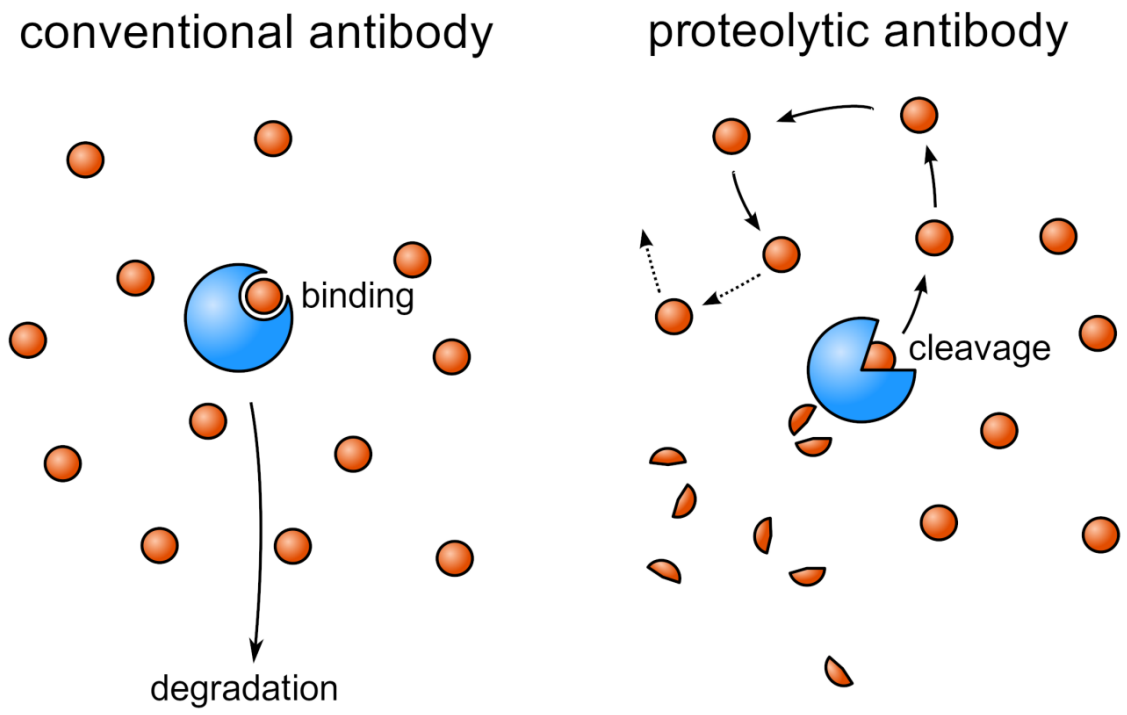

Figure 5.1: Schematic mode of action of proteolytic antibodies. In contrast to conventional antibodies, proteolytic antibodies do not only bind the target and recruit immune cells but recognize their target and degrade it directly. While a conventional antibody is degraded after its recognition reaction, a proteolytic antibody is able to react several times.

Proteolytically active antibodies are antibodies with protease-like activities. Taguchi *et al.* (316) and Paul *et al.* (317) reported that the peptide fragments of Alzheimer's disease (AD) associated Amyloid-β (Aβ) are incapable of building amyloid aggregates again. Inspired by those findings, we decided to apply our method "Proteolytic Antigen Cleavage-Mediated AmplificatioN" (PACMAN) and select antibodies against IAPP. Finding suitable antibodies could be a gamechanger in the fight against T2DM.

5.4 Results and Discussion

5.4.1 Construction of the antibody library

A novel approach to find a cure to T2DM could be the implementation of proteolytically active antibodies as described by Paul *et al.* (315, 317) selected by PACMAN. For PACMAN, a DNA library is required. The DNA templates cannot be longer than 2 kb due to amplification efficiency. Taguchi *et al.* (316) have already reported about the discovery of catalytically active scFv and immunoglobulins (Ig) against Aβ consisting of two lambda light-chains (VL) both of a size of approximately 800 kb. Therefore, we chose to focus on these scFv which are non-natural fusion proteins of heavy (VH) and light chains of Ig connected via a peptide linker (318) as well as on nanobodies that are not present in humans, but in camelids and cartilaginous fish (319, 320) (Figure 5.2A). Additionally, we involved double VH and double VL antibody derivatives to our repertoire (Figure 5.2A). Naturally occurring nanobodies only consist of heavy chains and lack light chains (321). Due to the reported success of Taguchi *et al.* (316) we additionally took nanobodies consisting of only a VL into account (Figure 5.2A). The avoidance of antibodies' constant domains (Fc) might be also beneficial due to their proinflammatory characteristics caused by glycosylation sites (322, 323) which are eradicated by not utilizing Y-shaped antibodies.

The antibody library used for PACMAN against IAPP was derived from ten human naïve buffy coats. A scheme of the library assembly is shown in Figure 5.2B. After the extraction of peripheral mononuclear cells (PBMCs) from buffy coats, mRNA isolation with subsequent cDNA synthesis was performed. The variable regions were amplified using specific primers (overview SI Figure 5.1A, primer sequences in Table 5.2) adding overhangs to the pIgV plasmid (see 4.6.1). For the LibIgV_2 library, the library consisting of antibody variants constructed of two fragments, either two heavy chains, two light chains, one 3' heavy chain and one 5' light chain and vice versa, two PCRs had to be performed to produce fragments harbouring 5' pIgV plasmid overhangs, a start codon (forward primer) and a 3' part encoding part of the $(G_4S)_4$ linker (reverse primer) and other fragments encoding on the 5' end a part of the $(G_4S)_4$ linker (forward primer) and on the 3' end a stop codon and pIgV plasmid overlapping sequences (reverse primer). The two chains were annealed via PCR (as shown in Figure 5.2B) and cloned into the pIgV vector via Gibson assembly. In case of LibNano, the library consisting only of nanobodies, only one PCR had to be performed producing constructs harbouring the pIgV overlap sequence end and the start codon on the 5' end (forward primer) and a stop codon and overlaps to the pIgV plasmid on the 3' end (reverse primer). Both of the libraries were sequenced using the PacBio Next Generation Sequencing method. The outcome was analysed by Filip Hasecke using the capture-recapture model. For this, all antibody sequences were divided into two groups and compared in order to find identical sequences in both groups.

The calculation yielded in 1.1 ± 0.09 x 10^8 for the LibNano and 6.6 ± 0.04 x 10^5 for the LibIgV_2 library different sequences.

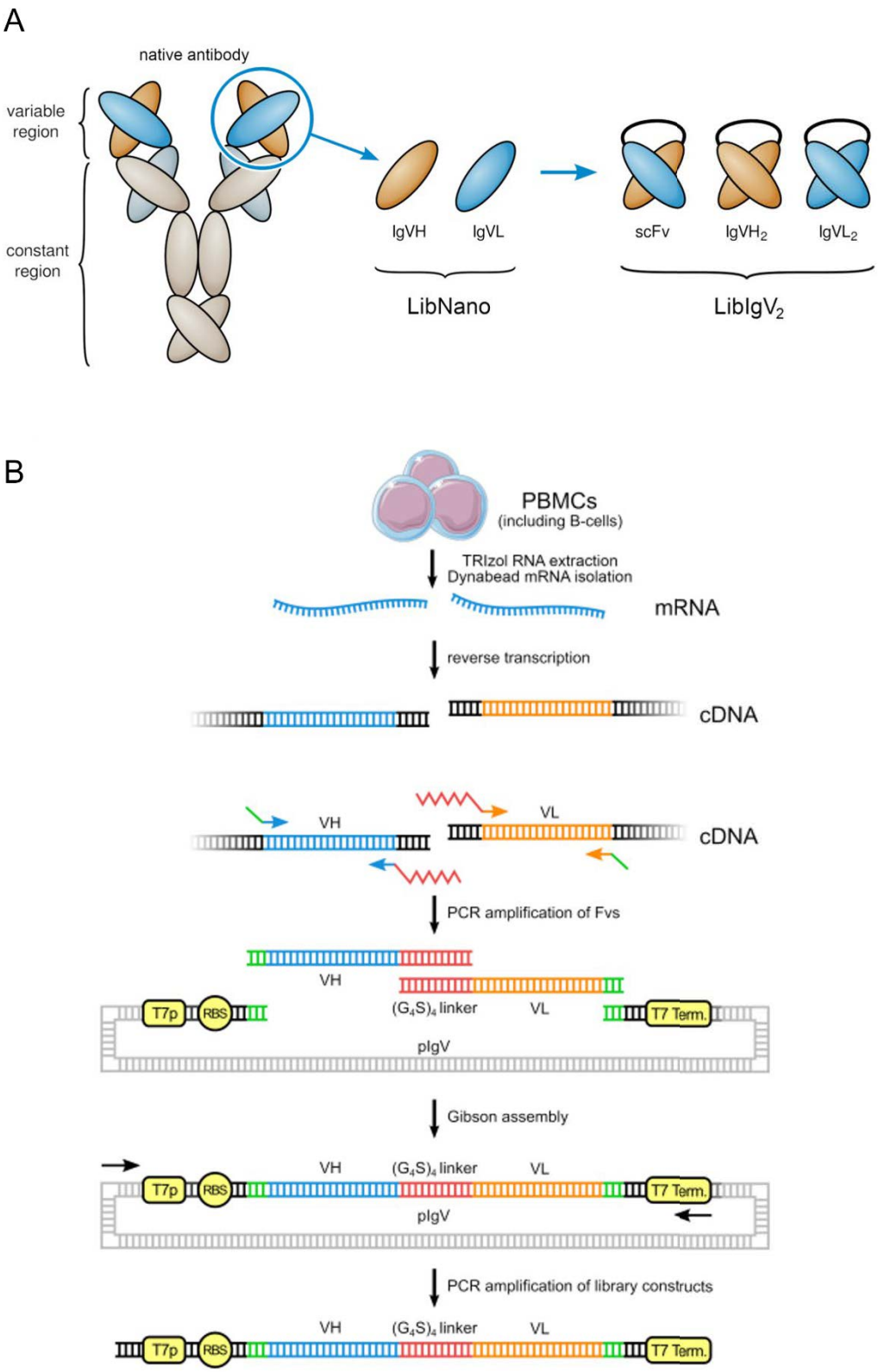

Figure 5.2: Scheme of the construction of the antibody library. A: In the antibody library, a LibNano consisting of only a heavy or a light chain is included as well as a LibIgV$_2$ consisting of scFv, IgVH$_2$ and IgVL$_2$. All of the antibody variants only exhibited the variable, but not the constant region of ordinary antibodies. **B:** Cloning strategy for the antibody library of scFv. The starting material were PBMCs. After RNA extraction and cDNA synthesis, the heavy and light chain regions were amplified. An overlap to the pIgV vector, a start codon and a linker sequence or a linker sequence, a stop codon and an overlap to the pIgV vector were added via PCR. The fragments were cloned using Gibson assembly. For PACMAN, the genes of interest were amplified and linearized.

5.4.2 Optimizing the conditions for the read out of successful cleavage of the IAPP target by proteolytic antibodies

The PACMAN method requires the binding of a double fluorophore labelled, biotinylated target peptide against which specific antibodies can be selected. An IAPP target peptide (Figure 5.3A) was purchased. As a read out for successful cleavage of the peptide by proteolytic antibodies, reversed-phase (RP) chromatography was chosen. Due to low solubility of the IAPP target peptide and weak visibility in the chromatogram (Figure 5.3B), the IAPP target peptide was supplemented with either 20% (v/v) dimethylformamide (DMF) (324) (Figure 5.3C) or 50% (v/v) 8 M guanidium hydrochloride (GdmCl) (325) (Figure 5.3D). As the visibility of the IAPP target peptide was best when supplemented with 50% (v/v) of 8 M GdmCl, we decided to add 50% (v/v) GdmCl to every sample right before loading to the high performance liquid chromatography (HPLC) system.

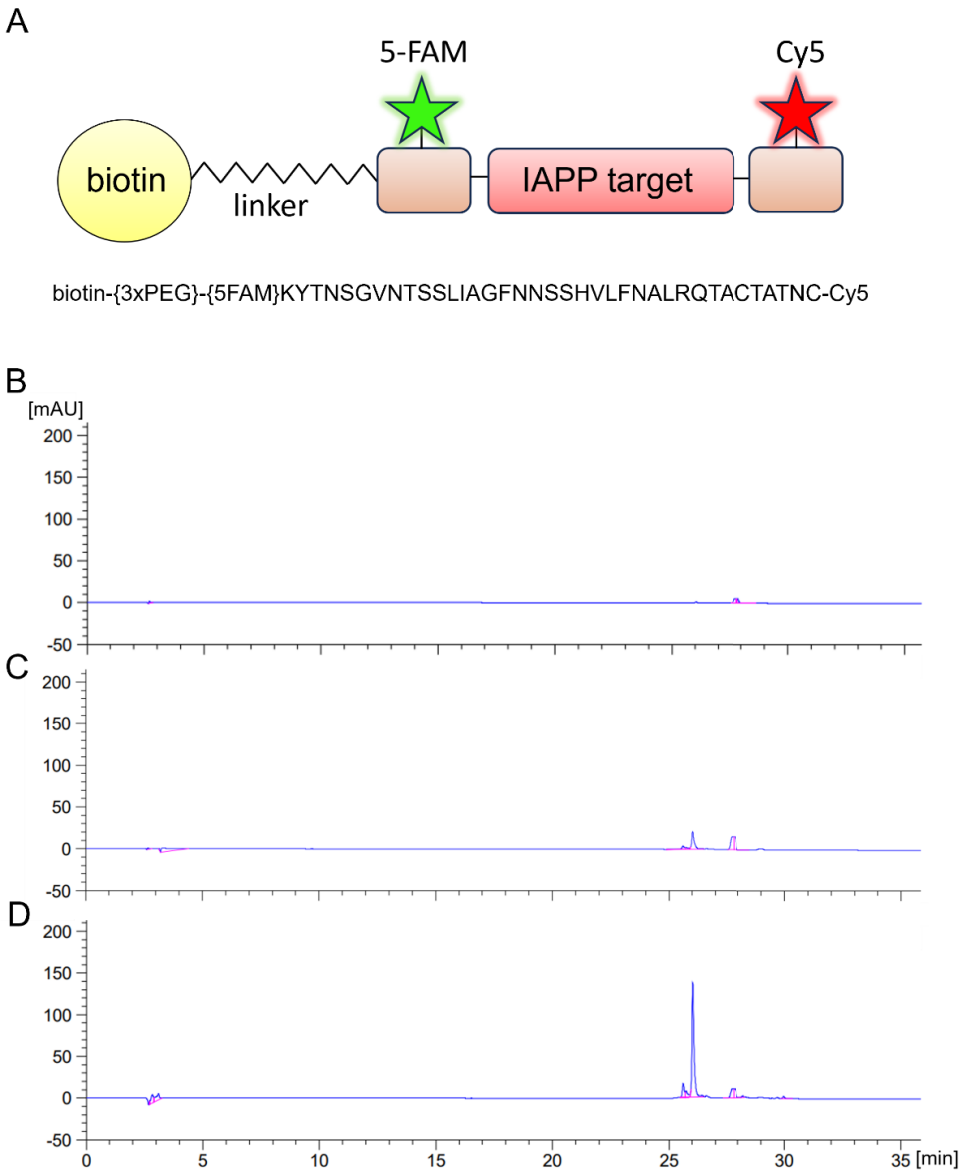

Figure 5.3: Solubility optimization of the IAPP target peptide to improve the read out quality in HPLC analyses. A: Scheme of the IAPP target peptide consisting of a modified IAPP peptide labelled to biotin, a 3xPEG linker and two fluorophores: 5-FAM and Cy5. **B:** RP-HPLC run of the IAPP target peptide. **C:** RP-HPLC run of the IAPP target peptide mixed with 20% (v/v) DMF right before loading to the HPLC system. **D:** RP-HPLC run of the IAPP target peptide mixed with 50% (v/v) GdmCl right before loading to the HPLC system. For all samples, a Zorbax 300SB-C8 4.6x250 mm column was used and a linear gradient of 0-80% trifluoroacetic acid (TFA) over 40 min applied. Cut 0.5 ml Protein LoBind reaction tubes by Eppendorf were placed in HPLC glass vials as reaction tubes. The samples had a total volume of 50 µl. The absorbance at 633 nm is illustrated.

5.4.3 Performance of two rounds of PACMAN and seemingly cleavage success of the IAPP target peptide by proteolytic antibodies

PACMAN was performed using the LibNano Library. The library of scFv, $IgVH_2$ and $IgVL_2$ "$LibIgV_2$" was disregarded as amplification of the library from the microbeads was not successful as shown in SI Figure 5B. After the first round of PACMAN, the green-shifted population was collected, the DNA binding to the streptavidin coated microbeads amplified and reused as starting material for the next round of PACMAN. Again, the DNA binding to the streptavidin coated microbeads was amplified. From both rounds of amplification, the DNA was used as template DNA for in vitro transcription and translation (IVTT). Therefore, 25 µM of the IAPP target peptide was incubated with IVTT solution expressing and synthesizing the LibNano variants over night at 37 °C and analysed using reversed-phase HPLC (Figure 5.4). In Figure 5.4B and Figure 5.4C a new peak after 24.5 ml is visible. This peak was neither detected in the control sample of IAPP target peptide incubated in 1x PBS over night at 37 °C (Figure 5.4A), nor in a control sample of IAPP target peptide incubated over night at 37 °C together with IVTT solution without any DNA (Figure 5.4D). The fact that the height of the main peak of the IAPP target peptide eluting after 26 ml did not correspond to the height of the IAPP target control sample (Figure 5.4A) indicated the complicated distribution of the IAPP target peptide in the sample due to its still low solubility, even though 50% GdmCl (v/v) were added right before loading. In Figure 5.4E another control sample is shown in which the IAPP target peptide was not added to the sample, but only IVTT solution and DNA from PACMAN round 1. The appearing peak could indicate that the cleavage reaction was successful. From the FACS data (data not shown), a successful cleavage reaction was not fully observable as the populations could not be distinguished clearly. With both DNA samples, a transformation of XL1-Blue Competent Cells was performed. The transformation efficiency was poor and only 5 clones could be sent for sequencing. From these 5 clones, only one clone corresponded to a nanobody sequence. IVTT with the reamplified DNA did not result in a promising result evaluated with HPLC (data not shown).

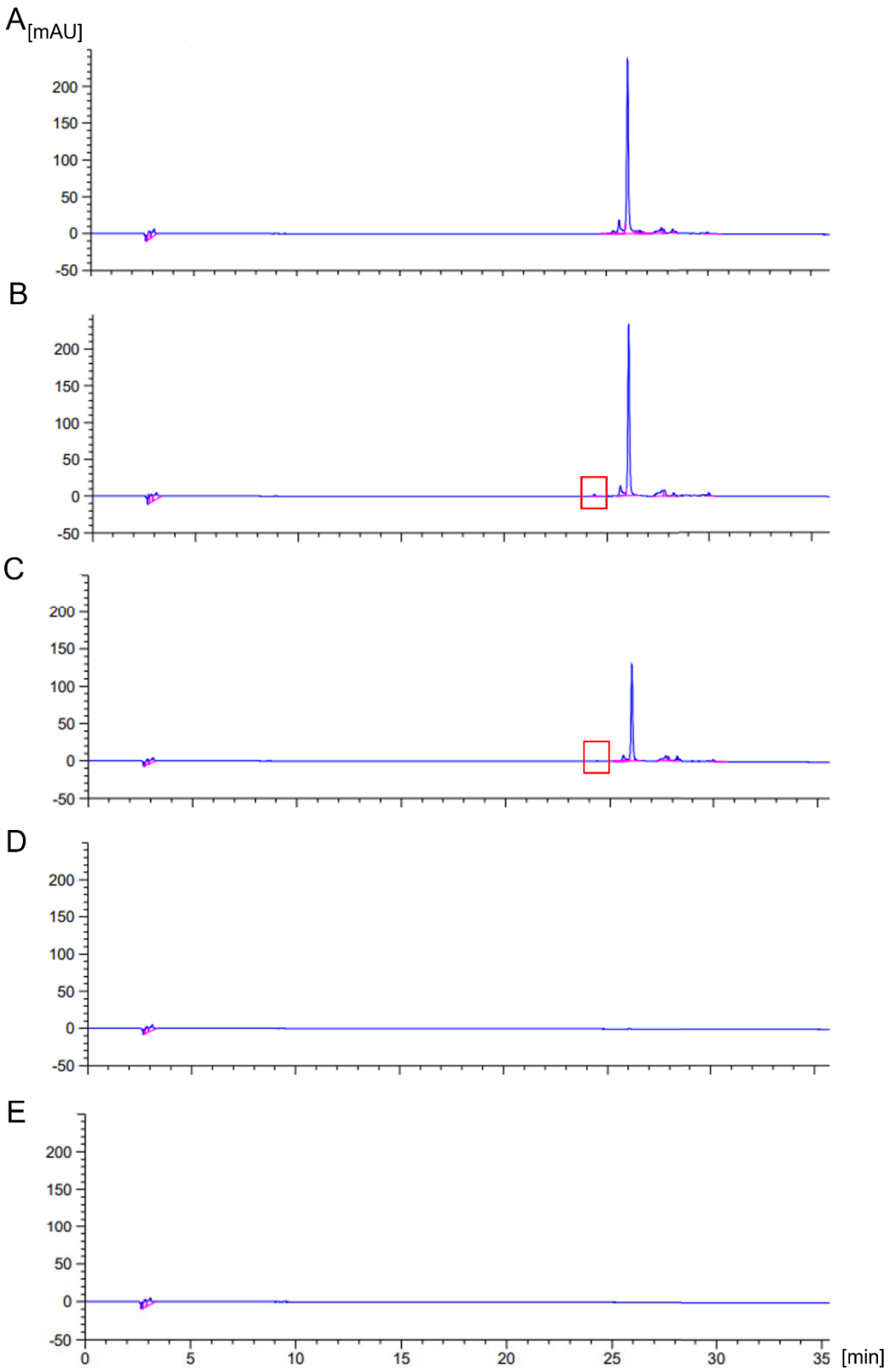

Figure 5.4: Seemingly successful cleavage of the IAPP target peptide with DNA taken from PACMAN round 1 and 2. A: IAPP target control. **B:** IAPP target peptide incubated in IVTT solution with LibNano DNA from PACMAN round 1 over night at 37°C. **C**: IAPP target peptide incubated in IVTT solution with LibNano DNA from PACMAN round 2 over night at 37 °C. **D:** IAPP target peptide incubated in IVTT solution without added DNA over night at 37 °C. **E:** IVTT solution with LibNano DNA from PACMAN round 1. All samples were analysed using RP-HPLC using a Zorbax 300SB-C8 4.6x250 mm column and applying a linear gradient of 0-80% trifluoroacetic acid (TFA) over 40 min. Cut 0.5 ml Protein LoBind reaction tubes by Eppendorf were placed in HPLC glass vials as reaction tubes. The samples had a total volume of 50 µl. The absorbance at 633 nm is illustrated.

To confirm the apparent successful result, the experiment was repeated with the DNA from PACMAN round 2. Again, a new peak could be observed (Figure 5.5B) which was not detected in the IAPP target peptide control sample. Unfortunately, in the control sample of IAPP target peptide in IVTT solution without any added DNA of this experiment, this once promising peak appeared as well, however much smaller (Figure 5.5C). It must be mentioned that the sample in which no nanobody was present because no DNA was added to the IVTT was loaded before the sample of IAPP target peptide in IVTT with added nanobody DNA was loaded. Hence a takeover of the sample is excluded. The successful cleavage of the target cannot be excluded entirely by the unpleasant appearance of the peak, but a bijective positive result is still pending.

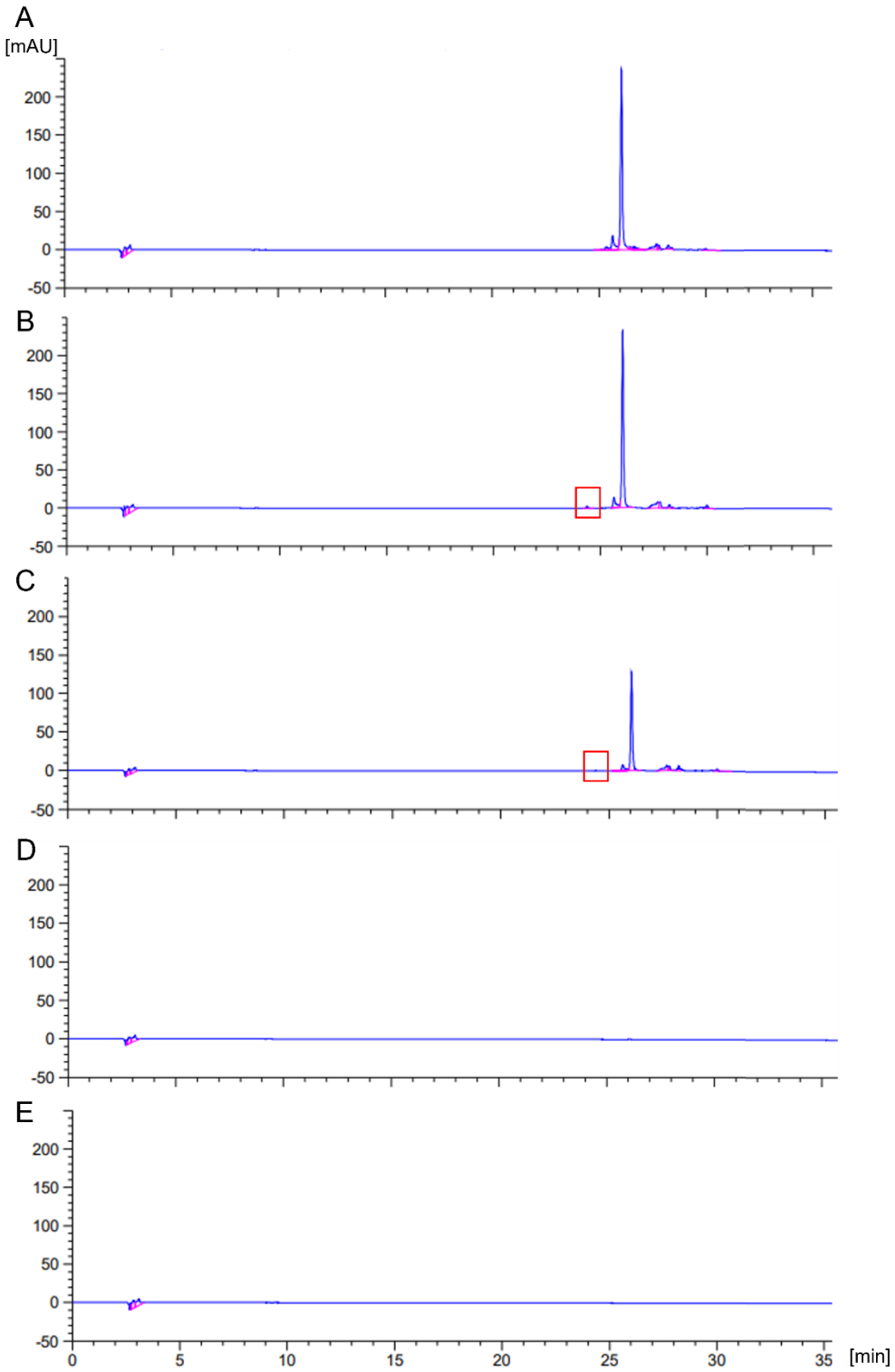

Figure 5.5: The revealing truth of the success of PACMAN against the IAPP target peptide utilizing LibNano. A: IAPP target control. **B:** IAPP target peptide incubated in IVTT solution with LibNano DNA from PACMAN round 2 over night at 37°C. **C:** IAPP target peptide incubated in IVTT solution without added DNA over night at 37 °C. **D:** IVTT solution with LibNano PACMAN round 2 DNA. **E:** IVTT solution without any added DNA. All samples were analysed using RP-HPLC using a Zorbax 300SB-C8 4.6x250 mm column and applying a linear gradient of 0-80% trifluoroacetic acid (TFA) over 40 min. Cut 0.5 ml Protein LoBind reaction tubes by Eppendorf were placed in HPLC glass vials as reaction tubes. The samples had a total volume of 50 µl. The absorbance at 633 nm is illustrated.

5.5 Outlook

PACMAN against the IAPP target peptide was performed. The seemingly successful cleavage of the target peptide was left in doubt after the repetition of the experiment. Although LibNano DNA was successfully reamplified after the PACMAN rounds, the result is not conclusive. At least the appearing peak in the control sample was smaller than the same peak in the cleavage sample. This keeps the chance of a real positive hit, but nevertheless, the result has to be confirmed by other methods than RP-HPLC.

Repeating PACMAN and sending the collected peaks to mass spectrometry to gain information about their identity would be of great interest. Another interesting aspect is the optimization of the amplification of the antibody library "LibIgV_2". In this library, there might be potent antibodies present against the IAPP target peptide.

In addition, other target peptides can be tested as they might be suitable candidates for the prepared antibody libraries.

5.6 Materials and Methods

5.6.3 Plasmids

The plasmid used in PACMAN is termed pIgV and derived from the PURExpress® In Vitro Protein Synthesis kit by New England Biolabs. The gene in this plasmid, DHFR, was removed and a new cloning site containing the restriction sites SalI and NotI were introduced.

5.6.4 Primers

Here, the primers for the amplification of the VH families are shown.

The forward primers shown in Table 5.1 introduce an overlap sequence to the pIgV plasmid and a start codon. They exhibit the complementary sequence of the stated VH family sequences (bold).

Table 5.1: Forward primers introducing overlaps to the pIgV plasmid and a start codon in the VH family sequences. VH family part is printed in bold.

VH family primer	Sequence 5' → 3'
Vec-SalI-ATG-VH1/7-For	AGGAGAGTCGACATGGCC**CARRTSCAGCTGGTRCART CTGG**
Vec-SalI-ATG-VH1-For	AGGAGAGTCGACATGGCC**SAGGTBCAGCTGGTGCAGT CTGG**
Vec-SalI-ATG-VH2-For	AGGAGAGTCGACATGGCC**CAGRTCACCTTGAAGGAGT CTGG**
Vec-SalI-ATG-VH3_1-For	AGGAGAGTCGACATGGCC**SARGTGCAGCTGGTGGAGT CTGG**
Vec-SalI-ATG-VH3_2-For	AGGAGAGTCGACATGGCC**GAGGTGCAGCTGKTGGAG WCYSG**
Vec-SalI-ATG-VH4_1-For	AGGAGAGTCGACATGGCC**CAGGTGCAGCTGCAGGAGT CGGG**
Vec-SalI-ATG-VH4_2-For	AGGAGAGTCGACATGGCC**CAGSTGCAGCTRCAGSAGT SSGG**
Vec-SalI-ATG-VH5-For	AGGAGAGTCGACATGGCC**GARGTGCAGCTGGTGCAGT CTGG**
Vec-SalI-ATG-VH6-For	AGGAGAGTCGACATGGCCCAGGTACAGCTGCAGCAGT CAGG

The following forward primers shown in Table 5.2 introduce part of the $(G_4S)_4$ linker sequence. They exhibit the complementary sequence of the stated VH family sequence (bold).

Table 5.2: Forward primers introducing part of the $(G_4S)_4$ linker sequence in the VH family sequences. VH family part is printed in bold.

VH family primer	Sequence 5' → 3'
Link-VH1/7-For	AGCGGCGGCGGCGGCTCTGGTGGTGGTGGATCC**CARRTSCAGCTGGTRCARTCTGG**
Link-VH1-For	AGCGGCGGCGGCGGCTCTGGTGGTGGTGGATCC**SAGGTBCAGCTGGTGCAGTCTGG**
Link-VH2-For	AGCGGCGGCGGCGGCTCTGGTGGTGGTGGATCC**CAGRTCACCTTGAAGGAGTCTGG**
Link-VH3_1-For	AGCGGCGGCGGCGGCTCTGGTGGTGGTGGATCC**SARGTGCAGCTGGTGGAGTCTGG**
Link-VH3_2-For	AGCGGCGGCGGCGGCTCTGGTGGTGGTGGATCC**GAGGTGCAGCTGKTGGAGWCYSG**
Link-VH4_1-For	AGCGGCGGCGGCGGCTCTGGTGGTGGTGGATCC**CAGGTGCAGCTGCAGGAGTCGGG**
Link-VH4_2-For	AGCGGCGGCGGCGGCTCTGGTGGTGGTGGATCC**CAGSTGCAGCTRCAGSAGTSSGG**
Link-VH5-For	AGCGGCGGCGGCGGCTCTGGTGGTGGTGGATCC**GARGTGCAGCTGGTGCAGTCTGG**
Link-VH6-For	AGCGGCGGCGGCGGCTCTGGTGGTGGTGGATCCC**AGGTACAGCTGCAGCAGTCAGG**

The reverse primers shown in Table 5.3 represent complementary sequences of the stated JH antibody family sequences (bold). They introduce a stop codon and an overlap to the pIgV plasmid.

Table 5.3: Reverse primers introducing a stop codon and an overlap to the pIgV plasmid in the JH family sequences. JH family part is printed in bold.

JH family primer	Sequence 5' → 3'
JH1_2_4_5-Vec-Rev	CTGCTCTGCTGCACC**TGAGGAGACRGTGACCAGGGTKCC**
JH3_6-Vec-Rev	CTGCTCTGCTGCACC**TGARGAGACGGTGACCRKKGTCCC**

The reverse primers shown in Table 5.4 represent complementary sequences of the stated JH antibody family sequences (bold). They introduce part of the $(G_4S)_4$ linker sequence.

Table 5.4: Reverse primers introducing part of the $(G_4S)_4$ linker sequence in the JH family sequences. JH family part is printed in bold.

JH family primer	Sequence 5' → 3'
JH1_2_4_5-Rev-Link	ACCAGAGCCGCCGCCGCCGCTACCACCACCACC**TGAGGAGACRGTGACCAGGGTKCC**
JH3_6-Rev-Link	ACCAGAGCCGCCGCCGCCGCTACCACCACCACC**TGARGAGACGGTGACCRKKGTCCC**

Here, the primers for the amplification of the VK families are shown.

The forward primers shown in Table 5.5 introduce an overlap sequence to the pIgV plasmid and a start codon. They exhibit the complementary sequence of the stated VK family sequences (bold).

Table 5.5: Forward primers introducing overlaps to the pIgV plasmid and a start codon in the VK family sequences. VK family part is printed in bold.

VK family primer	Sequence 5' → 3'
Vec-SalI-ATG-VK1-For	AGGAGAGTCGACATGGCC**GMCATCCRGWTGACCCAGTCTCC**
Vec-SalI-ATG-VK2-For	AGGAGAGTCGACATGGCC**GATRTTGTGATGACYCAGWCTCC**
Vec-SalI-ATG-VK3-For	AGGAGAGTCGACATGGCC**GAAATWGTGWTGACRCAGTCTCC**
Vec-SalI-ATG-VK4-For	AGGAGAGTCGACATGGCC**GACATCGTGATGACCCAGTCTCC**
Vec-SalI-ATG-VK5-For	AGGAGAGTCGACATGGCC**GAAACGACACTCACGCAGTCTCC**
Vec-SalI-ATG-VK6-For	AGGAGAGTCGACATGGCC**GAWRTTGTGMTGACWCAGTCTCC**

The following forward primers shown in Table 5.6 introduce part of the $(G_4S)_4$ linker sequence. They exhibit the complementary sequence of the stated VK family sequence (bold).

Table 5.6: Forward primers introducing part of the $(G_4S)_4$ linker sequence in the VK family sequences. VK family part is printed in bold.

VK family primer	Sequence 5' → 3'
Link-VK1-For	AGCGGCGGCGGCGGCTCTGGTGGTGGTGGATCC**GMCATCCRGWTGACCCAGTCTCC**
Link-VK2-For	AGCGGCGGCGGCGGCTCTGGTGGTGGTGGATCC**GATRTTGTGATGACYCAGWCTCC**
Link-VK3-For	AGCGGCGGCGGCGGCTCTGGTGGTGGTGGATCC**GAAATWGTGWTGACRCAGTCTCC**
Link-VK4-For	AGCGGCGGCGGCGGCTCTGGTGGTGGTGGATCC**GACATCGTGATGACCCAGTCTCC**
Link-VK5-For	AGCGGCGGCGGCGGCTCTGGTGGTGGTGGATCC**GAAACGACACTCACGCAGTCTCC**
Link-VK6-For	AGCGGCGGCGGCGGCTCTGGTGGTGGTGGATCC**GAWRTTGTGMTGACWCAGTCTCC**

The reverse primers shown in Table 5.7 represent complementary sequences of the stated JK antibody family sequences (bold). They introduce a stop codon and an overlap to the pIgV plasmid.

Table 5.7: Reverse primers introducing a stop codon and an overlap to the pIgV plasmid in the JK family sequences. JK family part is printed in bold.

JK family primer	Sequence 5' → 3'
JK1-4-Vec-Rev	CTGCTCTGCTGCACC**TTTGATHTCCASYTTGGTCCC**
JK5-Vec-Rev	CTGCTCTGCTGCACC**TTTAATCTCCAGTCGTGTCCC**

The reverse primers shown in Table 5.8 represent complementary sequences of the stated JH antibody family sequences (bold). They introduce part of the $(G_4S)_4$ linker sequence.

Table 5.8: Reverse primers introducing part of the $(G_4S)_4$ linker sequence in the JK family sequences. JK family part is printed in bold.

JK family primer	Sequence 5' → 3'
JK1-4-Rev-Link	ACCAGAGCCGCCGCCGCCGCTACCACCACCACC**TTTGATHTCCASYTTGGTCCC**
JK5-Rev-Link	ACCAGAGCCGCCGCCGCCGCTACCACCACCACC**TTTAATCTCCAGTCGTGTCCC**

Here, the primers for the amplification of the VL families are shown.

The forward primers shown in Table 5.9 introduce an overlap sequence to the pIgV plasmid and a start codon. They exhibit the complementary sequence of the stated VL family sequences (bold).

Table 5.9: Forward primers introducing overlaps to the pIgV plasmid and a start codon in the VL family sequences. VL family part is printed in bold.

VL family primer	Sequence 5' → 3'
Vec-SalI-ATG-VK1-For	AGGAGAGTCGACATGGCC**CAGTCTGTGYTGACKCAGCC**
Vec-SalI-ATG-VK2-For	AGGAGAGTCGACATGGCC**CAGTCTGCCCTGACTCAGCC**
Vec-SalI-ATG-VK3-For	AGGAGAGTCGACATGGCC**TCCTMTGAGCTGACWCAG**
Vec-SalI-ATG-VK4ab-For	AGGAGAGTCGACATGGCC**CAGCYTGTGCTGACTCAATC**
Vec-SalI-ATG-VK4c-For	AGGAGAGTCGACATGGCC**CTGCCTGTGCTGACTCAGCC**
Vec-SalI-ATG-VK5-For	AGGAGAGTCGACATGGCC**CAGSCTGTGCTGACYCAGCC**
Vec-SalI-ATG-VK6-For	AGGAGAGTCGACATGGCC**AATTTTATGCTGACTCAGCCC**
Vec-SalI-ATG-VK7-For	AGGAGAGTCGACATGGCC**CAGRCTGTGGTGACTCAGGAGCCCTC**

The following forward primers shown in Table 5.10 introduce part of the $(G_4S)_4$ linker sequence. They exhibit the complementary sequence of the stated VL family sequence (bold).

Table 5.10: Forward primers introducing part of the $(G_4S)_4$ linker sequence in the VL family sequences. VL family part is printed in bold.

VL family primer	Sequence 5' → 3'
Link-VL1-For	AGCGGCGGCGGCGGCTCTGGTGGTGGTGGATCC**CAGTCTGTGY TGACKCAGCC**
Link-VL2-For	AGCGGCGGCGGCGGCTCTGGTGGTGGTGGATCC**CAGTCTGCCC TGACTCAGCC**
Link-VL3-For	AGCGGCGGCGGCGGCTCTGGTGGTGGTGGATCC**TCCTMTGAGC TGACWCAG**
Link-VL4ab-For	AGCGGCGGCGGCGGCTCTGGTGGTGGTGGATCC**CAGCYTGTGC TGACTCAATC**
Link-VL4c-For	AGCGGCGGCGGCGGCTCTGGTGGTGGTGGATCC**CTGCCTGTGC TGACTCAGCC**
Link-VL5-For	AGCGGCGGCGGCGGCTCTGGTGGTGGTGGATCC**CAGSCTGTGC TGACYCAGCC**
Link-VL6-For	AGCGGCGGCGGCGGCTCTGGTGGTGGTGGATCC**AATTTTATGCT GACTCAGCCC**
Link-VL7-For	AGCGGCGGCGGCGGCTCTGGTGGTGGTGGATCC**CAGRCTGTGG TGACTCAGGAGCCCTC**

The reverse primers shown in Table 5.11 represent complementary sequences of the stated JL antibody family sequences (bold). They introduce a stop codon and an overlap to the pIgV plasmid.

Table 5.11: Reverse primers introducing a stop codon and an overlap to the pIgV plasmid in the JL family sequences. JL family part is printed in bold.

JL family primer	Sequence 5' → 3'
JL1-3-Vec-Rev	CTGCTCTGCTGCACC**TAGGACGGTSASCTTGGTCCC**
JL7-Vec-Rev	CTGCTCTGCTGCACC**GAGGACGGTCAGCTGGGTGCC**

The reverse primers shown in Table 5.12 represent complementary sequences of the stated JL antibody family sequences (bold). They introduce part of the $(G_4S)_4$ linker sequence.

Table 5.12: Reverse primers introducing part of the $(G_4S)_4$ linker sequence in the JL family sequences. JL family part is printed in bold.

JL family primer	Sequence 5' → 3'
JL1-3-Rev-Link	ACCAGAGCCGCCGCCGCCGCTACCACCACCACC**TAGGACGGTSAS CTTGGTCCC**
JL7-Rev-Link	ACCAGAGCCGCCGCCGCCGCTACCACCACCACC**GAGGACGGTCA GCTGGGTGCC**

5.6.5 Preparation of Input DNA for PACMAN

The preparation of the DNA was done exactly the way it was described in Chapter 4.6.3.

5.6.6 Preparation of agarose gel

The agarose gel was prepared exactly the way it was described in Chapter 4.6.4.

5.6.7 Determination of DNA concentration

The concentration of the DNA was measured the way it was described in Chapter 4.6.5.

5.6.8 Gibson Assembly

The Gibson Assemblies were performed exactly the way described in Chapter 4.6.6.

5.6.9 Purchased Peptide

The IAPP target peptide

bio-3xPEG-5-FAM-KYTTNSGVNTSSLIAGFNNSSLIAGFNNSSHVLFNALRQTACTATNC-Cy5

was purchased by Pepscan.

5.6.10 Coupling of biotinylated DNA and target peptide to the microbeads

The coupling of biotinylated DNA and target peptide to the microbeads was done the way it was described in Chapter 4.6.8.

5.6.11 On-bead emPCR

The on-bead emPCR was performed the way described in Chapter 4.6.9.

5.6.12 IVTT

IVTT was performed the way described in Chapter 4.6.10. For IVTT in solution for HPLC analyses, only 25 µl of IVTT was used in total and the trace metal mix A5 with Co was left out. The IVTT was prepared in a cut 0.5 ml Eppendorf Protein LoBind Tube and the target peptide was added directly at a concentration of 25 µM.

5.6.13 FACS

FACS analysis was performed the way described in Chapter 4.6.11, but only the Beckman Coulter CytoFLEX SRT device was used.

5.6.14 Reamplification of the DNA coupled to the sorted microbeads

Reamplification of the DNA coupled to the sorted microbeads was performed the way described in Chapter 4.6.12.

5.6.15 HPLC analysis

HPLC analyses were performed using a gradient of 0-80% of acetonitrile with 0.1% TFA over 40 min. An Agilent Zorbax SB300 C8, 4.6x250 mm column was used heated to 80 °C. A flow rate of 0.1 ml/min was applied. After the gradient, the column was washed for 2 min with 80% acetonitrile with 0.1% TFA. Re-equilibration was performed for 8 min using water.

5.7 Supplementary Information

A

ATG-V-Stop		ATG-V-Link		Link-V-Stop	
ATG-VH-Stop (65°C)		**ATG-VH-Link (65°C)**		**Link-VH-Stop (65°C)**	
fwd primers:	**rev primers:**	**fwd primers:**	**rev primers:**	**fwd primers:**	**rev primers:**
Vec-SalI-ATG-VH1/7-For	JH1_2_4_5-Vec-Rev	Vec-SalI-ATG-VH1/7-For	JH1_2_4_5-Rev-Link	Link-VH1/7-For	JH1_2_4_5-Vec-Rev
Vec-SalI-ATG-VH1-For	JH3_6-Vec-Rev	Vec-SalI-ATG-VH1-For	JH3_6-Rev-Link	Link-VH1-For	JH3_6-Vec-Rev
Vec-SalI-ATG-VH2-For		Vec-SalI-ATG-VH2-For		Link-VH2-For	
Vec-SalI-ATG-VH3_1-For		Vec-SalI-ATG-VH3_1-For		Link-VH3_1-For	
Vec-SalI-ATG-VH3_2-For		Vec-SalI-ATG-VH3_2-For		Link-VH3_2-For	
Vec-SalI-ATG-VH4_1-For		Vec-SalI-ATG-VH4_1-For		Link-VH4_1-For	
Vec-SalI-ATG-VH4_2-For		Vec-SalI-ATG-VH4_2-For		Link-VH4_2-For	
Vec-SalI-ATG-VH5-For		Vec-SalI-ATG-VH5-For		Link-VH5-For	
Vec-SalI-ATG-VH6-For		Vec-SalI-ATG-VH6-For		Link-VH6-For	
ATG-VL-Stop (60°C)		**ATG-VL-Link (60°C)**		**Link-VL-Stop (60°C)**	
fwd primers:	**rev primers:**	**fwd primers:**	**rev primers:**	**fwd primers:**	**rev primers:**
Vec-SalI-ATG-VL3-For	JL1-3-Vec-Rev	Vec-SalI-ATG-VL3-For	JL1-3-Rev-Link	Link-VL3-For	JL1-3-Vec-Rev
Vec-SalI-ATG-VL4ab-For	JL7-Vec-Rev	Vec-SalI-ATG-VL4ab-For	JL7-Rev-Link	Link-VL4ab-For	JL7-Vec-Rev
Vec-SalI-ATG-VL6-For		Vec-SalI-ATG-VL6-For		Link-VL6-For	
ATG-VL-Stop (65°C)		**ATG-VL-Link (65°C)**		**Link-VL-Stop (65°C)**	
fwd primers:	**rev primers:**	**fwd primers:**	**rev primers:**	**fwd primers:**	**rev primers:**
Vec-SalI-ATG-VL1-For	JL1-3-Vec-Rev	Vec-SalI-ATG-VL1-For	JL1-3-Rev-Link	Vec-SalI-ATG-VL1-For	JL1-3-Vec-Rev
Vec-SalI-ATG-VL2-For	JL7-Vec-Rev	Vec-SalI-ATG-VL2-For	JL7-Rev-Link	Vec-SalI-ATG-VL2-For	JL7-Vec-Rev
Vec-SalI-ATG-VL4c-For		Vec-SalI-ATG-VL4c-For		Vec-SalI-ATG-VL4c-For	
Vec-SalI-ATG-VL5-For		Vec-SalI-ATG-VL5-For		Vec-SalI-ATG-VL5-For	
Vec-SalI-ATG-VL7-For		Vec-SalI-ATG-VL7-For		Vec-SalI-ATG-VL7-For	
ATG-VK-Stop (62°C)		**ATG-VK-Link (62°C)**		**Link-VK-Stop (62°C)**	
fwd primers:	**rev primers:**	**fwd primers:**	**rev primers:**	**fwd primers:**	**rev primers:**
Vec-SalI-ATG-VK1-For	JK1-4-Vec-Rev	Vec-SalI-ATG-VK1-For	JK1-4-Rev-Link	Link-VK1-For	JK1-4-Vec-Rev
Vec-SalI-ATG-VK2-For	JK5-Vec-Rev	Vec-SalI-ATG-VK2-For	JK5-Rev-Link	Link-VK2-For	JK5-Vec-Rev
Vec-SalI-ATG-VK3-For		Vec-SalI-ATG-VK3-For		Link-VK3-For	
Vec-SalI-ATG-VK4-For		Vec-SalI-ATG-VK4-For		Link-VK4-For	
Vec-SalI-ATG-VK5-For		Vec-SalI-ATG-VK5-For		Link-VK5-For	
Vec-SalI-ATG-VK6-For		Vec-SalI-ATG-VK6-For		Link-VK6-For	

B

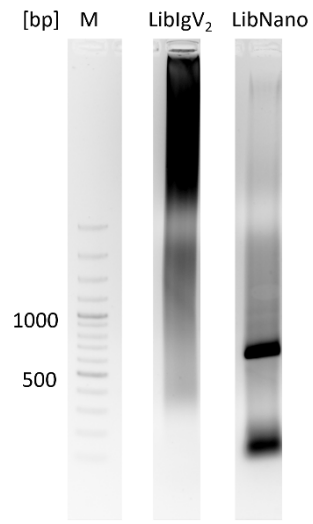

SI Figure 5.1: Primers used for the construction of the antibody libraries and amplification of the DNA from streptavidin coated microbeads. A: Primers used to amplify VH and VL from human derived PBMCs. The primers were designed after evaluation of the V and J region exon nucleotide sequence alignments uploaded to V BASE (326). **B:** Amplification of the DNA from streptavidin coated microbeads.

6 General Discussion and Outlook

The objective of this thesis was to explore basic mechanisms of amyloid aggregation as well as method development to gain access to novel therapeutic strategies. In this thesis, firstly I dealt with basic questions about the amyloid disease associated peptides α-syn and IAPP displayed in Chapters 2 and 3.

As the elongation of α-syn is a process associated with the development of synucleinopathies like PD, our group introduced an inhibitor that blocks the inhibition of the elongation of α-syn. Shaykhalishahi *et al.* (201) described a potent inhibitor of α-syn elongation processes. This inhibitor had the sequence of α-syn but mutations at positions 41 and 48. G41C and V48C resulted in the formation of a disulfide bridge triggering the emergence of a hairpin loop. In 2020, Agerschou *et al.* (202) determined that fusion of the inhibitor which is denoted CC48 C-terminally to a wildtype monomer of α-syn results in increased inhibitory strength. The dimeric design of the construct was based on the fact that the structurally resolved α-syn fibril polymorphs consist of two protofilaments (189, 217, 219, 327). Until now, it was not understood which part or parts of the dimeric construct is responsible for the strong inhibition. To gain insights, we decided to prepare several truncated versions of the dimeric inhibitor WT-CC48. Our finding (Chapter 2) that the HP and NAC region in both monomeric sides of the dimeric construct WT-CC48 are key of inhibition of α-syn fibril elongation helped us to understand the mechanism of the inhibition process. The data strongly suggest that the inhibitor CC48 binds to the fibril end on one of the protofilaments of the fibril polymorph. To the other protofilament there binds the WT α-syn part. The following monomers cannot assemble in the highly ordered fibril elongating manner, but in a less ordered oligomer-like cap which is the endpoint of the elongation of the fibril. The minimal inhibitory construct of WT-CC48 was not tested separately but would be of great interest for upcoming projects. The question whether the inhibitor is only of interest in *in vitro* studies focusing on one mode of amyloid aggregation or could be utilized as a potent therapeutic is still open. A next step in this direction would be to make the construct enter cells. The fusion of different cell-penetrating tags or optimizing transfection techniques would be of importance. Another aspect would be the intracellular stability of the disulfide bridge. To avoid undesirable degradation processes, one could try to synthesize the minimal inhibitory construct of WT-CC48 as a D-peptide to protect it from proteolysis. Another possibility to circumvent the issue of the low stability of the disulfide bridge under reducing environment might be found in utilizing peptide mimetics. The finding that the construct CC49, meaning G41C and V49C, showed a remarkable lower ability to inhibit α-syn fibril elongation illustrates that the chemical neighbourhood of the residues involved in the disulfide bridge is of great importance and that one amino acid more in the hairpin loop makes a difference. This

finding indicates that peptide mimetics might require thorough optimization to overcome the stability issue without loss of inhibitory activity.

The field of research on amyloid diseases is dependent on reliable models of stable oligomers as oligomers are considered to be the toxic species in the progression of amyloid diseases. We introduced a potent model of IAPP oligomers by generation a polypeptide containing two IAPP units. The cysteines in the IAPP units were substituted with serines to prevent undesirable disordered formations of disulfide bridges within the dimeric molecule. The two IAPP units were connected via a flexible glycine-serine linker. As proved by AFM, the appearance of the aggregated species formed by dimIAPP-O differed strikingly from the fibrils IAPP is known to aggregate into rapidly. We used the oligomeric model in *in vitro* as well as *in vivo* studies to gain insights into its characteristics and effects. The *in vitro* ThT assays revealed dimIAPP-O to have delaying impact on the aggregation behaviour of IAPP. DimIAPP-O does not get incorporated into the fibril in the same manner as IAPP does as inferred from the aggregation behaviour in ThT-based kinetic assays. The mechanism of inhibition is not understood at this point. However, dimIAPP-O binds in an unknown way to IAPP and prevents ThT from binding. The *in vivo* data investigating the effects of dimIAPP-O in comparison to IAPP fibrils related to stress mechanisms in the ER and mitochondria revealed more toxicity in case of the treatment with IAPP fibrils. Concerning ER and mitochondria stress markers to be potent indicators, fibrils have a bigger impact on the cells. It is important to note that the choice of the cell line allowed us to observe the effects independently as rat derived RIN-m5f cells do not synthesize aggregation prone IAPP. The effects observed are only caused by the distinct species itself and no seeding effects. Contrary to the Aβ toxicity reducing results by Tomiyama *et al.* (84, 85), Meier *et al.* (248) used rifampicin to prevent IAPP fibril formation which was successful, but were still able to observe toxicity which was caused by IAPP oligomers as detected by oligomer-specific antibodies. Meier *et al.* (248) concluded from their data that the prevention of toxic oligomer formation should be in focus and not of fibril formation. There is the possibility that dimIAPP-O is not the toxic form due to its off-pathway character. It would be of great interest to investigate the effects of dimIAPP-O in a cell line synthesizing human IAPP. In our experiments, neither dimIAPP-O nor IAPP fibrils showed cytotoxic effects on the cells as the CellTiter-Blue® assay (SI Figure 3.3A) did not show a difference between untreated and dimIAPP-O and IAPP fibril treated cells. Under the fluorescence microscope (SI Figure 3.4) no difference concerning viability was observed. It must be emphasized that suffering from amyloid diseases like AD, PD or T2DM comprises a long multifactorial medical history. The diseases do not proceed aggressively, but slowly and steadily. The effects observed here by us are of acute, and not chronic nature. Our findings indicate that either dimIAPP-O is not the critical disease-related aggregation species, the oligomers in studies by

other groups are not stable and form more toxic fibrils, the experimental setup does not correspond at all to the disease-relevant mechanism or other processes are responsible for the cytotoxicity of the β-cells of the islets of Langerhans. The assumption that oligomers and not fibrils might be the toxic species in all amyloid diseases developed from the observation of neuro- or cytotoxicity, but absence of well-defined, easy to find plaques. This is reasonable but cannot be confirmed with the findings shown in Chapter 3.

The ultimate goal is the maintenance of monomeric species of all amyloidogenic peptides and proteins. As displayed in Chapter 3, the deposition of fibrils or plaques triggers stress responses and is therefore no favourable state. This is a goal which could be achieved by the utilization of proteolytic antibodies. Passive immunization by utilizing antibodies is favoured compared to active immunization by developing vaccines as a big issue of the development of vaccines is the choice of the target. Monomeric species of amyloidogenic proteins and peptides cannot be used as a target because of their vital roles. The idea of injecting the right dose of a vaccine triggering the immune response against monomers would be a mammoth project and not feasible at all. The injection of preformed fibrils would be dangerous due to possible contagion of amyloid diseases. Administering external antibodies is less dangerous and a better practicable opportunity.

The idea of naturally occurring proteolytic antibodies was introduced by Paul et al. (315) in 1998. Paul's group claims IgM antibodies and single-chain antibodies to exhibit proteolytic properties. This made us believe in the potential of proteolytic antibodies as novel therapeutics. They would have many advantages compared to conventional antibody therapy which recruits the immune response of the patient risking micro bleedings and inflammation. They would be capable of not only recognizing their target but executing their cleavage reaction on site. Taguchi *et al.* (316) and Paul *et al.* (317) reported the fragments to be aggregation-incompetent which would be the perfect basis for curing amyloid diseases, of course while at the same time improving cognitive abilities. The group itself mentioned the danger of false-positive results caused by contamination (328) when isolating IgM antibodies from human blood donations. The Paul group performed an experiment in which 6 M GdmCl was added to the PBS in an SEC run in order to get rid of potentially bound proteases to the IgM antibodies. After refolding of the IgM, they were able to detect the same cleavage pattern against Aβ which they observed before. We replicated the experiment and were able to observe the same pattern in agreement with published data from the Paul group (data not included in this thesis). As proteases bound to IgM antibodies and separated by GdmCl treatment might have the same size as IgM antibodies or at least might show a similar elution pattern on a gel filtration column, we are less

confident about the success of this purification step. Therefore, we are less optimistic than the Paul group.

Another point we struggled with was the reproducibility of catalytic activity of two single-chain antibody derivatives the Paul group (329) introduced, denoted 2E6 and 5D3. We were able to express and purify the antibodies produced in the periplasm of *E. coli* BL21(DE3) successfully. Furthermore, 2E6 and 5D3 were expressed and synthesized in IVTT solutions with added supplements like chaperones, chaperonins, and trace metal mixes, but no functionality was observed in this attempt. Alterations in expression duration and temperature did not lead to functional antibody derivatives. The self-selected antibody derivatives from human blood donations against IAPP allowed for hope in the first experiment as an additional peak, shown in Chapter 5, appeared. Unfortunately, the peak was also observed in the control sample.

When I transformed competent *E. coli* XL1-Blue cells with my nanobody library DNA output from the PACMAN rounds, I only received in 20% of the clones a real nanobody. In general, transformation efficiency was poor and cloning efficiency is something which could be improved. With the single nanobody I received I was not able to reproduce the result I observed for the pool of DNA. Because it was only one isolated known nanobody which was not a potent one, I would not overinterpret the result and claim that there are no proteolytic antibodies. However, at the current stage of research, we cannot be sure that proteolytic antibodies really exist. It would need more studies to prove their existence.

We established the PACMAN method which is shown in Chapter 4 in order to select proteolytic antibodies against amyloid targets to open a novel approach for therapy development. PACMAN is an easily applicable method which exhibits its potency by the fact that only two rounds of PACMAN are sufficient to eradicate non-desired DNA. The aim that motivated us to work on method establishment has not been successful so far. I only focused on the nanobody library we built but did not use the LibIgV$_2$ library as we still had issues in reamplifying the DNA from that library. Another attempt would be to search in the LibIgV$_2$ library for potent proteolytic antibodies albeit my colleague Filip Hasecke used both libraries and could not identify any potent antibody derivatives against Aβ.
The PACMAN method nevertheless is a promising way to select proteases from different sources which allows trustworthy selection of proteases with special properties while only requiring widely distributed equipment.

7 Author Contributions

The following manuscripts and projects reflect the content of this dissertation.

Chapter 2:

Celina M. Schulz*, Anne Pfitzer*, Wolfgang Hoyer

*: These authors contributed equally.

Fibril core regions in engineered α-synuclein dimer are crucial for blocking of fibril elongation

Contributions: Design of constructs, transformation, expression, purification, elongation assays, DGC experiments, SDS-PAGE, preparation of figures, writing and reviewing of the manuscript

Chapter 3:

Anne Pfitzer*, Celina M. Schulz*, Robin Backer, Filip Hasecke, Wolfgang Hoyer

*: These authors contributed equally.

An islet amyloid polypeptide oligomer model for the study of amyloid aggregation and oligomer induced pathophysiology

Contributions: Study design, design of the construct, transformation, expression, purification, AFM, *de novo* aggregation assays, RNA isolation, cDNA synthesis, primer design, qPCR, evaluation of qPCR, preparation of figures, writing and reviewing of the manuscript

Chapter 4:

Filip Hasecke*, Anne Pfitzer*, Nadine Teichweyde, Charlotte Esser, Wolfgang Hoyer

*: These authors contributed equally.

PACMAN: A High-Throughput Method for Selecting Proteases with Special Properties

Contributions: Attract third-party funding, ordering of the peptide, DNA preparation, cloning, optimization of emPCR, optimization of emulsion compositions, TIRF microscopy, IVTT reactions, FACS analyses, writing and reviewing of the manuscript

Chapter 5:

Anne Pfitzer, Filip Hasecke, Stefanie Williams, Robin Backer, Wolfgang Hoyer

PACMAN selection against Islet Amyloid Polypeptide

Contributions: Study design, ordering of the peptide, supervision of Stefanie Williams who optimized conditions for the establishment of antibody libraries, cloning, PACMAN runs, IVTT reactions, FACS analyses, writing and reviewing of the manuscript

8 References

1. R. Virchow, Zur Cellulose —Frage. *Archiv für pathologische Anatomie und Physiologie und für klinische Medicin* **6**, 416-426 (1854).
2. N. Friedreich, A. Kekulé, Zur Amyloidfrage. *Archiv für pathologische Anatomie und Physiologie und für klinische Medicin* **16**, 50-65 (1859).
3. E. D. Eanes, G. G. Glenner, X-ray diffraction studies on amyloid filaments. *J Histochem Cytochem* **16**, 673-677 (1968).
4. A. Geddes, K. Parker, E. Atkins, E. Beighton, “Cross-β” conformation in proteins. *Journal of molecular biology* **32**, 343-358 (1968).
5. M. G. Iadanza, M. P. Jackson, E. W. Hewitt, N. A. Ranson, S. E. Radford, A new era for understanding amyloid structures and disease. *Nature Reviews Molecular Cell Biology* **19**, 755-773 (2018).
6. R. Tycko, Solid-state NMR studies of amyloid fibril structure. *Annu Rev Phys Chem* **62**, 279-299 (2011).
7. O. S. Makin, E. Atkins, P. Sikorski, J. Johansson, L. C. Serpell, Molecular basis for amyloid fibril formation and stability. *Proc Natl Acad Sci U S A* **102**, 315-320 (2005).
8. M. Török *et al.*, Structural and dynamic features of Alzheimer's Abeta peptide in amyloid fibrils studied by site-directed spin labeling. *J Biol Chem* **277**, 40810-40815 (2002).
9. M. Schmidt *et al.*, Comparison of Alzheimer Abeta(1-40) and Abeta(1-42) amyloid fibrils reveals similar protofilament structures. *Proc Natl Acad Sci U S A* **106**, 19813-19818 (2009).
10. A. D. Williams *et al.*, Mapping abeta amyloid fibril secondary structure using scanning proline mutagenesis. *J Mol Biol* **335**, 833-842 (2004).
11. R. Nelson *et al.*, Structure of the cross-beta spine of amyloid-like fibrils. *Nature* **435**, 773-778 (2005).
12. D. Eisenberg, M. Jucker, The amyloid state of proteins in human diseases. *Cell* **148**, 1188-1203 (2012).
13. J. D. Sipe *et al.*, Amyloid fibril protein nomenclature: 2010 recommendations from the nomenclature committee of the International Society of Amyloidosis. *Amyloid* **17**, 101-104 (2010).
14. M. D. Benson *et al.*, Amyloid nomenclature 2018: recommendations by the International Society of Amyloidosis (ISA) nomenclature committee. *Amyloid* **25**, 215-219 (2018).
15. J. N. Buxbaum *et al.*, Amyloid nomenclature 2022: update, novel proteins, and recommendations by the International Society of Amyloidosis (ISA) Nomenclature Committee. *Amyloid* **29**, 213-219 (2022).
16. J.-P. Colletier *et al.*, Molecular basis for amyloid-β polymorphism. *Proceedings of the National Academy of Sciences* **108**, 16938-16943 (2011).
17. W. Qiang, K. Kelley, R. Tycko, Polymorph-Specific Kinetics and Thermodynamics of β-Amyloid Fibril Growth. *Journal of the American Chemical Society* **135**, 6860-6871 (2013).
18. J. Gath *et al.*, Yet another polymorph of α-synuclein: solid-state sequential assignments. *Biomol NMR Assign* **8**, 395-404 (2014).
19. C. B. Anfinsen, Principles that govern the folding of protein chains. *Science* **181**, 223-230 (1973).
20. A. Sicorello *et al.*, Agitation and high ionic strength induce amyloidogenesis of a folded PDZ domain in native conditions. *Biophys J* **96**, 2289-2298 (2009).
21. H. LeVine, 3rd, Thioflavine T interaction with synthetic Alzheimer's disease beta-amyloid peptides: detection of amyloid aggregation in solution. *Protein Sci* **2**, 404-410 (1993).
22. F. Chiti *et al.*, Designing conditions for in vitro formation of amyloid protofilaments and fibrils. *Proc Natl Acad Sci U S A* **96**, 3590-3594 (1999).

23. L. Wang, S. K. Maji, M. R. Sawaya, D. Eisenberg, R. Riek, Bacterial inclusion bodies contain amyloid-like structure. *PLoS Biol* **6**, e195 (2008).
24. W. E. Balch, R. I. Morimoto, A. Dillin, J. W. Kelly, Adapting proteostasis for disease intervention. *Science* **319**, 916-919 (2008).
25. D. Romero, C. Aguilar, R. Losick, R. Kolter, Amyloid fibers provide structural integrity to Bacillus subtilis biofilms. *Proceedings of the National Academy of Sciences* **107**, 2230-2234 (2010).
26. A. Taglialegna *et al.*, Staphylococcal Bap proteins build amyloid scaffold biofilm matrices in response to environmental signals. *PLoS pathogens* **12**, e1005711 (2016).
27. D. M. Fowler *et al.*, Functional amyloid formation within mammalian tissue. *PLoS biology* **4**, e6 (2006).
28. N. R. Roan *et al.*, Peptides released by physiological cleavage of semen coagulum proteins form amyloids that enhance HIV infection. *Cell host & microbe* **10**, 541-550 (2011).
29. M. Stefani, C. M. Dobson, Protein aggregation and aggregate toxicity: new insights into protein folding, misfolding diseases and biological evolution. *J Mol Med (Berl)* **81**, 678-699 (2003).
30. S. E. Radford, C. M. Dobson, From computer simulations to human disease: emerging themes in protein folding. *Cell* **97**, 291-298 (1999).
31. J. W. Kelly, The alternative conformations of amyloidogenic proteins and their multi-step assembly pathways. *Current opinion in structural biology* **8**, 101-106 (1998).
32. C. M. Dobson, The structural basis of protein folding and its links with human disease. *Philosophical Transactions of the Royal Society of London. Series B: Biological Sciences* **356**, 133-145 (2001).
33. L. Bousset *et al.*, Structural and functional characterization of two alpha-synuclein strains. *Nature Communications* **4**, 2575 (2013).
34. H. Olzscha *et al.*, Amyloid-like aggregates sequester numerous metastable proteins with essential cellular functions. *Cell* **144**, 67-78 (2011).
35. R. Kayed *et al.*, Common structure of soluble amyloid oligomers implies common mechanism of pathogenesis. *Science* **300**, 486-489 (2003).
36. C. Haass, D. J. Selkoe, Soluble protein oligomers in neurodegeneration: lessons from the Alzheimer's amyloid β-peptide. *Nature reviews Molecular cell biology* **8**, 101-112 (2007).
37. K. Sörgjerd, T. Klingstedt, M. Lindgren, K. Kågedal, P. Hammarström, Prefibrillar transthyretin oligomers and cold stored native tetrameric transthyretin are cytotoxic in cell culture. *Biochemical and biophysical research communications* **377**, 1072-1078 (2008).
38. J. Lee, E. K. Culyba, E. T. Powers, J. W. Kelly, Amyloid-β forms fibrils by nucleated conformational conversion of oligomers. *Nat Chem Biol* **7**, 602-609 (2011).
39. F. Ferrone, Analysis of protein aggregation kinetics. *Methods Enzymol* **309**, 256-274 (1999).
40. C. G. Glabe, R. Kayed, Common structure and toxic function of amyloid oligomers implies a common mechanism of pathogenesis. *Neurology* **66**, S74-S78 (2006).
41. I. V. Baskakov, G. Legname, M. A. Baldwin, S. B. Prusiner, F. E. Cohen, Pathway complexity of prion protein assembly into amyloid. *J Biol Chem* **277**, 21140-21148 (2002).
42. P. J. Muchowski, J. L. Wacker, Modulation of neurodegeneration by molecular chaperones. *Nat Rev Neurosci* **6**, 11-22 (2005).
43. D. E. Ehrnhoefer *et al.*, EGCG redirects amyloidogenic polypeptides into unstructured, off-pathway oligomers. *Nat Struct Mol Biol* **15**, 558-566 (2008).
44. F. Bemporad, F. Chiti, Protein misfolded oligomers: experimental approaches, mechanism of formation, and structure-toxicity relationships. *Chem Biol* **19**, 315-327 (2012).
45. S. Lesné *et al.*, A specific amyloid-beta protein assembly in the brain impairs memory. *Nature* **440**, 352-357 (2006).

46. G. M. Shankar *et al.*, Amyloid-beta protein dimers isolated directly from Alzheimer's brains impair synaptic plasticity and memory. *Nat Med* **14**, 837-842 (2008).
47. B. Winner *et al.*, In vivo demonstration that alpha-synuclein oligomers are toxic. *Proc Natl Acad Sci U S A* **108**, 4194-4199 (2011).
48. Z. Berger *et al.*, Accumulation of pathological tau species and memory loss in a conditional model of tauopathy. *J Neurosci* **27**, 3650-3662 (2007).
49. B. R. Hoover *et al.*, Tau mislocalization to dendritic spines mediates synaptic dysfunction independently of neurodegeneration. *Neuron* **68**, 1067-1081 (2010).
50. M. H. Polymeropoulos *et al.*, Mutation in the alpha-Synuclein Gene Identified in Families with Parkinson's Disease. *Science* **276**, 2045-2047 (1997).
51. J. J. Zarranz *et al.*, The new mutation, E46K, of α-synuclein causes parkinson and Lewy body dementia. *Annals of Neurology* **55**, 164-173 (2004).
52. M. Yoshida, Multiple system atrophy: α-synuclein and neuronal degeneration. *Neuropathology* **27**, 484-493 (2007).
53. E. A. Coon, W. Singer, Synucleinopathies. *Continuum (Minneapolis, Minn.)* **26**, 72 (2020).
54. M. G. Cersosimo, E. E. Benarroch, Central control of autonomic function and involvement in neurodegenerative disorders. *Handb Clin Neurol* **117**, 45-57 (2013).
55. C. H. Schenck, A. L. Callies, M. W. Mahowald, Increased percentage of slow-wave sleep in REM sleep behavior disorder (RBD): a reanalysis of previously published data from a controlled study of RBD reported in SLEEP. *Sleep* **26**, 1066; author reply 1067 (2003).
56. B. F. Boeve *et al.*, Synucleinopathy pathology and REM sleep behavior disorder plus dementia or parkinsonism. *Neurology* **61**, 40-45 (2003).
57. A. Iwai *et al.*, The precursor protein of non-A beta component of Alzheimer's disease amyloid is a presynaptic protein of the central nervous system. *Neuron* **14**, 467-475 (1995).
58. P. H. Jensen, M. S. Nielsen, R. Jakes, C. G. Dotti, M. Goedert, Binding of alpha-synuclein to brain vesicles is abolished by familial Parkinson's disease mutation. *J Biol Chem* **273**, 26292-26294 (1998).
59. J. M. George, H. Jin, W. S. Woods, D. F. Clayton, Characterization of a novel protein regulated during the critical period for song learning in the zebra finch. *Neuron* **15**, 361-372 (1995).
60. K. Petersen, O. F. Olesen, J. D. Mikkelsen, Developmental expression of alpha-synuclein in rat hippocampus and cerebral cortex. *Neuroscience* **91**, 651-659 (1999).
61. N. G. Kholodilov *et al.*, Increased expression of rat synuclein in the substantia nigra pars compacta identified by mRNA differential display in a model of developmental target injury. *J Neurochem* **73**, 2586-2599 (1999).
62. G. S. Withers, J. M. George, G. A. Banker, D. F. Clayton, Delayed localization of synelfin (synuclein, NACP) to presynaptic terminals in cultured rat hippocampal neurons. *Brain Res Dev Brain Res* **99**, 87-94 (1997).
63. R. G. Perez *et al.*, A role for alpha-synuclein in the regulation of dopamine biosynthesis. *J Neurosci* **22**, 3090-3099 (2002).
64. S. E. Kahn, M. E. Cooper, S. Del Prato, Pathophysiology and treatment of type 2 diabetes: perspectives on the past, present, and future. *The Lancet* **383**, 1068-1083 (2014).
65. N. Kang *et al.*, Adverse associations of different obesity measures and the interactions with long-term exposure to air pollutants with prevalent type 2 diabetes mellitus: The Henan Rural Cohort study. *Environ Res* **207**, 112640 (2022).
66. P. Saeedi *et al.*, Global and regional diabetes prevalence estimates for 2019 and projections for 2030 and 2045: Results from the International Diabetes Federation Diabetes Atlas, 9(th) edition. *Diabetes Res Clin Pract* **157**, 107843 (2019).
67. L. Guariguata *et al.*, Global estimates of diabetes prevalence for 2013 and projections for 2035. *Diabetes Res Clin Pract* **103**, 137-149 (2014).
68. Z. Zhou, B. Sun, D. Yu, C. Zhu, Gut microbiota: an important player in type 2 diabetes mellitus. *Frontiers in Cellular and Infection Microbiology* **12**, 112 (2022).

69. G. J. Taborsky Jr, The physiology of glucagon. *Journal of diabetes science and technology* **4**, 1338-1344 (2010).
70. P. Westermark, A. Andersson, G. T. Westermark, Islet amyloid polypeptide, islet amyloid, and diabetes mellitus. *Physiol Rev* **91**, 795-826 (2011).
71. T. A. Lutz, The role of amylin in the control of energy homeostasis. *Am J Physiol Regul Integr Comp Physiol* **298**, R1475-1484 (2010).
72. J. Montane, A. Klimek-Abercrombie, K. J. Potter, C. Westwell-Roper, C. Bruce Verchere, Metabolic stress, IAPP and islet amyloid. *Diabetes Obes Metab* **14 Suppl 3**, 68-77 (2012).
73. M. Kawahara, Y. Kuroda, N. Arispe, E. Rojas, Alzheimer's beta-amyloid, human islet amylin, and prion protein fragment evoke intracellular free calcium elevations by a common mechanism in a hypothalamic GnRH neuronal cell line. *J Biol Chem* **275**, 14077-14083 (2000).
74. A. Clark *et al.*, Islet amyloid, increased A-cells, reduced B-cells and exocrine fibrosis: quantitative changes in the pancreas in type 2 diabetes. *Diabetes Res* **9**, 151-159 (1988).
75. P. Westermark, L. Grimelius, The pancreatic islet cells in insular amyloidosis in human diabetic and non-diabetic adults. *Acta Pathol Microbiol Scand A* **81**, 291-300 (1973).
76. P. Westermark, E. Wilander, The influence of amyloid deposits on the islet volume in maturity onset diabetes mellitus. *Diabetologia* **15**, 417-421 (1978).
77. D. Gu, K. Andreev, M. E. Dupre, Major Trends in Population Growth Around the World. *China CDC Wkly* **3**, 604-613 (2021).
78. J. Li, X. Han, X. Zhang, S. Wang, Spatiotemporal evolution of global population ageing from 1960 to 2017. *BMC public health* **19**, 1-15 (2019).
79. Bundesministerium für Bildung und Forschung, Wie funktionieren klinische Studien? (2023).
80. M. Necula, R. Kayed, S. Milton, C. G. Glabe, Small molecule inhibitors of aggregation indicate that amyloid beta oligomerization and fibrillization pathways are independent and distinct. *J Biol Chem* **282**, 10311-10324 (2007).
81. J. Wang, S. Gines, M. E. MacDonald, J. F. Gusella, Reversal of a full-length mutant huntingtin neuronal cell phenotype by chemical inhibitors of polyglutamine-mediated aggregation. *BMC Neuroscience* **6**, 1 (2005).
82. Y. Porat, Y. Mazor, S. Efrat, E. Gazit, Inhibition of islet amyloid polypeptide fibril formation: a potential role for heteroaromatic interactions. *Biochemistry* **43**, 14454-14462 (2004).
83. T. Umeda *et al.*, Rifampicin is a candidate preventive medicine against amyloid-β and tau oligomers. *Brain* **139**, 1568-1586 (2016).
84. T. Tomiyama *et al.*, Rifampicin prevents the aggregation and neurotoxicity of amyloid beta protein in vitro. *Biochem Biophys Res Commun* **204**, 76-83 (1994).
85. T. Tomiyama *et al.*, Inhibition of amyloid beta protein aggregation and neurotoxicity by rifampicin. Its possible function as a hydroxyl radical scavenger. *J Biol Chem* **271**, 6839-6844 (1996).
86. J. Li, M. Zhu, S. Rajamani, V. N. Uversky, A. L. Fink, Rifampicin inhibits alpha-synuclein fibrillation and disaggregates fibrils. *Chem Biol* **11**, 1513-1521 (2004).
87. J. Xu *et al.*, Rifampicin protects PC12 cells against MPP+-induced apoptosis and inhibits the expression of an alpha-Synuclein multimer. *Brain Res* **1139**, 220-225 (2007).
88. D. W. Molloy, T. I. Standish, Q. Zhou, G. Guyatt, A multicenter, blinded, randomized, factorial controlled trial of doxycycline and rifampin for treatment of Alzheimer's disease: the DARAD trial. *Int J Geriatr Psychiatry* **28**, 463-470 (2013).
89. B. De Strooper *et al.*, Deficiency of presenilin-1 inhibits the normal cleavage of amyloid precursor protein. *Nature* **391**, 387-390 (1998).
90. R. S. Doody *et al.*, A phase 3 trial of semagacestat for treatment of Alzheimer's disease. *N Engl J Med* **369**, 341-350 (2013).

91. M. F. Egan *et al.*, Randomized Trial of Verubecestat for Mild-to-Moderate Alzheimer's Disease. *N Engl J Med* **378**, 1691-1703 (2018).
92. F. Panza, M. Lozupone, G. Logroscino, B. P. Imbimbo, A critical appraisal of amyloid-β-targeting therapies for Alzheimer disease. *Nature Reviews Neurology* **15**, 73-88 (2019).
93. B. P. Imbimbo, S. Ippati, M. Watling, C. Imbimbo, Role of monomeric amyloid-β in cognitive performance in Alzheimer's disease: Insights from clinical trials with secretase inhibitors and monoclonal antibodies. *Pharmacol Res* **187**, 106631 (2023).
94. G. F. Chen *et al.*, Amyloid beta: structure, biology and structure-based therapeutic development. *Acta Pharmacol Sin* **38**, 1205-1235 (2017).
95. A. J. Espay, A. Sturchio, L. S. Schneider, K. Ezzat, Soluble Amyloid-β Consumption in Alzheimer's Disease. *J Alzheimers Dis* **82**, 1403-1415 (2021).
96. O. Olubiyi *et al.*, Amyloid aggregation inhibitory mechanism of arginine-rich D-peptides. *Current medicinal chemistry* **21**, 1448-1457 (2014).
97. T. van Groen *et al.*, The Aβ oligomer eliminating D-enantiomeric peptide RD2 improves cognition without changing plaque pathology. *Scientific reports* **7**, 16275 (2017).
98. S. Schemmert *et al.*, Aβ Oligomer Elimination Restores Cognition in Transgenic Alzheimer's Mice with Full-blown Pathology. *Mol Neurobiol* **56**, 2211-2223 (2019).
99. O. Brener *et al.*, QIAD assay for quantitating a compound's efficacy in elimination of toxic Aβ oligomers. *Sci Rep* **5**, 13222 (2015).
100. T. Zhang, I. Gering, J. Kutzsche, L. Nagel-Steger, D. Willbold, Toward the Mode of Action of the Clinical Stage All-d-Enantiomeric Peptide RD2 on Aβ42 Aggregation. *ACS Chem Neurosci* **10**, 4800-4809 (2019).
101. J. Kutzsche *et al.*, Large-Scale Oral Treatment Study with the Four Most Promising D3-Derivatives for the Treatment of Alzheimer's Disease. *Molecules* **22** (2017).
102. Priavoid GmbH, https://priavoid.com/pipeline/, last accessed 16.08.2023
103. J. Cummings, G. Lee, A. Ritter, K. Zhong, Alzheimer's disease drug development pipeline: 2018. *Alzheimer's & Dementia: Translational Research & Clinical Interventions* **4**, 195-214 (2018).
104. P. Davies, A. J. Maloney, Selective loss of central cholinergic neurons in Alzheimer's disease. *Lancet* **2**, 1403 (1976).
105. C. Courtney *et al.*, Long-term donepezil treatment in 565 patients with Alzheimer's disease (AD2000): randomised double-blind trial. *Lancet* **363**, 2105-2115 (2004).
106. R. C. Petersen *et al.*, Vitamin E and donepezil for the treatment of mild cognitive impairment. *N Engl J Med* **352**, 2379-2388 (2005).
107. J. S. Birks, J. Grimley Evans, Rivastigmine for Alzheimer's disease. *Cochrane Database Syst Rev* 10.1002/14651858.CD001191.pub3, Cd001191 (2015).
108. R. McShane *et al.*, Memantine for dementia. *Cochrane Database Syst Rev* **3**, Cd003154 (2019).
109. J. Birks, J. Grimley Evans, Ginkgo biloba for cognitive impairment and dementia. *Cochrane Database Syst Rev* 10.1002/14651858.CD003120.pub3, Cd003120 (2009).
110. A. R. Bilia, M. D. C. Costa, Medicinal plants and their preparations in the European market: Why has the harmonization failed? The cases of St. John's wort, valerian, ginkgo, ginseng, and green tea. *Phytomedicine* **81**, 153421 (2021).
111. B. Winblad, Piracetam: a review of pharmacological properties and clinical uses. *CNS Drug Rev* **11**, 169-182 (2005).
112. L. Flicker, G. Grimley Evans, Piracetam for dementia or cognitive impairment. *Cochrane Database Syst Rev* 10.1002/14651858.Cd001011, Cd001011 (2001).
113. H. Fukui, A. Arai, K. Toyoshima, Efficacy of music therapy in treatment for the patients with Alzheimer’s disease. *International Journal of Alzheimer’s disease* **2012** (2012).
114. A. De la Rosa *et al.*, Physical exercise in the prevention and treatment of Alzheimer's disease. *Journal of sport and health science* **9**, 394-404 (2020).

115. M. J. Armstrong, M. S. Okun, Diagnosis and Treatment of Parkinson Disease: A Review. *Jama* **323**, 548-560 (2020).
116. A. J. Espay, A. E. Lang, Common Myths in the Use of Levodopa in Parkinson Disease: When Clinical Trials Misinform Clinical Practice. *JAMA Neurol* **74**, 633-634 (2017).
117. P. J. Garcia-Ruiz *et al.*, Impulse control disorder in patients with Parkinson's disease under dopamine agonist therapy: a multicentre study. *J Neurol Neurosurg Psychiatry* **85**, 840-844 (2014).
118. C. A. Rabinak, M. J. Nirenberg, Dopamine agonist withdrawal syndrome in Parkinson disease. *Arch Neurol* **67**, 58-63 (2010).
119. M. K. Mak, I. S. Wong-Yu, X. Shen, C. L. Chung, Long-term effects of exercise and physical therapy in people with Parkinson disease. *Nat Rev Neurol* **13**, 689-703 (2017).
120. J. Mehrholz *et al.*, Treadmill training for patients with Parkinson Disease. An abridged version of a Cochrane Review. *Eur J Phys Rehabil Med* **52**, 704-713 (2016).
121. Y. Yang, X. Y. Li, L. Gong, Y. L. Zhu, Y. L. Hao, Tai Chi for improvement of motor function, balance and gait in Parkinson's disease: a systematic review and meta-analysis. *PLoS One* **9**, e102942 (2014).
122. P. Krack, J. Volkmann, G. Tinkhauser, G. Deuschl, Deep brain stimulation in movement disorders: from experimental surgery to evidence-based therapy. *Movement Disorders* **34**, 1795-1810 (2019).
123. Y. Liu *et al.*, Improvement of Deep Brain Stimulation in Dyskinesia in Parkinson's Disease: A Meta-Analysis. *Frontiers in Neurology* **10** (2019).
124. N. T. Nguyen, X. M. Nguyen, J. Lane, P. Wang, Relationship between obesity and diabetes in a US adult population: findings from the National Health and Nutrition Examination Survey, 1999-2006. *Obes Surg* **21**, 351-355 (2011).
125. J. J. Marín-Peñalver, I. Martín-Timón, C. Sevillano-Collantes, F. J. Del Cañizo-Gómez, Update on the treatment of type 2 diabetes mellitus. *World J Diabetes* **7**, 354-395 (2016).
126. M. L. Wheeler *et al.*, Macronutrients, food groups, and eating patterns in the management of diabetes: a systematic review of the literature, 2010. *Diabetes Care* **35**, 434-445 (2012).
127. National Diabetes Education Program: Guiding principles for the care of peple with or at risk for diabetes, https://www.niddk.nih.gov/, last accessed on 27.08.2023
128. A. B. Evert *et al.*, Nutrition therapy recommendations for the management of adults with diabetes. *Diabetes Care* **37 Suppl 1**, S120-143 (2014).
129. K. N. Burger *et al.*, Dietary fiber, carbohydrate quality and quantity, and mortality risk of individuals with diabetes mellitus. (2012).
130. A. F. Pfeiffer *et al.*, The effects of different quantities and qualities of protein intake in people with diabetes mellitus. *Nutrients* **12**, 365 (2020).
131. M. Z. Vitolins *et al.*, Action for Health in Diabetes (Look AHEAD) trial: baseline evaluation of selected nutrients and food group intake. *Journal of the American Dietetic Association* **109**, 1367-1375 (2009).
132. M. Cullmann, A. Hilding, C. G. Östenson, Alcohol consumption and risk of pre-diabetes and type 2 diabetes development in a Swedish population. *Diabetic Medicine* **29**, 441-452 (2012).
133. B. E. Karlström, A. E. Järvi, L. Byberg, L. G. Berglund, B. O. Vessby, Fatty fish in the diet of patients with type 2 diabetes: comparison of the metabolic effects of foods rich in n-3 and n-6 fatty acids. *Am J Clin Nutr* **94**, 26-33 (2011).
134. Standards of Medical Care in Diabetes—2016: Summary of Revisions, *Diabetes Care* **39**, S4-S5 (2015).
135. L. J. Goodyear, B. B. Kahn, Exercise, glucose transport, and insulin sensitivity. *Annual review of medicine* **49**, 235-261 (1998).
136. E. Phielix, R. Meex, E. Moonen-Kornips, M. K. Hesselink, P. Schrauwen, Exercise training increases mitochondrial content and ex vivo mitochondrial function similarly in

patients with type 2 diabetes and in control individuals. *Diabetologia* **53**, 1714-1721 (2010).
137. S. Balducci *et al.*, Exercise training can modify the natural history of diabetic peripheral neuropathy. *J Diabetes Complications* **20**, 216-223 (2006).
138. F. P. Cappuccio, D. Cooper, L. D'Elia, P. Strazzullo, M. A. Miller, Sleep duration predicts cardiovascular outcomes: a systematic review and meta-analysis of prospective studies. *Eur Heart J* **32**, 1484-1492 (2011).
139. H. An, L. He, Current understanding of metformin effect on the control of hyperglycemia in diabetes. *J Endocrinol* **228**, R97-106 (2016).
140. R. Song, Mechanism of Metformin: A Tale of Two Sites. *Diabetes Care* **39**, 187-189 (2016).
141. J. Bryan, A. Crane, W. H. Vila-Carriles, A. P. Babenko, L. Aguilar-Bryan, Insulin secretagogues, sulfonylurea receptors and K(ATP) channels. *Curr Pharm Des* **11**, 2699-2716 (2005).
142. A. Takahashi *et al.*, Sulfonylurea and glinide reduce insulin content, functional expression of K(ATP) channels, and accelerate apoptotic beta-cell death in the chronic phase. *Diabetes Res Clin Pract* **77**, 343-350 (2007).
143. K. Maedler *et al.*, Sulfonylurea induced beta-cell apoptosis in cultured human islets. *J Clin Endocrinol Metab* **90**, 501-506 (2005).
144. M. A. Nauck *et al.*, Incretin effects of increasing glucose loads in man calculated from venous insulin and C-peptide responses. *J Clin Endocrinol Metab* **63**, 492-498 (1986).
145. D. R. Owens, G. Matfin, L. Monnier, Basal insulin analogues in the management of diabetes mellitus: What progress have we made? *Diabetes Metab Res Rev* **30**, 104-119 (2014).
146. F. Panza, M. Lozupone, D. Seripa, B. P. Imbimbo, Amyloid-β immunotherapy for alzheimer disease: Is it now a long shot? *Ann Neurol* **85**, 303-315 (2019).
147. Y. H. Liu, B. Giunta, H. D. Zhou, J. Tan, Y. J. Wang, Immunotherapy for Alzheimer disease: the challenge of adverse effects. *Nat Rev Neurol* **8**, 465-469 (2012).
148. C. H. van Dyck, Anti-Amyloid-β Monoclonal Antibodies for Alzheimer's Disease: Pitfalls and Promise. *Biol Psychiatry* **83**, 311-319 (2018).
149. D. Schenk *et al.*, Immunization with amyloid-beta attenuates Alzheimer-disease-like pathology in the PDAPP mouse. *Nature* **400**, 173-177 (1999).
150. S. Gilman *et al.*, Clinical effects of Abeta immunization (AN1792) in patients with AD in an interrupted trial. *Neurology* **64**, 1553-1562 (2005).
151. Clinicaltrials.gov (2021) A Study of CAD106 and CNP520 Versus Placebo in Participants at Risk for the Onset of Clinical Symptoms of Alzheimer's Disease (GS1).
152. A. Schneeberger, M. Mandler, F. Mattner, W. Schmidt, Vaccination for Parkinson's disease. *Parkinsonism & related disorders* **18**, S11-S13 (2012).
153. S. M. Fleming, A. Davis, E. Simons, Targeting alpha-synuclein via the immune system in Parkinson's disease: Current vaccine therapies. *Neuropharmacology* **202**, 108870 (2022).
154. D. Volc *et al.*, Safety and immunogenicity of the α-synuclein active immunotherapeutic PD01A in patients with Parkinson's disease: a randomised, single-blinded, phase 1 trial. *Lancet Neurol* **19**, 591-600 (2020).
155. W. Poewe *et al.*, Safety and Tolerability of Active Immunotherapy Targeting α-Synuclein with PD03A in Patients with Early Parkinson's Disease: A Randomized, Placebo-Controlled, Phase 1 Study. *J Parkinsons Dis* **11**, 1079-1089 (2021).
156. E. S. Roesti *et al.*, Vaccination against amyloidogenic aggregates in pancreatic islets prevents development of type 2 diabetes mellitus. *Vaccines* **8**, 116 (2020).
157. R. Orlandi, D. H. Güssow, P. T. Jones, G. Winter, Cloning immunoglobulin variable domains for expression by the polymerase chain reaction. *Proc Natl Acad Sci U S A* **86**, 3833-3837 (1989).
158. L. Sastry *et al.*, Cloning of the immunological repertoire in Escherichia coli for generation of monoclonal catalytic antibodies: construction of a heavy chain variable region-specific cDNA library. *Proc Natl Acad Sci U S A* **86**, 5728-5732 (1989).

159. C. Song *et al.*, Immunotherapy for Alzheimer's disease: targeting β-amyloid and beyond. *Transl Neurodegener* **11**, 18 (2022).
160. A. Wang, P. Das, R. C. Switzer, 3rd, T. E. Golde, J. L. Jankowsky, Robust amyloid clearance in a mouse model of Alzheimer's disease provides novel insights into the mechanism of amyloid-beta immunotherapy. *J Neurosci* **31**, 4124-4136 (2011).
161. R. B. DeMattos *et al.*, Peripheral anti-A beta antibody alters CNS and plasma A beta clearance and decreases brain A beta burden in a mouse model of Alzheimer's disease. *Proc Natl Acad Sci U S A* **98**, 8850-8855 (2001).
162. K. A. Bates *et al.*, Clearance mechanisms of Alzheimer's amyloid-beta peptide: implications for therapeutic design and diagnostic tests. *Mol Psychiatry* **14**, 469-486 (2009).
163. B. Solomon, R. Koppel, E. Hanan, T. Katzav, Monoclonal antibodies inhibit in vitro fibrillar aggregation of the Alzheimer beta-amyloid peptide. *Proc Natl Acad Sci U S A* **93**, 452-455 (1996).
164. R. Deane *et al.*, IgG-assisted age-dependent clearance of Alzheimer's amyloid beta peptide by the blood-brain barrier neonatal Fc receptor. *J Neurosci* **25**, 11495-11503 (2005).
165. J. W. Arndt *et al.*, Structural and kinetic basis for the selectivity of aducanumab for aggregated forms of amyloid-β. *Sci Rep* **8**, 6412 (2018).
166. E. A. Largent, A. Peterson, H. F. Lynch, FDA Drug Approval and the Ethics of Desperation. *JAMA Internal Medicine* **181**, 1555-1556 (2021).
167. Food and Drug Administration Modernization Act of 1997 21 USC §353a (2006).
168. U. Food, D. Administration (2020) Combined FDA and Biogen briefing information for the November 6. in *2020 meeting of the peripheral and central nervous system drugs advisory committee. Published online Nov*.
169. Alzheimer Forschung Initiative e.V., Aducanumab (Aduhelm): Der aktuelle Stand. (2021).
170. FDA, FDA Converst Novel Alzheimer's Disease Treatment to Traditional Approval (2023).
171. C. J. Swanson *et al.*, A randomized, double-blind, phase 2b proof-of-concept clinical trial in early Alzheimer's disease with lecanemab, an anti-Aβ protofibril antibody. *Alzheimers Res Ther* **13**, 80 (2021).
172. Alzheimer Forschung Initiative e.V., Leqembi (Lecanemab): Neues Alzheimer-Medikament. (2023).
173. M. S. Uddin *et al.*, APOE and Alzheimer’s disease: evidence mounts that targeting APOE4 may combat Alzheimer’s pathogenesis. *Molecular neurobiology* **56**, 2450-2465 (2019).
174. A.-C. S. Vogt *et al.*, Anti-IAPP monoclonal antibody improves clinical symptoms in a mouse model of type 2 diabetes. *Vaccines* **9**, 1316 (2021).
175. A. E. Lang *et al.*, Trial of Cinpanemab in Early Parkinson's Disease. *N Engl J Med* **387**, 408-420 (2022).
176. G. Pagano *et al.*, Trial of prasinezumab in early-stage Parkinson’s disease. *New England Journal of Medicine* **387**, 421-432 (2022).
177. L. A. Lampson (2011) Monoclonal antibodies in neuro-oncology: Getting past the blood-brain barrier. in *MAbs* (Taylor & Francis), pp 153-160.
178. F. Chiti, C. M. Dobson, Protein Misfolding, Amyloid Formation, and Human Disease: A Summary of Progress Over the Last Decade. *Annu Rev Biochem* **86**, 27-68 (2017).
179. R. M. Vabulas, F. U. Hartl, Aberrant protein interactions in amyloid disease. *Cell Cycle* **10**, 1512-1513 (2011).
180. C. M. Dobson, Protein misfolding, evolution and disease. *Trends in Biochemical Sciences* **24**, 329-332 (1999).
181. E. Chuang, A. M. Hori, C. D. Hesketh, J. Shorter, Amyloid assembly and disassembly. *J Cell Sci* **131** (2018).
182. F. Chiti, C. M. Dobson, Protein misfolding, functional amyloid, and human disease. *Annu Rev Biochem* **75**, 333-366 (2006).

183. P. Westermark *et al.*, Amyloid: Toward terminology clarification Report from the Nomenclature Committee of the International Society of Amyloidosis. *Amyloid* **12**, 1-4 (2005).
184. A. B. Reiss, H. A. Arain, M. M. Stecker, N. M. Siegart, L. J. Kasselman, Amyloid toxicity in Alzheimer's disease. *Rev Neurosci* **29**, 613-627 (2018).
185. D. Aarsland *et al.*, Cognitive decline in Parkinson disease. *Nat Rev Neurol* **13**, 217-231 (2017).
186. M. G. Spillantini, R. A. Crowther, R. Jakes, M. Hasegawa, M. Goedert, α-Synuclein in filamentous inclusions of Lewy bodies from Parkinson's disease and dementia with Lewy bodies. *Proceedings of the National Academy of Sciences* **95**, 6469-6473 (1998).
187. J. Verasdonck *et al.*, Further exploration of the conformational space of α-synuclein fibrils: solid-state NMR assignment of a high-pH polymorph. *Biomolecular NMR Assignments* **10**, 5-12 (2016).
188. A. Makky, L. Bousset, J. Polesel-Maris, R. Melki, Nanomechanical properties of distinct fibrillar polymorphs of the protein α-synuclein. *Scientific reports* **6**, 1-10 (2016).
189. B. Li *et al.*, Cryo-EM of full-length α-synuclein reveals fibril polymorphs with a common structural kernel. *Nature Communications* **9**, 3609 (2018).
190. T. P. J. Knowles, M. Vendruscolo, C. M. Dobson, The amyloid state and its association with protein misfolding diseases. *Nature Reviews Molecular Cell Biology* **15**, 384-396 (2014).
191. M. Törnquist *et al.*, Secondary nucleation in amyloid formation. *Chemical Communications* **54**, 8667-8684 (2018).
192. J. D. Camino, P. Gracia, N. Cremades, The role of water in the primary nucleation of protein amyloid aggregation. *Biophysical Chemistry* **269**, 106520 (2021).
193. S. Linse, Mechanism of amyloid protein aggregation and the role of inhibitors. *Pure and Applied Chemistry* **91**, 211-229 (2019).
194. A. K. Buell, The growth of amyloid fibrils: rates and mechanisms. *Biochemical Journal* **476**, 2677-2703 (2019).
195. P. Arosio, M. Vendruscolo, C. M. Dobson, T. P. Knowles, Chemical kinetics for drug discovery to combat protein aggregation diseases. *Trends Pharmacol Sci* **35**, 127-135 (2014).
196. P. Sormanni, F. A. Aprile, M. Vendruscolo, Rational design of antibodies targeting specific epitopes within intrinsically disordered proteins. *Proc Natl Acad Sci U S A* **112**, 9902-9907 (2015).
197. S. Sangwan *et al.*, Inhibition of synucleinopathic seeding by rationally designed inhibitors. *Elife* **9** (2020).
198. Y. A. Kyriukha *et al.*, α-Synuclein Dimers as Potent Inhibitors of Fibrillization. *Journal of Medicinal Chemistry* **62**, 10342-10351 (2019).
199. K. Afitska, A. Priss, D. A. Yushchenko, V. V. Shvadchak, Structural Optimization of Inhibitors of α-Synuclein Fibril Growth: Affinity to the Fibril End as a Crucial Factor. *Journal of Molecular Biology* **432**, 967-977 (2020).
200. K. A. Murray *et al.*, De novo designed protein inhibitors of amyloid aggregation and seeding. *Proc Natl Acad Sci U S A* **119**, e2206240119 (2022).
201. H. Shaykhalishahi *et al.*, Contact between the β1 and β2 Segments of α-Synuclein that Inhibits Amyloid Formation. *Angewandte Chemie International Edition* **54**, 8837-8840 (2015).
202. E. D. Agerschou, V. Borgmann, M. M. Wördehoff, W. Hoyer, Inhibitor and substrate cooperate to inhibit amyloid fibril elongation of α-synuclein. *Chem Sci* **11**, 11331-11337 (2020).
203. E. A. Mirecka *et al.*, Sequestration of a β-hairpin for control of α-synuclein aggregation. *Angew Chem Int Ed Engl* **53**, 4227-4230 (2014).
204. Z. Liang, H. Y. E. Chan, M. M. Lee, M. K. Chan, A SUMO1-Derived Peptide Targeting SUMO-Interacting Motif Inhibits α-Synuclein Aggregation. *Cell Chem Biol* **28**, 180-190.e186 (2021).

205. J. Ahmed *et al.*, Foldamers reveal and validate therapeutic targets associated with toxic α-synuclein self-assembly. *Nat Commun* **13**, 2273 (2022).
206. B. M. Burmann *et al.*, Regulation of α-synuclein by chaperones in mammalian cells. *Nature* **577**, 127-132 (2020).
207. C. P. A. Doherty *et al.*, A short motif in the N-terminal region of α-synuclein is critical for both aggregation and function. *Nat Struct Mol Biol* **27**, 249-259 (2020).
208. S. Lesage *et al.*, G51D α-synuclein mutation causes a novel Parkinsonian–pyramidal syndrome. *Annals of Neurology* **73**, 459-471 (2013).
209. S. Appel-Cresswell *et al.*, Alpha-synuclein p.H50Q, a novel pathogenic mutation for Parkinson's disease. *Movement Disorders* **28**, 811-813 (2013).
210. P. Pasanen *et al.*, A novel α-synuclein mutation A53E associated with atypical multiple system atrophy and Parkinson's disease-type pathology. *Neurobiology of Aging* **35**, 2180.e2181-2180.e2185 (2014).
211. M. G. Spillantini *et al.*, α-Synuclein in Lewy bodies. *Nature* **388**, 839-840 (1997).
212. A. K. Buell *et al.*, Solution conditions determine the relative importance of nucleation and growth processes in α-synuclein aggregation. *Proc Natl Acad Sci U S A* **111**, 7671-7676 (2014).
213. N. S. Rösener *et al.*, Clustering of human prion protein and α-synuclein oligomers requires the prion protein N-terminus. *Commun Biol* **3**, 365 (2020).
214. M. Schweighauser *et al.*, Structures of α-synuclein filaments from multiple system atrophy. *Nature* **585**, 464-469 (2020).
215. Y. Li *et al.*, Amyloid fibril structure of α-synuclein determined by cryo-electron microscopy. *Cell Research* **28**, 897-903 (2018).
216. R. Guerrero-Ferreira *et al.*, Two new polymorphic structures of human full-length alpha-synuclein fibrils solved by cryo-electron microscopy. *eLife* **8**, e48907 (2019).
217. Y. Sun *et al.*, Cryo-EM structure of full-length α-synuclein amyloid fibril with Parkinson's disease familial A53T mutation. *Cell Research* **30**, 360-362 (2020).
218. K. Zhao *et al.*, Parkinson's disease associated mutation E46K of α-synuclein triggers the formation of a distinct fibril structure. *Nature Communications* **11**, 2643 (2020).
219. D. R. Boyer *et al.*, The α-synuclein hereditary mutation E46K unlocks a more stable, pathogenic fibril structure. *Proceedings of the National Academy of Sciences* **117**, 3592-3602 (2020).
220. K. Zhao *et al.*, Parkinson's disease-related phosphorylation at Tyr39 rearranges α-synuclein amyloid fibril structure revealed by cryo-EM. *Proceedings of the National Academy of Sciences* **117**, 20305-20315 (2020).
221. W. Hoyer *et al.*, Dependence of α-synuclein aggregate morphology on solution conditions. *Journal of molecular biology* **322**, 383-393 (2002).
222. A. E. Butler *et al.*, β-Cell Deficit and Increased β-Cell Apoptosis in Humans With Type 2 Diabetes. *Diabetes* **52**, 102-110 (2003).
223. S. E. Kahn, S. Andrikopoulos, C. B. Verchere, Islet amyloid: a long-recognized but underappreciated pathological feature of type 2 diabetes. *Diabetes* **48**, 241-253 (1999).
224. P. Westermark, Amyloid and polypeptide hormones: What is their interrelationship? *Amyloid* **1**, 47-60 (1994).
225. J. Janson *et al.*, Spontaneous diabetes mellitus in transgenic mice expressing human islet amyloid polypeptide. *Proc Natl Acad Sci U S A* **93**, 7283-7288 (1996).
226. M. M. Altamirano-Bustamante *et al.*, Unpacking the aggregation-oligomerization-fibrillization process of naturally-occurring hIAPP amyloid oligomers isolated directly from sera of children with obesity or diabetes mellitus. *Sci Rep* **9**, 18465 (2019).
227. N. F. Altamirano-Bustamante *et al.*, Protein-conformational diseases in childhood: Naturally-occurring hIAPP amyloid-oligomers and early β-cell damage in obesity and diabetes. *PLoS One* **15**, e0237667 (2020).
228. D. C. R. Camargo *et al.*, hIAPP forms toxic oligomers in plasma. *Chemical Communications* **54**, 5426-5429 (2018).

229. M. Birol, S. Kumar, E. Rhoades, A. D. Miranker, Conformational switching within dynamic oligomers underpins toxic gain-of-function by diabetes-associated amyloid. *Nature communications* **9**, 1312 (2018).
230. S. E. Kahn *et al.*, Evidence of cosecretion of islet amyloid polypeptide and insulin by beta-cells. *Diabetes* **39**, 634-638 (1990).
231. H. J. Woerle *et al.*, Impaired Hyperglycemia-Induced Delay in Gastric Emptying in Patients With Type 1 Diabetes Deficient for Islet Amyloid Polypeptide. *Diabetes Care* **31**, 2325-2331 (2008).
232. A. Kanatsuka *et al.*, Secretion of islet amyloid polypeptide in response to glucose. *FEBS Letters* **259**, 199-201 (1989).
233. U. Arnelo, *Islet amyloid polypeptide in the control of food intake: an experimental study in the rat* (Inst för klinisk vetenskap, intervention och teknik/Dept of Clinical Science …, 1997).
234. B. Åkesson, G. Panagiotidis, P. Westermark, I. Lundquist, Islet amyloid polypeptide inhibits glucagon release and exerts a dual action on insulin release from isolated islets. *Regulatory Peptides* **111**, 55-60 (2003).
235. L. Gremer *et al.*, Fibril structure of amyloid-β (1–42) by cryo–electron microscopy. *Science* **358**, 116-119 (2017).
236. R. Guerrero-Ferreira *et al.*, Cryo-EM structure of alpha-synuclein fibrils. *elife* **7**, e36402 (2018).
237. C. Roeder *et al.*, Cryo-EM structure of islet amyloid polypeptide fibrils reveals similarities with amyloid-β fibrils. *Nature Structural & Molecular Biology* **27**, 660-667 (2020).
238. E. L. Opie, ON THE RELATION OF CHRONIC INTERSTITIAL PANCREATITIS TO THE ISLANDS OF LANGERHANS AND TO DIABETES MELUTUS. *J Exp Med* **5**, 397-428 (1901).
239. A. Weichselbaum, E. Stangl, Zur Kenntnis der feineren Veränderungen des Pankreas bei Diabetes mellitus. *Wiener Klinische Wochenschrift* **14**, 968-972 (1901).
240. P. Westermark, C. Wernstedt, E. Wilander, K. Sletten, A novel peptide in the calcitonin gene related peptide family as an amyloid fibril protein in the endocrine pancreas. *Biochem Biophys Res Commun* **140**, 827-831 (1986).
241. P. Westermark *et al.*, Amyloid fibrils in human insulinoma and islets of Langerhans of the diabetic cat are derived from a neuropeptide-like protein also present in normal islet cells. *Proc Natl Acad Sci U S A* **84**, 3881-3885 (1987).
242. A. Abedini *et al.*, Time-resolved studies define the nature of toxic IAPP intermediates, providing insight for anti-amyloidosis therapeutics. *Elife* **5**, e12977 (2016).
243. L. Haataja, T. Gurlo, C. J. Huang, P. C. Butler, Islet amyloid in type 2 diabetes, and the toxic oligomer hypothesis. *Endocrine reviews* **29**, 303-316 (2008).
244. A. E. Butler, J. Janson, W. C. Soeller, P. C. Butler, Increased beta-cell apoptosis prevents adaptive increase in beta-cell mass in mouse model of type 2 diabetes: evidence for role of islet amyloid formation rather than direct action of amyloid. *Diabetes* **52**, 2304-2314 (2003).
245. T. Gurlo *et al.*, Evidence for proteotoxicity in beta cells in type 2 diabetes: toxic islet amyloid polypeptide oligomers form intracellularly in the secretory pathway. *Am J Pathol* **176**, 861-869 (2010).
246. C.-Y. Lin *et al.*, Toxic human islet amyloid polypeptide (h-IAPP) oligomers are intracellular, and vaccination to induce anti-toxic oligomer antibodies does not prevent h-IAPP–induced β-cell apoptosis in h-IAPP transgenic mice. *Diabetes* **56**, 1324-1332 (2007).
247. S. L. Masters *et al.*, Activation of the NLRP3 inflammasome by islet amyloid polypeptide provides a mechanism for enhanced IL-1β in type 2 diabetes. *Nat Immunol* **11**, 897-904 (2010).
248. J. J. Meier *et al.*, Inhibition of human IAPP fibril formation does not prevent β-cell death: evidence for distinct actions of oligomers and fibrils of human IAPP. *American Journal of Physiology-Endocrinology and Metabolism* **291**, E1317-E1324 (2006).

249. Y. Bram *et al.*, Apoptosis induced by islet amyloid polypeptide soluble oligomers is neutralized by diabetes-associated specific antibodies. *Scientific reports* **4**, 4267 (2014).
250. J. Janson, R. H. Ashley, D. Harrison, S. McIntyre, P. C. Butler, The mechanism of islet amyloid polypeptide toxicity is membrane disruption by intermediate-sized toxic amyloid particles. *Diabetes* **48**, 491-498 (1999).
251. J. Janson, R. H. Ashley, D. Harrison, S. McIntyre, P. C. Butler, The mechanism of islet amyloid polypeptide toxicity is membrane disruption by intermediate-sized toxic amyloid particles. *Diabetes* **48**, 491-498 (1999).
252. E. E. Cawood, T. K. Karamanos, A. J. Wilson, S. E. Radford, Visualizing and trapping transient oligomers in amyloid assembly pathways. *Biophys Chem* **268**, 106505 (2021).
253. C. Berardet *et al.*, Evidence for different in vitro oligomerization behaviors of synthetic hIAPP obtained from different sources. *Anal Bioanal Chem* **412**, 3103-3111 (2020).
254. D. M. Walsh, D. J. Selkoe, Aβ Oligomers – a decade of discovery. *Journal of Neurochemistry* **101**, 1172-1184 (2007).
255. E. N. Cline, M. A. Bicca, K. L. Viola, W. L. Klein, The Amyloid-β Oligomer Hypothesis: Beginning of the Third Decade. *J Alzheimers Dis* **64**, S567-s610 (2018).
256. A. J. Dear *et al.*, Identification of on- and off-pathway oligomers in amyloid fibril formation. *Chem Sci* **11**, 6236-6247 (2020).
257. M. Muschol, W. Hoyer, Amyloid oligomers as on-pathway precursors or off-pathway competitors of fibrils. *Front Mol Biosci* **10**, 1120416 (2023).
258. S. Zraika *et al.*, Toxic oligomers and islet beta cell death: guilty by association or convicted by circumstantial evidence? *Diabetologia* **53**, 1046-1056 (2010).
259. J. P. Cleary *et al.*, Natural oligomers of the amyloid-beta protein specifically disrupt cognitive function. *Nat Neurosci* **8**, 79-84 (2005).
260. R. Kayed *et al.*, Permeabilization of lipid bilayers is a common conformation-dependent activity of soluble amyloid oligomers in protein misfolding diseases. *J Biol Chem* **279**, 46363-46366 (2004).
261. M. N. Vieira *et al.*, Soluble oligomers from a non-disease related protein mimic Abeta-induced tau hyperphosphorylation and neurodegeneration. *J Neurochem* **103**, 736-748 (2007).
262. K. Ono, M. M. Condron, D. B. Teplow, Structure–neurotoxicity relationships of amyloid β-protein oligomers. *Proceedings of the National Academy of Sciences* **106**, 14745-14750 (2009).
263. F. Hasecke *et al.*, Origin of metastable oligomers and their effects on amyloid fibril self-assembly. *Chemical science* **9**, 5937-5948 (2018).
264. M. P. Schützmann *et al.*, Endo-lysosomal Aβ concentration and pH trigger formation of Aβ oligomers that potently induce Tau missorting. *Nature communications* **12**, 4634 (2021).
265. F. Hasecke *et al.*, Protofibril–fibril interactions inhibit amyloid fibril assembly by obstructing secondary nucleation. *Angewandte Chemie* **133**, 3053-3058 (2021).
266. M. Yuan, X. Tang, W. Han, Anatomy and formation mechanisms of early amyloid-β oligomers with lateral branching: graph network analysis on large-scale simulations. *Chem Sci* **13**, 2649-2660 (2022).
267. E. Andreetto *et al.*, Identification of Hot Regions of the Aβ–IAPP Interaction Interface as High-Affinity Binding Sites in both Cross-and Self-Association. *Angewandte Chemie International Edition* **49**, 3081-3085 (2010).
268. B. O'Nuallain, A. D. Williams, P. Westermark, R. Wetzel, Seeding specificity in amyloid growth induced by heterologous fibrils. *J Biol Chem* **279**, 17490-17499 (2004).
269. R. Gallardo *et al.*, Fibril structures of diabetes-related amylin variants reveal a basis for surface-templated assembly. *Nat Struct Mol Biol* **27**, 1048-1056 (2020).
270. Q. Cao, D. R. Boyer, M. R. Sawaya, P. Ge, D. S. Eisenberg, Cryo-EM structure and inhibitor design of human IAPP (amylin) fibrils. *Nat Struct Mol Biol* **27**, 653-659 (2020).

271. B. W. Koo, A. D. Miranker, Contribution of the intrinsic disulfide to the assembly mechanism of islet amyloid. *Protein Sci* **14**, 231-239 (2005).
272. K. Esposito *et al.*, Oxidative stress in the metabolic syndrome. *J Endocrinol Invest* **29**, 791-795 (2006).
273. A. Fernández-Sánchez *et al.*, Inflammation, oxidative stress, and obesity. *Int J Mol Sci* **12**, 3117-3132 (2011).
274. D. A. Butterfield, J. Drake, C. Pocernich, A. Castegna, Evidence of oxidative damage in Alzheimer's disease brain: central role for amyloid β-peptide. *Trends in Molecular Medicine* **7**, 548-554 (2001).
275. R. Inagi, Y. Ishimoto, M. Nangaku, Proteostasis in endoplasmic reticulum--new mechanisms in kidney disease. *Nat Rev Nephrol* **10**, 369-378 (2014).
276. S. S. Cao, R. J. Kaufman, Unfolded protein response. *Current Biology* **22**, R622-R626 (2012).
277. Y. Li, Y. Guo, J. Tang, J. Jiang, Z. Chen, New insights into the roles of CHOP-induced apoptosis in ER stress. *Acta Biochimica et Biophysica Sinica* **46**, 629-640 (2014).
278. H. Sidibé, A. Dubinski, C. Vande Velde, The multi-functional RNA-binding protein G3BP1 and its potential implication in neurodegenerative disease. *Journal of Neurochemistry* **157**, 944-962 (2021).
279. N. L. Kedersha, M. Gupta, W. Li, I. Miller, P. Anderson, RNA-binding proteins TIA-1 and TIAR link the phosphorylation of eIF-2α to the assembly of mammalian stress granules. *The Journal of cell biology* **147**, 1431-1442 (1999).
280. P. Yang *et al.*, G3BP1 is a tunable switch that triggers phase separation to assemble stress granules. *Cell* **181**, 325-345. e328 (2020).
281. L. Nover, K. D. Scharf, D. Neumann, Formation of cytoplasmic heat shock granules in tomato cell cultures and leaves. *Mol Cell Biol* **3**, 1648-1655 (1983).
282. D. W. Sanders *et al.*, Competing protein-RNA interaction networks control multiphase intracellular organization. *Cell* **181**, 306-324. e328 (2020).
283. A. Cléry, M. Blatter, F. H. Allain, RNA recognition motifs: boring? Not quite. *Current opinion in structural biology* **18**, 290-298 (2008).
284. J. Guillén-Boixet *et al.*, RNA-induced conformational switching and clustering of G3BP drive stress granule assembly by condensation. *Cell* **181**, 346-361. e317 (2020).
285. P. Nedumpully-Govindan *et al.*, Stabilizing Off-pathway Oligomers by Polyphenol Nanoassemblies for IAPP Aggregation Inhibition. *Scientific Reports* **6**, 19463 (2016).
286. Y. Porat, A. Abramowitz, E. Gazit, Inhibition of amyloid fibril formation by polyphenols: structural similarity and aromatic interactions as a common inhibition mechanism. *Chemical biology & drug design* **67**, 27-37 (2006).
287. F. L. Palhano, J. Lee, N. P. Grimster, J. W. Kelly, Toward the molecular mechanism (s) by which EGCG treatment remodels mature amyloid fibrils. *Journal of the American Chemical Society* **135**, 7503-7510 (2013).
288. P. Cao, D. P. Raleigh, Analysis of the inhibition and remodeling of islet amyloid polypeptide amyloid fibers by flavanols. *Biochemistry* **51**, 2670-2683 (2012).
289. F. Meng, A. Abedini, A. Plesner, C. B. Verchere, D. P. Raleigh, The flavanol (−)-epigallocatechin 3-gallate inhibits amyloid formation by islet amyloid polypeptide, disaggregates amyloid fibrils, and protects cultured cells against IAPP-induced toxicity. *Biochemistry* **49**, 8127-8133 (2010).
290. A. Pithadia, J. R. Brender, C. A. Fierke, A. Ramamoorthy, Inhibition of IAPP Aggregation and Toxicity by Natural Products and Derivatives. *J Diabetes Res* **2016**, 2046327 (2016).
291. M. S. Saravanan *et al.*, The small molecule inhibitor anle145c thermodynamically traps human islet amyloid peptide in the form of non-cytotoxic oligomers. *Scientific Reports* **9**, 19023 (2019).
292. M. Zielinski, C. Röder, G. F. Schröder, Challenges in sample preparation and structure determination of amyloids by cryo-EM. *Journal of Biological Chemistry* **297** (2021).

293. C.-j. Huang *et al.*, Induction of endoplasmic reticulum stress-induced β-cell apoptosis and accumulation of polyubiquitinated proteins by human islet amyloid polypeptide. *American Journal of Physiology-Endocrinology and Metabolism* **293**, E1656-E1662 (2007).
294. C.-j. Huang *et al.*, High expression rates of human islet amyloid polypeptide induce endoplasmic reticulum stress–mediated β-cell apoptosis, a characteristic of humans with type 2 but not type 1 diabetes. *Diabetes* **56**, 2016-2027 (2007).
295. T. Gurlo *et al.*, CHOP Contributes to, But Is Not the Only Mediator of, IAPP Induced β-Cell Apoptosis. *Mol Endocrinol* **30**, 446-454 (2016).
296. Y. Fan, K. Lee, N. Wang, J. C. He, The role of endoplasmic reticulum stress in diabetic nephropathy. *Current diabetes reports* **17**, 1-7 (2017).
297. E. A. Mirecka *et al.*, Engineered aggregation inhibitor fusion for production of highly amyloidogenic human islet amyloid polypeptide. *Journal of Biotechnology* **191**, 221-227 (2014).
298. I. Cummins, P. G. Steel, R. Edwards, Identification of a carboxylesterase expressed in protoplasts using fluorescence-activated cell sorting. *Plant biotechnology journal* **5**, 354-359 (2007).
299. G. P. Smith, Filamentous fusion phage: novel expression vectors that display cloned antigens on the virion surface. *Science* **228**, 1315-1317 (1985).
300. H. Shim, Therapeutic Antibodies by Phage Display. *Curr Pharm Des* **22**, 6538-6559 (2016).
301. R. Freudl, S. MacIntyre, M. Degen, U. Henning, Cell surface exposure of the outer membrane protein OmpA of Escherichia coli K-12. *J Mol Biol* **188**, 491-494 (1986).
302. P. S. Daugherty, Protein engineering with bacterial display. *Curr Opin Struct Biol* **17**, 474-480 (2007).
303. M. P. Schreuder, S. Brekelmans, H. van den Ende, F. M. Klis, Targeting of a heterologous protein to the cell wall of Saccharomyces cerevisiae. *Yeast* **9**, 399-409 (1993).
304. K. S. Lam *et al.*, A new type of synthetic peptide library for identifying ligand-binding activity. *Nature* **354**, 82-84 (1991).
305. A. K. Price, A. B. MacConnell, B. M. Paegel, Microfluidic Bead Suspension Hopper. *Analytical Chemistry* **86**, 5039-5044 (2014).
306. D. Dressman, H. Yan, G. Traverso, K. W. Kinzler, B. Vogelstein, Transforming single DNA molecules into fluorescent magnetic particles for detection and enumeration of genetic variations. *Proc Natl Acad Sci U S A* **100**, 8817-8822 (2003).
307. T. Thorsen, R. W. Roberts, F. H. Arnold, S. R. Quake, Dynamic Pattern Formation in a Vesicle-Generating Microfluidic Device. *Physical Review Letters* **86**, 4163-4166 (2001).
308. M. Gantz, S. Neun, E. J. Medcalf, L. D. van Vliet, F. Hollfelder, Ultrahigh-Throughput Enzyme Engineering and Discovery in In Vitro Compartments. *Chemical Reviews* 10.1021/acs.chemrev.2c00910 (2023).
309. P.-Y. Colin, A. Zinchenko, F. Hollfelder, Enzyme engineering in biomimetic compartments. *Current Opinion in Structural Biology* **33**, 42-51 (2015).
310. R. Fudala *et al.*, Fluorescence detection of MMP-9. I. MMP-9 selectively cleaves Lys-Gly-Pro-Arg-Ser-Leu-Ser-Gly-Lys peptide. *Curr Pharm Biotechnol* **12**, 834-838 (2011).
311. World Health Organization (2023) Diabetes, https://www.who.int/news-room/fact-sheets/detail/diabetes, last accessed on 23.07.23
312. S. E. Inzucchi *et al.*, Management of hyperglycemia in type 2 diabetes, 2015: a patient-centered approach: update to a position statement of the American Diabetes Association and the European Association for the Study of Diabetes. *Diabetes Care* **38**, 140-149 (2015).
313. S. Kalra *et al.*, Place of sulfonylureas in the management of type 2 diabetes mellitus in South Asia: A consensus statement. *Indian J Endocrinol Metab* **19**, 577-596 (2015).

314. I. Thrainsdottir, K. Malmberg, A. Olsson, M. Gutniak, L. Rydén, Initial experience with GLP-1 treatment on metabolic control and myocardial function in patients with type 2 diabetes mellitus and heart failure. *Diab Vasc Dis Res* **1**, 40-43 (2004).
315. S. Paul *et al.*, Catalytic hydrolysis of vasoactive intestinal peptide by human autoantibody. *Science* **244**, 1158-1162 (1989).
316. H. Taguchi *et al.*, Catalytic antibodies to amyloid beta peptide in defense against Alzheimer disease. *Autoimmun Rev* **7**, 391-397 (2008).
317. S. Paul, S. Planque, Y. Nishiyama, Beneficial catalytic immunity to abeta peptide. *Rejuvenation Res* **13**, 179-187 (2010).
318. R. Glockshuber, M. Malia, I. Pfitzinger, A. Plueckthun, A comparison of strategies to stabilize immunoglobulin Fv-fragments. *Biochemistry* **29**, 1362-1367 (1990).
319. C. Hamers-Casterman *et al.*, Naturally occurring antibodies devoid of light chains. *Nature* **363**, 446-448 (1993).
320. A. S. Greenberg *et al.*, A new antigen receptor gene family that undergoes rearrangement and extensive somatic diversification in sharks. *nature* **374**, 168-173 (1995).
321. D. Könning *et al.*, Camelid and shark single domain antibodies: structural features and therapeutic potential. *Current opinion in structural biology* **45**, 10-16 (2017).
322. R. M. Anthony, J. V. Ravetch, A novel role for the IgG Fc glycan: the anti-inflammatory activity of sialylated IgG Fcs. *Journal of clinical immunology* **30**, 9-14 (2010).
323. G. Alter, T. H. Ottenhoff, S. A. Joosten (2018) Antibody glycosylation in inflammation, disease and vaccination. in *Seminars in immunology* (Elsevier), pp 102-110.
324. P. Cysewski, M. Przybyłek, R. Rozalski, Experimental and theoretical screening for green solvents improving sulfamethizole solubility. *Materials* **14**, 5915 (2021).
325. J.-S. Park *et al.*, Solubility enhancement of aggregation-prone heterologous proteins by fusion expression using stress-responsive Escherichia coli protein, RpoS. *BMC biotechnology* **8**, 1-11 (2008).
326. MRC Centre for Protein Engineering V Base https://www2.mrc-lmb.cam.ac.uk/vbase/alignments2.php, last accessed on 20.07.2023
327. D. R. Boyer *et al.*, Structures of fibrils formed by α-synuclein hereditary disease mutant H50Q reveal new polymorphs. *Nat Struct Mol Biol* **26**, 1044-1052 (2019).
328. H. Taguchi *et al.*, Autoantibody-catalyzed hydrolysis of amyloid beta peptide. *J Biol Chem* **283**, 4714-4722 (2008).
329. H. Taguchi *et al.*, Exceptional amyloid beta peptide hydrolyzing activity of nonphysiological immunoglobulin variable domain scaffolds. *J Biol Chem* **283**, 36724-36733 (2008).